Precipitation Variability over the Northeastern United States: Large-Scale Drivers and Large-Scale Meteorological Patterns

By

Raymond Sukhdeo

B.S. (Stony Brook University) 2016
M.S. (Stony Brook University) 2018

DISSERTATION

Submitted in partial satisfaction of the requirements for the degree of

DOCTOR OF PHILOSOPHY

in

Atmospheric Science

in the

OFFICE OF GRADUATE STUDIES

of the

UNIVERSITY OF CALIFORNIA

DAVIS

Approved:

_____

Dr. Paul A. Ullrich, Co-Chair

_____

Dr. Richard Grotjahn, Co-Chair

_____

Dr. Mark D. Risser

Committee in Charge
2024

Doctoral Committee:

Dr. Paul A. Ullrich, Co-Chair
Dr. Richard Grotjahn, Co-Chair
Dr. Mark D. Risser, Dissertation Signee
Dr. Matthew R. Igel
Dr. Terrence R. Nathan

For Mom, Rohan, and Nirmala

"Wherever you find strength, or beauty, or spiritual power, you may be sure that these have sprung from just a spark of my essence."
-Lord Krishna, *Bhagavad Gita*, Chapter 10: Verse 41

Acknowledgements

I would like to first and foremost thank my graduate advisors Paul Ullrich and Richard Grotjahn for all of their advice, guidance, mentorship, and support throughout my PhD tenure at UC Davis. Back in 2019 when I was going through the PhD program recruitment process, I initially had some qualms about moving roughly 3,000 miles away from New York City to Davis, California, but I knew that the opportunity to work with Paul and Richard was too good to pass up. In retrospect, it was one of the greatest decisions of my life. Paul and Richard have helped me to expand my research network, provided me with support (and patience) as I've developed my technical skills in atmospheric science, and encouraged my independence as a researcher. I am the scientist I am today because of Paul and Richard, and I sincerely look forward to my continued collaborative efforts with them in the future.

I would also like to thank my mother Sandra, brother Rohan, and sister Nirmala for their lifetime of love and support. I feel extremely blessed to have you all as part of my support system.

Special thanks as well to the rest of my PhD committee: Mark Risser, Matt Igel, and Terry Nathan. I could always rely on you all for helpful insight into my work.

Thank you to my graduate group peers, in particular Lucas, Leif, Argel, Will, Clark, and Abhishekh, for your support, assistance, and discussions as I've worked to complete my PhD.

Lastly, I would like to thank my funding sources that have helped to facilitate my PhD work, specifically the Integrated Coastal Modeling (ICoM) project, the United States Department of Energy (DOE), the Milton family for their contributions to the 2023 Milton Award, and the UC Davis Professors for the Future (PFTF) fellowship program.

Table of Contents

Raymond Sukhdeo

July 2024

Atmospheric Science

Precipitation Variability over the Northeastern United States: Large-Scale Drivers and Large-Scale Meteorological Patterns

Abstract

The northeastern United States (hereinafter, the Northeast) is home to a dense human population and encompasses a variety of agricultural and economic interests that are reliant on the available water resources and the replenishment of those resources via precipitation. Due to ongoing climate change, water availability is expected to be altered in this region. This expected change is particularly important at the ends of the precipitation spectrum (i.e., extreme precipitation and droughts), as these events can lead to devastating economic damages to infrastructure, property, and agriculture. Given the many problems that can be associated with an increased frequency of both wet and dry extremes, it has become increasingly important to gain a better understanding of the large-scale meteorology related to precipitation variability in the Northeast. Such insight provides meaningful insight for stakeholders and policymakers with interests pertaining to future resource allocations and water management practices in the region.

This PhD work seeks to build upon the existing literature related to understanding the large-scale processes that are important in producing conditions favorable to precipitation in the Northeast, and uses that understanding to examine the meteorological conditions that accompany short-duration dry spells (droughts) that occur over the region. My dissertation establishes a unique

framework by which to explore scientific questions related to Northeast precipitation variability by utilizing a novel linear orthogonal decomposition technique, large-scale meteorological pattern analysis, analysis of relevant dynamical and thermodynamical fields, and reanalysis and climate model datasets. Such a framework provides a comprehensive assessment of the meteorological conditions associated with different precipitation regimes over the Northeast. This research topic sits at the intersection of atmospheric science, regional climate, machine learning, and climate model validation, with the overall goal of improving our capabilities in regional climate analysis.

Chapter 1 provides an introduction and background information related to precipitation in the Northeast. Chapter 2 focuses on identifying the large-scale drivers of precipitation over the Northeast using a novel linear orthogonal decomposition (LOD) approach. Chapter 3 examines the absence (or reduction) of those drivers during short-duration dry spells (droughts) over the region primarily using large-scale meteorological pattern (LSMP) analysis. Chapter 4 assesses the fidelity of current-generation general circulation models (GCMs) in representing different characteristics of the dry spells in comparison to those obtained from observations. Lastly, Chapter 5 summarizes the work discussed in this dissertation and provides insight into potential avenues for future work.

Chapter 1 – Introduction

1.1 – Northeastern U.S. Precipitation, Droughts, and Dissertation Overview

The 21st century will continue to see dramatic changes to the Earth climate system due in large part to anthropogenic influences. At present, the Intergovernmental Panel on Climate Change (IPCC) has confidently attributed climate system processes at global scales. However, understanding of these processes at global scales does not necessarily translate to regional scales, where most stakeholder and policymaker decisions are made, particularly with regards to water resource management (Field et al. 2014). As a result, this presents a unique and pressing challenge for our understanding of regional climate and how it may evolve under climate change.

The northeastern United States (hereinafter, the Northeast) is one such region that will be influenced by ongoing climate change, particularly with regards to its precipitation. With a dense human population and a variety of agricultural and economic interests, this region is heavily reliant on the available water resources and the replenishment of those resources via precipitation. The Northeast exhibits seasonal cycles for several important precipitation characteristics, such as number of precipitating days, precipitation intensity, and precipitation total. These characteristics are discussed in detail in Agel et al. (2015) and are summarized in part here. Precipitation intensity tends to have large annual variation, with peaks in late summer, spring and fall. These differences in seasonal precipitation characteristics are due in part to the large-scale features and storm tracks associated with daily precipitation in the region. Extratropical storms account for 80-85% of the total precipitation from December to May (Pfahl and Wernli 2012; Agel et al. 2015). Storm track also plays a key role in this seasonal cycle, and there are two broad regions with the greatest storm track density: one over the Great Lakes region and another along the Atlantic seaboard (Kocin and

Uccellini 2004; Pfahl and Wernli 2012; Agel et al. 2015). Track density is highest in the winter and spring. In the summertime, while extratropical cyclone activity is reduced, localized convection, mesoscale convective activity (Feng et al. 2019), and tropical cyclones (Barlow 2011) can be important drivers of precipitation in the region.

With the continued progression of climate change, water availability and precipitation are expected to be altered in the Northeast (Melillo et al. 2014). These changes are particularly important at the ends of the precipitation spectrum (i.e., extreme precipitation and droughts), as these events risk billions of dollars' worth of damage to infrastructure, property, and agriculture (Lott and Ross 2006). Observations have shown an upward trend in the frequency and intensity of extreme precipitation in the Northeast in the last several decades (Kunkel et al. 1999; DeGaetano 2009; Pryor et al. 2009; Howarth et al. 2019). This region has also experienced several major droughts in the twentieth century (Seager et al. 2012), and model projections suggest more short-term droughts in the region due to increased warming and evaporative demand (Hayhoe et al. 2007; Xue and Ullrich 2021). The most famous of these droughts, which persisted from 1962-1967 period (Namias 1966), had major implications for agricultural and water management practices, and still serves as the standard for future water resource planning. Given the many problems that can be associated with an increased frequency in both extreme precipitation and drought conditions, one of the main goals of this dissertation is to gain a better understanding of the large-scale meteorology associated with precipitation variability over the Northeast.

In the context of Northeast precipitation variability and dry extremes that impact the region, this dissertation fills important gaps in the present literature by identifying the large-scale drivers of precipitation variability, and uses insight from that analysis to explore the meteorological conditions associated with short-duration droughts (dry spells) in the region. The specific foci of

this dissertation are to: 1) explore the large-scale atmospheric drivers of precipitation in the Northeast, 2) analyze historical short-duration dry spells that have impacted the region, and 3) assess the ability of CMIP6 models to represent different characteristics of the historical dry spells. Raymond Sukhdeo was the primary author on all works and conducted the bulk of the work in relation to testing hypotheses, literature review, data acquisition, data analysis, and the drafting of each manuscript. Both Paul Ullrich and Richard Grotjahn were the primary advisors and mentors on all works. They both provided consistent commentary, technical guidance, and mentorship where needed via email, in-person meetings, and Zoom meetings. Additionally, Paul Ullrich provided access to computing resources and assistance with the tracking of extratropical cyclone activity across multiple data products.

Chapter 2 represents a successful attempt to identify the large-scale drivers of precipitation over the Northeast using a novel linear orthogonal decomposition (LOD) approach. The goal of the LOD approach is to sub-sample and extract the time series of several predictor fields in order to maximize the linear predictability of precipitation. This technique provides a convenient and comprehensive means by which to determine the meteorological processes that lead to precipitation over the Northeast, and these LOD modes are robust in multiple datasets. The study is now published in the Climate Dynamics journal under the DOI:10.1007/s00382-022-06289-y.

Chapter 3 explores the meteorological conditions associated with short-duration droughts (dry spells) over the Northeast. This analysis is conducted primarily using large-scale meteorological pattern (LSMP) analysis. After determining the LSMPs associated with the dry spells, other meteorological fields, such as upper-level zonal winds, low-level moisture, and extratropical cyclone activity are explored. This work fills an important gap in the drought

literature by focusing on events lasting between 12-29 days. The study is now published in the Monthly Weather Review journal under the DOI:10.1175/MWR-D-23-0141.1.

Chapter 4 considers the fidelity of 15 CMIP6 models in representing different characteristics of the dry spells in comparison to the ERA5 reanalysis dataset, including LSMP spatial correlation and the percentage of dry days associated with events lasting 12 days or longer. Error metrics for these different characteristics are used to devise a model weighting scheme that ranks the models from best to worst and allows for an assessment of the composite CMIP6 representation of the dry spells. This work serves as an important validation tool to assess GCM representation of regional climate conditions. The study is currently in preparation for submission to an academic journal.

Chapter 5 summarizes and concludes the work discussed in this dissertation, and also explores possible avenues for future work, specifically with regard to 1) understanding how climatological mean biases may impact model representation of LSMPs, 2) examining future projections of dry spell characteristics in the Northeast, and 3) identifying possible teleconnection mechanisms that may influence the manifestation of the dry spell LSMPs.

1.2 – References

Agel L, M. Barlow, J-H, Qian, F. Colby, E. Douglas, and T. Eichler, 2015: Climatology of daily precipitation and extreme precipitation events in the northeast United States. *J. Hydrometeorol*, **16**, 2537–2557, doi:10.1175/JHM-D-14-0147.1.

Barlow, M., 2011: Influence of hurricane-related activity on North American extreme precipitation. *Geophys. Res. Lett.*, **38**, L04705. doi:10.1029/2010GL046258.

DeGaetano, A.T., 2009: Time-dependent changes in extreme- precipitation return-period amounts in the continental United States. *J. Appl. Meteor. Climatol.*, **48**, 2086–2099, doi:10.1175/2009JAMC2179.1.

Feng, Z., et al., 2019: Spatiotemporal characteristics and large-scale environments of mesoscale convective systems east of the Rocky Mountains. *Journal of Climate*, **32(21)**, 7303–7328. doi:10.1175/JCLI-D-19-0137.1.

Field, C.B., et al., 2014: Climate Change 2014: Impacts, Adaptation, and Vulnerability. Part A: Global and Sectoral Aspects. Contribution of Working Group II to the Fifth Assessment Report of the Intergovernmental Panel on Climate Change ed C.B. Field et al. (*Cambridge: Cambridge University Press*) Technical summary.

Hayhoe, K., and Coauthors, 2007: Past and future changes in climate and hydrological indicators in the US Northeast. *Clim Dyn.*, **28**, 381–407, doi:10.1007/s00382-006-0187-8.

Howarth, M.E., C.D. Thorncroft, and L.H. Bosart LH, 2019: Changes in extreme precipitation in the Northeast United States: 1979–2014. *J. Hydrometeorol.*, **20**, 673–689. doi:10.1175/JHM-D-18-0155.1.

Kocin, P.J. and L.W. Uccellini, 2004: Northeast Snowstorms. *Meteor. Monogr.*, **No. 54**, Amer. Meteor. Soc., 818 pp. doi:10.1007/978-1-878220-32-5.

Kunkel, K.E., K. Andsager, and D.R. Easterling 1999: Long-term trends in extreme precipitation events over the conterminous United States and Canada. *J. Climate*, **12**, 2515–2527, doi:10.1175/1520-0442(1999)012,2515:LTTIEP.2.0.CO;2.

Lott, N., and T. Ross, 2006: Tracking and evaluating U. S. billion-dollar weather disasters, 1980–2005. AMS Forum: Environmental Risk and Impacts on Society: Successes and Challenges, Atlanta, GA, Amer. Meteor. Soc., 1.2. [Available online at https://ams.confex.com/ams/Annual2006/techprogram/ paper_100686.htm.]

Melillo, J. M., T. C. Richmond, and G. W. Yohe, 2014: *Climate Change Impacts in the United States: The Third National Climate Assessment.* U.S. Global Change Research Program, 841 pp., doi:10.7930/J0Z31WJ2.

Namias, J., 1966: Nature and possible causes of the northeastern United States drought during 1962–65. *Mon. Wea. Rev.*, **94**, 543–554, doi:10.1175/1520-0493(1966)094<0543:napcot>2.3.co;2.

Pfahl, S. and H. Wernli, 2012: Quantifying the relevance of cyclones for precipitation extremes. *J. Climate*, **25**, 6770–6780, doi:10.1175/JCLI-D-11-00705.1.

Pryor, S.C., J.A. Howe, and K.E. Kunkel, 2009: How spatially coherent and statistically robust are temporal changes in extreme precipitation in the contiguous USA? *Int. J. Climatol.*, **29**, 31–45, doi:10.1002/joc.1696.

Seager, R., N. Pederson, Y. Kushnir, J. Nakamura, and S. Jurburg, 2012b: The 1960s drought and the subsequent shift to a wetter climate in the Catskill Mountains Region of the New York City watershed. *J. Clim.,* **25**, 6721–6742. doi:10.1175/JCLI-D-11-00518.1.

Xue, Z., and P.A. Ullrich, P.A., 2021: A retrospective and prospective examination of the 1960s U.S. northeast drought. *Earth's Future*, **9**, e2020EF001930, doi:10.1029/2020EF001930.

Chapter 2 – Assessing the Large-Scale Drivers of Precipitation in the Northeastern United States via Linear Orthogonal Decomposition

Abstract

This study examines the linear orthogonal modes associated with monthly precipitation in the northeastern United States, from CESM1 LENS (35 ensemble members, 1979-2005) and two reanalysis datasets (ERA5, 1950-2018 and NOAA-CIRES-DOE 20CRv3, 1950-2015). Calendar months are aggregated together, and any linear trends in data are removed. Using region-averaged precipitation anomaly time series and monthly anomalies for several global 2D atmospheric fields, a linear orthogonal decomposition method is implemented to iteratively extract time series (based on field and geographic location) of absolute maximum correlation. Linear modes associated with this method are then projected onto the full set of 2D fields to provide physical insight into the mechanisms involved in generating precipitation. In this region, the first mode is associated with vapor transport from the Atlantic seaboard, the second mode is characterized by westward vapor transport associated with extratropical cyclones, and the third mode captures vapor transport from the Gulf of Mexico during the fall and winter. However, the third mode is less robust in the spring and summer. Results are generally consistent across the datasets, and applying multiple linear regression with the linear modes to predict the precipitation anomalies produces R-squared values of around 0.54 – 0.65 for CESM1 LENS, and around 0.58 – 0.88 for reanalysis, with the lowest values generally in the spring and late summer. The influence of low-frequency climate variability on the modes is considered for CESM1 LENS, and the modes in late winter can be predicted with some success via a combination of several, prominent large-scale teleconnection patterns.

2.1 – Introduction

The northeastern United States (hereafter the Northeast) is home to a dense human population and encompasses a variety of agricultural and economic interests that are reliant on the available water resources and the replenishment of those resources via precipitation. However, water availability in this region is expected to be altered under climate change (Melillo et al. 2014). These trends are particularly important at the ends of the precipitation spectrum (i.e., extreme precipitation and droughts), as these events risk billions of dollars' worth of damage to infrastructure, property, and agriculture (Lott and Ross 2006). Observations have shown an upward trend in the frequency and intensity of extreme precipitation in the Northeast in the last several decades (Kunkel et al. 1999; DeGaetano 2009; Pryor et al. 2009; Kunkel et al. 2013a; Kunkel et al. 2013b; Howarth et al. 2019). This region has also experienced several major droughts in the 20th century (Seager et al. 2012b), and model projections suggest more short-term droughts in the region due to warming and increased evaporative demand (Hayhoe et al. 2007). The most famous of these droughts, which persisted over the 1962-1967 period (Namias 1966), had major implications for agricultural and water management practices, and still serves as the standard for future water resource planning. Given the many problems that can be associated with an increased frequency in both extreme precipitation and drought conditions, it has become increasingly important to gain a better understanding of the dominant, large-scale atmospheric drivers of precipitation in the Northeast, particularly those that accompany both wet and dry extremes. Such an understanding provides meaningful insight for stakeholders with interests pertaining to future resource allocations and water management practices in the region.

The Northeast exhibits seasonal cycles for several precipitation characteristics, such as number of precipitating days, precipitation intensity, and precipitation total. These characteristics

are discussed in detail in Agel at al. (2015) (hereafter A015), and are summarized in part here. Precipitation intensity tends to have a large annual variation, with a peak in late summer and dual peaks in the spring and fall. These differences in seasonal precipitation characteristics are due in part to the large-scale features and storm tracks associated with daily precipitation in the region. Extratropical storms account for 80-85% of the total precipitation from December to May (Pfahl and Wernli 2012; A015), and the dual peak in precipitation intensity in the spring and fall is related to a weakening of storm-related intensity in May (Pfahl and Wernli 2012; A015). Storm track also plays a key role in this seasonal cycle, and in each season, there are two broad regions with the greatest storm track density: one over the Great Lakes region and another over the Atlantic seaboard (Kocin and Uccellini 2004; Pfahl and Wernli 2012; A015). Track density is highest in the winter and spring, and during the summer and fall, track density in these areas is weaker and shifted northward into the lower portion of eastern Canada. In the summertime, while extratropical cyclone activity is reduced, localized convection, mesoscale convective activity (Feng et al. 2019), and tropical cyclones (Barlow 2011) can be important drivers of precipitation in the region.

Winter precipitation variability in the Northeast has been shown to be more significantly related to the large-scale circulation than in other seasons (Ning et al. 2012a). Previous studies (e.g., Hartley and Keables 1998; Kunkel and Angel 1999; Bradbury et al. 2003) have demonstrated that prominent, large-scale teleconnection patterns, such as the North Atlantic Oscillation (NAO) (Wallace and Gutzler 1981; Barnston and Livezey 1987), the Pacific-North American pattern (PNA) (Wallace and Gutzler 1981; Leathers et al. 1997), and the El Niño-Southern Oscillation (ENSO) (Trenberth 1997), can have important influences on winter precipitation in the Northeast.

However, the relationships identified between winter precipitation and the large-scale teleconnection patterns are generally not robust (Ropelewski and Halpert 1986; Hurrell 1995;

Bradbury et al. 2002a; Bradbury et al. 2002b; Archambault et al. 2008). This lack of statistical significance is hypothesized to be because regional precipitation has inherent, complex variability, and the large-scale modes of climate variability previously discussed also have differing influences across the Northeast. As such, it becomes difficult to identify their influence when examining the domain holistically. Indeed, as determined by Ning and Bradley (2014), linear correlation and composite analysis show that different teleconnection patterns have significant influences on different precipitation patterns, which may explain why previous studies (e.g., Bradbury et al. 2002a; Archambault et al. 2008) did not find robust relationships between total winter precipitation over the whole domain and individual teleconnection patterns.

Our work here seeks to build upon the existing literature related to understanding the large-scale processes that are important in producing conditions favorable to precipitation in the Northeast and assessing the role that large-scale teleconnection patterns may have in those processes. Since this study is primarily concerned with water availability, we focus on monthly accumulated precipitation. Recent studies, such as Agel et al. (2015; 2017; 2019), have addressed the climatology of extreme precipitation in the context of overall precipitation in the region (A015), the large-scale meteorological patterns (LSMPs) associated with that precipitation (Agel et al. 2017; hereafter A017), and the dynamical structures and key ingredients for extreme precipitation, such as moisture and instability, that are linked to those LSMPs (Agel et al. 2019). Their analysis of the climatology of overall precipitation in the Northeast provides an excellent reference point for understanding the seasonal trends in the regional precipitation, and their assessment of the LSMPs and their associated dynamical pathways informs us about which processes are crucial in generating precipitation. However, these analyses have focused on daily,

extreme precipitation and have primarily examined the LSMPs associated with that precipitation via the use of clustering methods.

Studies such as these are nonetheless informative to understanding monthly-averaged precipitation, because it is reasonable to assume that most months in which there are more precipitating days will have greater monthly-averaged precipitation amounts (See Supplemental Materials in the online version of this journal article). This also indicates that smaller-scale features, such as localized convection, fronts and extratropical cyclones, which can facilitate heavier precipitation, directly impact monthly precipitation totals.

In this study, we seek to improve the current understanding of environmental conditions favorable to Northeast precipitation and quantify the relative contributions to precipitation amount from upstream drivers. This is achieved by: I) examining a large number of meteorological fields to understand which are likely associated with precipitation in the region, II) using a novel linear orthogonal decomposition-based technique, instead of clustering analysis, in order to identify a set of independent large-scale modes that are nearly optimal for prediction of precipitation totals, III) using multiple linear regression (MLR) to determine the amount of precipitation variability explained by the linear combination of those atmospheric modes, and IV) determining the influence of several large-scale teleconnection patterns on precipitation predictability via an analogous MLR framework.

The preceding paragraphs frame our study in the context of previous studies that have examined Northeast precipitation and its associated large-scale drivers, and outline some of contributions our study can make to the existing literature. Specifically, in this present work, we seek to address the following questions:

1) What are the dominant, large-scale atmospheric drivers of precipitation in the northeastern United States, as identified by a linear orthogonal decomposition?
2) How well can multiple linear regression models predict monthly-averaged precipitation in the Northeast?
3) How well does CESM1 LENS compare to reanalysis products with regards to the linear orthogonal modes identified in this study?
4) What is the dependence of the linear orthogonal modes on low-frequency modes of climate variability?

To address these questions, monthly-averaged precipitation in the Northeast is examined in connection with several "basic" atmospheric fields. The linear orthogonal decomposition is used to sub-sample the time series of all predictor fields at all grid points in order to maximize the linear predictability, in the sense of multiple linear regression (MLR). Such an approach is complementary to other methods for decomposing the meteorological fields that drive precipitation, such as k-means clustering analysis; however, one advantage of the linear decomposition is that the linear modes are easily combined within a single linear model, while total precipitation amounts are more difficult to extract from clustered fields. The approach pursued in this study can provide improved insight into the monthly trends and variability associated with Northeast precipitation, as well as inform the level of linear predictability for precipitation in the region via an understanding of key atmospheric features.

The remainder of the paper is organized as follows. Datasets are described in Section 2.2. Methodology is discussed in Section 2.3. Results and analysis of selected linear orthogonal modes are provided in Section 2.4. The paper concludes with a summary and discussion in Section 2.5.

2.2 – Data

Our study makes use of both reanalysis and large ensemble model simulations. For reanalysis, monthly data is drawn from the ERA5 dataset (Hersbach et al. 2020) at 0.25° x 0.25° latitude/longitude grid spacing, and from the NOAA-CIRES-DOE 20CRv3 dataset (Slivinski et al. 2019), with latitude/longitude grid spacing of 1.0° x 1.0°. ERA5 covers the period from 1950-2018 (69 years), while NOAA-CIRES-DOE 20CRv3 covers 1950-2015 (66 years). Both datasets include monthly-averaged data on single levels, as well as monthly-averaged data on several pressure levels (i.e., 500-hPa and 850-hPa). We also employ the CESM1 LENS dataset (Kay et al. 2015), which uses a 0.94240838° x 1.25° latitude/longitude grid. For CESM1 LENS, we draw on data from a subset of the historical period, from 1979-2005, and from the first 35 ensemble members of the dataset (giving 35 ensemble members x 27 years = 945 samples for each month), which provides the advantage of producing many more samples for analysis in each month. We seek to understand the large-scale drivers of Northeast precipitation for each calendar month (i.e., January, February, …, November, December) separately. In the case of CESM1 LENS, this aggregation is also performed over all ensemble members. As such, the monthly data for each calendar month are aggregated together and analyzed separately from the other calendar months. For example, after aggregation, we would have 69, 66, and 945 concatenated Januarys for ERA5, NOAA-CIRES-DOE 20CRv3, and CESM1 LENS, respectively, for use in our analysis. This aggregation is similarly done for the other calendar months. Of important note is the difference in the variety of atmospheric fields between the reanalysis products and the CESM1 LENS dataset. ERA5 and NOAA-CIRES-DOE 20CRv3 offer many more fields for analysis as compared to CESM1 LENS, in part due to the relatively large space requirements when CESM1 LENS was generated. As a result, for the purposes of congruency between our assessment of the reanalysis

products and model simulations, we have chosen to examine only atmospheric fields that are common to all three datasets. These fields are referred to now as “basic” atmospheric fields and include: geopotential height at 500-hPa (“Z500”), specific humidity at 850-hPa (“Q850”), zonal wind at 850-hPa (“U850”), meridional wind at 850-hPa (“V850”), sea-level pressure (“PSL”), two-meter temperature (“T2M”), eastward integrated vapor transport (“IVTe”), northward integrated vapor transport (“IVTn”), sea-surface temperature (“SST”) and 700-hPa omega (“ω700"). Total precipitation (“PRECT”) is also drawn from the three datasets, and a regional, area-averaged PRECT time series is calculated, using a geographic domain of 40-45°N and 70-75°W for the Northeast, for use in our methodology (See Section 2.3). Sensitivity testing for this domain was conducted to verify the robustness of our methodology and results. The results of this testing are given in Section 4 of the Online Resource. IVTe and IVTn are not readily given from NOAA-CIRES-DOE 20CRv3 and CESM1 LENS, and so are approximated from the Q850, U850, and V850 fields.

2.3 – Methodology

2.3a – Linear Orthogonal Decomposition (LOD)

Here we provide an overview and summary of the LOD method. The mathematical details of the method can be found in Appendix A.

As stated in Section 2.1, the goal of the LOD method is to sub-sample the time series of all predictor fields at all grid points in order to maximize linear predictability in the context of MLR. To begin, for a particular calendar month of aggregated data (ex. January), a reference state (in our analysis this is the climatological monthly mean) is first subtracted away from the precipitation time series and the 2D atmospheric fields, to generate anomalies of those data. If an obvious and

undesired trend is present in the time series, it can be removed by using a time-dependent linear field instead. The iterative procedure begins with the following: 1) the precipitation anomaly time series is correlated with each 2D anomaly atmospheric field, at each grid point, 2) the 2D anomaly atmospheric field and grid point of absolute maximum correlation is then identified, and used to create a linear model of the original precipitation anomaly time series, 3) this linear model precipitation (in this case, LOD Mode 1) is then subtracted away from the original precipitation anomaly time series. This will give us the remainder of the original precipitation anomaly time series that has yet to be predicted. Steps 1-3 are then repeated iteratively, with the original precipitation anomaly time series replaced with the unpredicted remainder. In Steps 2 and 3, we impose orthogonality constraints so that the time series of each identified linear mode is linearly independent from all others. In reality, the processes associated with each linear mode are not independent from each other. However, in our study, applying this artificial orthogonality criteria allows us to better isolate the individual contribution of particular large-scale drivers to the regional precipitation.

To our knowledge, such an approach has not been employed for assessing the linear predictability of precipitation in a region from relevant atmospheric fields. Instead, most studies employ principal component analysis (PCA) as a means of determining key modes. The linear orthogonal decomposition approach is somewhat analogous, with each extracted linear mode being orthogonal to the others. However, it brings an added nuance in that modes are tied directly to the variable being predicted, and allows us to iteratively extract the features across all 2D fields that are most strongly correlated with the monthly, region-averaged precipitation. The iterative method may be terminated at any point – here, we terminate our CESM1 LENS analysis at iteration N when the maximum absolute correlation at iteration N+1 is < 0.10. For reanalysis products, global

correlations tend to be higher, and so the process is terminated with a higher absolute correlation threshold of 0.20. Note that, while the iterative strategy described above does not guarantee the modes selected are the optimal set of modes to maximize predictability, they are certainly a close approximation to this optimum. Indeed, we expect finding such an optimal combination of field vectors would require an exhaustive search of all possible sets, which would make the problem computationally intractable.

Through the employ of multiple climate data products, we can ascertain whether or not a particular mode is likely to have physical meaning. Namely, we posit that if a particular linear orthogonal mode from our analysis appears consistent across such a set of high-quality products, we can say that the patterns exposed by the linear orthogonal decomposition are robust. On the other hand, if a particular mode is inconsistent across products, it is likely to be a manifestation of structural uncertainty or weather variability (i.e., the component of the precipitation that is inherently unpredictable).

2.3b – Multiple Linear Regression (MLR) Using Linear Modes to Predict PRECT

For the analysis of each particular calendar month of aggregated data, a multiple linear regression (MLR) model is generated, using the time series of the linear modes as predictors and the original precipitation anomaly time series as predictand. Indeed, it can be shown that the root mean square error of this MLR model is related to the "unexplained precipitation" at each step of the process via the expression $RMSE^n = \sqrt{\frac{1}{N-n-1}(\widehat{\mathbf{p}}^n \cdot \widehat{\mathbf{p}}^n)}$, where $\widehat{\mathbf{p}}^n$ is the unpredicted precipitation at iteration step n. The MLR model enables us to validate our above scheme by providing additional confirmation of the explained variance afforded by the "basic" atmospheric fields that was calculated in Part A. Additionally, MLR also provides the 95% confidence range

for the coefficients associated with each linear mode time series. These coefficients, in conjunction with the linear mode time series, allow us to determine how well our extracted modes combine linearly in the predictability of the monthly, region-averaged precipitation, and allow us to test whether or not these time series are in fact statistically significant predictors.

2.3c – Multiple Linear Regression (MLR) Using Climate Indices to Predict Linear Modes

In a similar process to that discussed in Section 2.3b, for the analysis of a particular month, an MLR model is built with several climate indices being used as predictors, and each linear mode time series being the predictand. The climate indices under consideration are: AMO, DMI, IPO, NAO, Nino1+2, Nino3, Nino3.4, Nino4, PDO, and PNA. All climate indices are initially included in the linear model regression for each linear mode time series. After the initial regression output, a recursive elimination approach is used to select only the climate indices that are significant at the 99% confidence level (p-value < 0.01). This feature selection based on recursive elimination is done for each linear mode time series for each calendar month of aggregated data.

2.4 – Results

2.4a – CESM1 LENS: Discussion of LOD Modes

As discussed previously, the linear orthogonal decomposition method allows us to determine the large-scale modes and processes that are most closely associated with monthly-averaged precipitation in the Northeast. These processes that are important in the generation of precipitation will often be embedded within large-scale meteorological patterns (LSMPs; Grotjahn et al. 2016), and these LSMPs in turn describe the atmospheric circulation that can be attributed to specific phenomena, in this case, precipitation in the Northeast. However, often the LSMPs

themselves may not be the primary drivers and/or direct influencers of the generation of precipitation. Rather, these LSMPs provide a favorable environment for other processes to generate precipitation (A017). Our linear orthogonal modes are analogous to these LSMPs, and while our LSMP-like linear orthogonal modes lack a local consistency metric, contour shading in our plots indicates statistically significant (p-value < 0.05) regions in our modes based on Student's t-testing. As such, the modes generated by the linear orthogonal decomposition are able to capture several important large-scale drivers of precipitation in the region. Given the similarity in results between the reanalysis products and CESM1 LENS, the larger sample size afforded by CESM1 LENS that allows us to avoid overestimation of the predictability of the LOD modes, and because this work is focused on understanding these large-scale drivers of precipitation as a means for informing future resource allocations and water management practices in the region, we choose to highlight the CESM1 LENS results here in Section 2.4. Results for the reanalysis products are similar to these, and are shown in the Online Resource of the Climate Dynamics article.

i. Winter and Early Spring

Our analysis of January for CESM1 LENS data (Figs. 2.1, 2.2, and 2.3) is used here to capture the large-scale conditions that are conducive to wintertime precipitation in the Northeast. Results for December, February, and March are similar, and can be found in the Online Resource. The results of our linear orthogonal decomposition method for CESM1 LENS are given in Table 2.1, and are discussed in part here and in the other subsections of Section 2.4a.

After applying the methodology discussed in Section 2.3, it emerges that the first linear mode is associated with northward integrated vapor transport (IVTn) (Fig. 2.1f), which is maximal along the Atlantic seaboard near coastal Virginia, the second linear mode is associated with

weakened westward integrated vapor transport (IVTe) over the Northeast (Fig. 2.2e), and the third linear mode is associated with northward integrated vapor transport (IVTn) originating from the Gulf of Mexico region (Fig. 2.3f). Recall that in each iteration step, the selected time series of data (based on field and geographic location) is determined by absolute maximum correlation with the region-averaged precipitation anomaly time series. Projecting these selected time series (our linear modes) onto the 2D meteorological fields (i.e., calculating their correlations with each point in the field, as in Step 1 of Section 2.3a) provides further insight into the physical mechanisms that can lead to precipitation. Looking at Fig. 2.1a, the east-west dipole of Z500 over the central United States and the North Atlantic provides a favorable mechanism for integrated vapor transport from the west and south. Increased moisture transport into the region, coupled with enhanced vertical motion (as seen in the ω700 field, Fig. 2.1h), creates a conducive environment for precipitation to occur. This finding is reasonable, as ocean-enhanced transport from the south or southeast can provide a rich source of water vapor into the Northeast. A017 demonstrate that IVTn is stronger for extreme precipitation as compared to interquartile (25-75th percentile) precipitation. This suggests that precipitation totals in January (and winter and early spring as a whole) are strongly connected to the amount of southerly moisture transport into the region. Correlation plots based on the second linear mode for PSL, IVTe, and ω700 (Fig. 2.2) suggest that low surface pressure to the south of the Northeast drives a weakening of the westerly flow and leads to moisture convergence. This is attributed, at least in part, to enhanced extratropical cyclone activity near this region. Enhanced surface lows, originating from the midwestern or southeastern United States, can move northward into the region, and the associated cyclonic rotation of these systems can stimulate a weakening of the westerly flow that facilitates increased westward vapor transport and moisture convergence, while frontal activity can provide an additional lifting mechanism for precipitation

to occur. Examining the Z500 and IVTn correlation plots for the third linear mode (Fig. 2.3) suggests that the location of high- and low-pressure systems can facilitate integrated vapor transport from the Gulf of Mexico into the central and east-central United States. In a similar (albeit weaker) manner to the first linear mode, increased southwesterly moisture convergence into the region can help to generate precipitation.

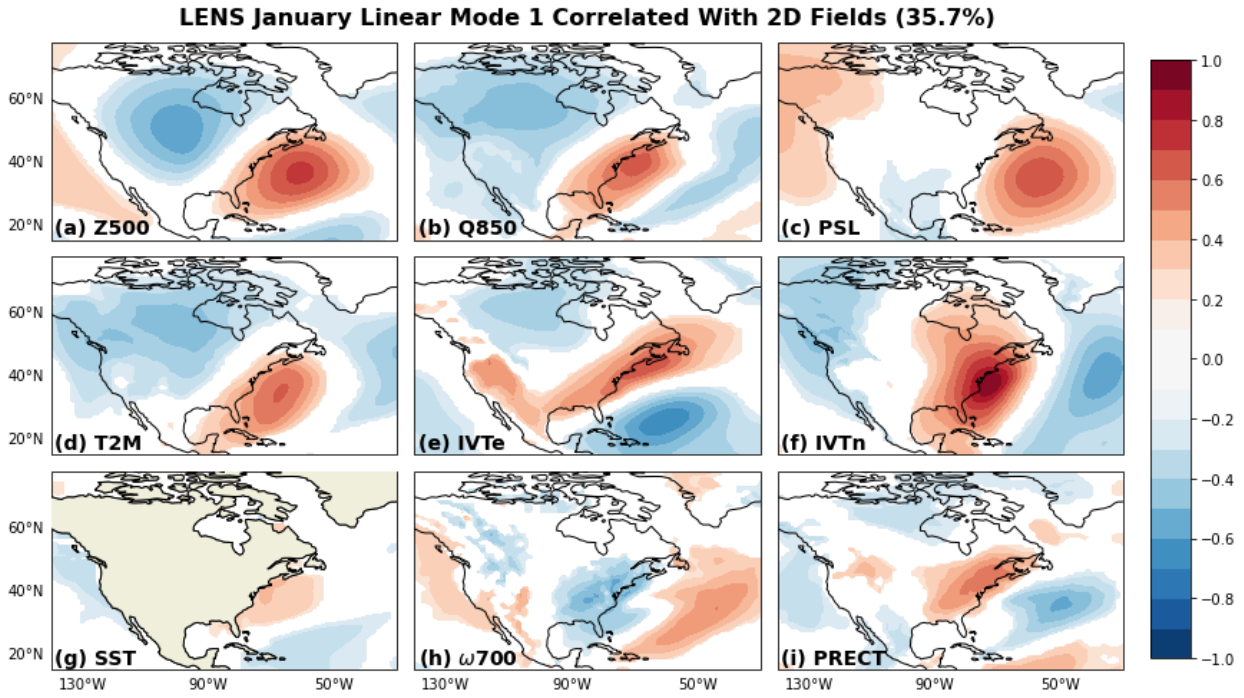

Fig. 2.1 CESM1 LENS January Linear Mode 1 for overall precipitation correlated with anomaly fields for a) 500-hPa geopotential height, b) 850-hPa specific humidity, c) sea-level pressure, d) two-meter temperature, e) eastward integrated vapor transport, f) northward integrated vapor transport, g) sea-surface temperature, h) 700-hPa omega, and i) total precipitation. Contour shading indicates significance at the 95% confidence level. Percentage is fraction of precipitation variance explained by the first linear mode in January

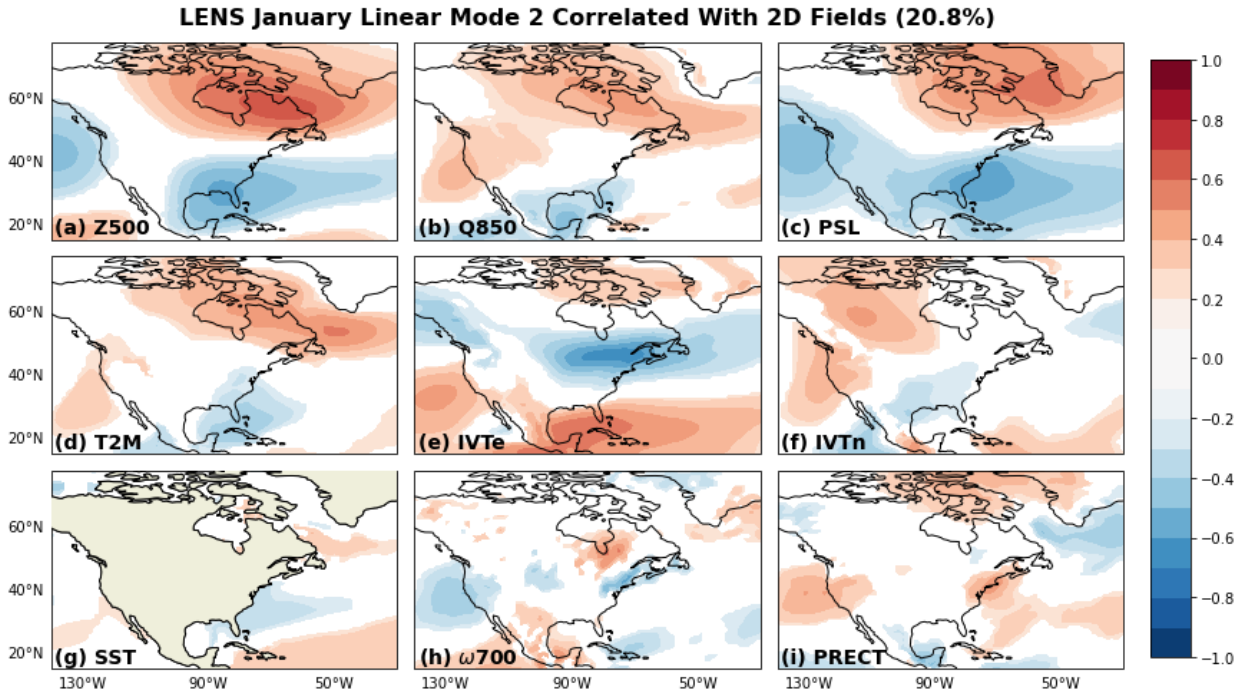

Fig. 2.2 Same as **Fig. 2.1**, but for Linear Mode 2

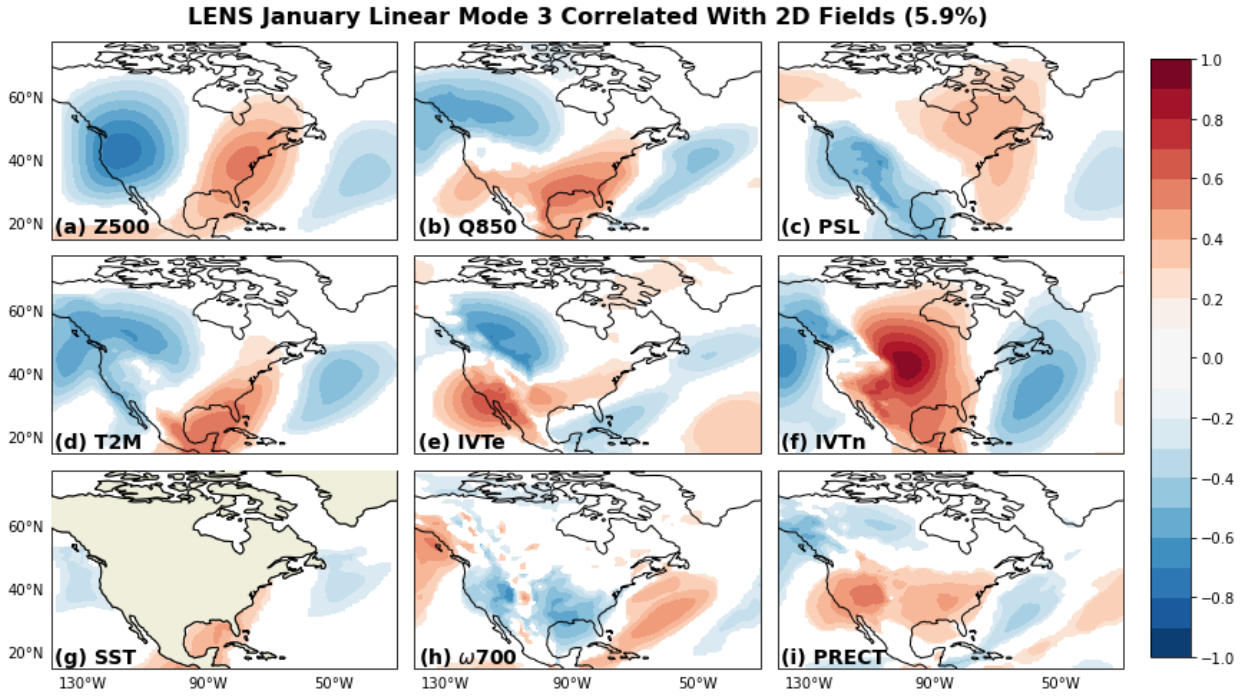

Fig. 2.3 Same as **Fig. 2.1**, but for Linear Mode 3

Table 2.1: LOD Results for CESM1 LENS

	$d\hat{p}^1$	$d\hat{p}^2$	$d\hat{p}^3$	$d\hat{p}^4$	R-Squared Value
January	IVTn(72°W,37°N) 0.5979 [0.56,0.64] 35.7%	U850(71°W,45°N) 0.4556 [0.42,0.49] 20.8%	IVTn(98°W,42°N) 0.2436 [0.21,0.28] 5.9%	Z500(92°W,18°N) 0.1208 [0.08,0.16] 1.5%	0.639
February	IVTn(71°W,37°N) 0.6317 [0.59,0.67] 39.9%	U850(70°W,46°N) 0.3884 [0.35,0.43] 15.1%	Z500(110°W,49°N) 0.2784 [0.24,0.32] 7.8%	PSL(90°W,47°N) 0.1506 [0.11,0.19] 2.3%	0.650
March	IVTn(70°W,38°N) 0.6085 [0.57,0.65] 37.0%	U850(71°W,46°N) 0.4216 [0.38,0.46] 17.8%	Z500(110°W,48°N) 0.2664 [0.23,0.31] 7.1%	IVTe(75°W,37°N) 0.1164 [0.08,0.16] 1.4%	0.632
April	IVTn(70°W,39°N) 0.5752 [0.54,0.62] 33.1%	U850(71°W,46°N) 0.4504 [0.41,0.49] 20.3%	Z500(105°W,50°N) 0.2136 [0.17,0.25] 4.6%	IVTe(76°W,38°N) 0.1486 [0.11,0.19] 2.2%	0.601
May	IVTn(70°W,40°N) 0.5310 [0.49,0.57] 28.2%	U850(71°W,46°N) 0.5108 [0.47,0.55] 26.1%	IVTe(77°W,38°N) 0.2398 [0.20,0.28] 5.7%	T2M(52°W,41°N) 0.1821 [0.14,0.22] 3.3%	0.634
June	IVTn(68°W,40°N) 0.6450 [0.61,0.68] 41.6%	IVTe(70°W,46°N) 0.4190 [0.38,0.46] 17.8%	IVTe(75°W,39°N) 0.2225 [0.19,0.26] 4.9%	IVTn(89°E,20°N) 0.1038 [0.07,0.14] 1.1%	0.652
July	IVTn(70°W,40°N) 0.6964 [0.66,0.74] 49.5%	IVTe(71°W,46°N) 0.3632 [0.33,0.40] 13.2%	Z500(92°W,36°N) 0.1390 [0.10,0.18] 1.9%		0.636
August	IVTn(68°W,40°N) 0.5355 [0.49,0.58] 28.7%	IVTe(72°W,46°N) 0.4661 [0.42,0.51] 21.7%	IVTe(76°W,39°N) 0.2466 [0.20,0.29] 6.1%		0.565
September	IVTn(68°W,39°N 0.4827 [0.44,0.53] 28.8%	U850(71°W,46°N) 0.4411 [0.40,0.48] 19.1%	IVTe(80°W,39°N) 0.2888 [0.25,0.33] 4.8%	T2M(56°W,42°N) 0.1779 [0.14,0.22] 2.4%	0.543
October	IVTn(70°W,39°N) 0.5918 [0.55,0.63] 35.0%	U850(70°W,47°N) 0.4646 [0.43,0.50] 21.6%	Z500(80°W,27°N) 0.1920 [0.15,0.23] 3.7%	Z500(57°W,24°N) 0.1168 [0.08,0.16] 1.4%	0.617
November	IVTn(71°W,36°N) 0.5719 [0.53,0.61] 32.7%	U850(70°W,46°N) 0.4549 [0.41,0.50] 20.7%	V850(62°W,26°N) 0.1958 [0.16,0.24] 3.8%	Q850(73°W,40°N) 0.1531 [0.11,0.19] 2.3%	0.596
December	IVTn(72°W,37°N 0.5550 [0.52,0.60] 30.8%	U850(70°W,45°N) 0.4783 [0.44,0.52] 22.8%	Z500(111°W,42°N) 0.2516 [0.21,0.29] 6.3%	Q850(106°W,12°N) 0.1074 [0.07,0.15] 1.2%	0.612

Table 2.1 Linear orthogonal decomposition results for CESM1 LENS data. First four columns represent the first four linear orthogonal modes. Rows for the first four columns indicate, respectively, i) selected atmospheric field and geographic grid point, ii) linear regression coefficient value, iii) 95% confidence range for the coefficient value, iv) fraction of explained variance of the precipitation data. Last column indicates R-squared value produced from multiple linear regression using the linear orthogonal modes to predict precipitation

ii. Late Spring

Results for April (as shown in the Online Resource) demonstrates good similarity with the results for the winter period and March, with our respective modes of Atlantic seaboard vapor transport (first linear mode), westward vapor transport associated with extratropical cyclone activity (second linear mode), and vapor transport from the Gulf of Mexico (third linear mode). However, as we move later into the season, there is an eastward shift of the east-west dipole of Z500 over the central United States and the North Atlantic. This configuration continues to provide a favorable mechanism for integrated vapor transport from the west and south, but indicates a transition period in the large-scale pattern over the conterminous United States. In terms of generating precipitation, this transition leads to the configuration for May (Figs. 2.4, 2.5, and 2.6), in which there is more noticeable shallow troughing in the Ohio River Valley. This pattern accompanies vapor transport from the south and southwest (Fig. 2.4), but reduced vapor transport from the Gulf of Mexico (Fig. 2.6). As was the case in preceding months, the location of the trough acts to modulate processes such as vapor transport, low pressure development, and whether available moisture from the Gulf of Mexico can reach the Northeast. In the case of May, it appears that Gulf of Mexico vapor transport is not a relatively important process because it is does not make its way as far northward as in the winter months.

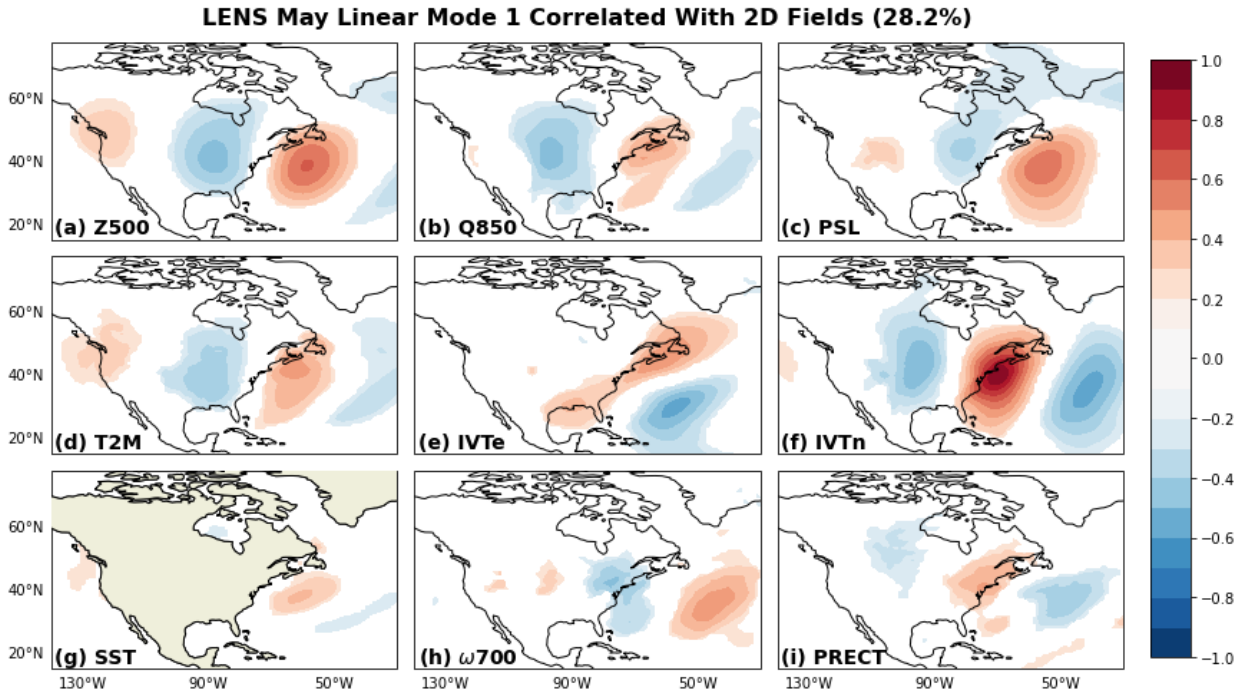

Fig. 2.4 CESM1 LENS May Linear Mode 1 for overall precipitation correlated with anomaly fields for a) 500-hPa geopotential height, b) 850-hPa specific humidity, c) sea-level pressure, d) two-meter temperature, e) eastward integrated vapor transport, f) northward integrated vapor transport, g) sea-surface temperature, h) 700-hPa omega, and i) total precipitation. Contour shading indicates significance at the 95% confidence level. Percentage is fraction of precipitation variance explained by the first linear mode in May

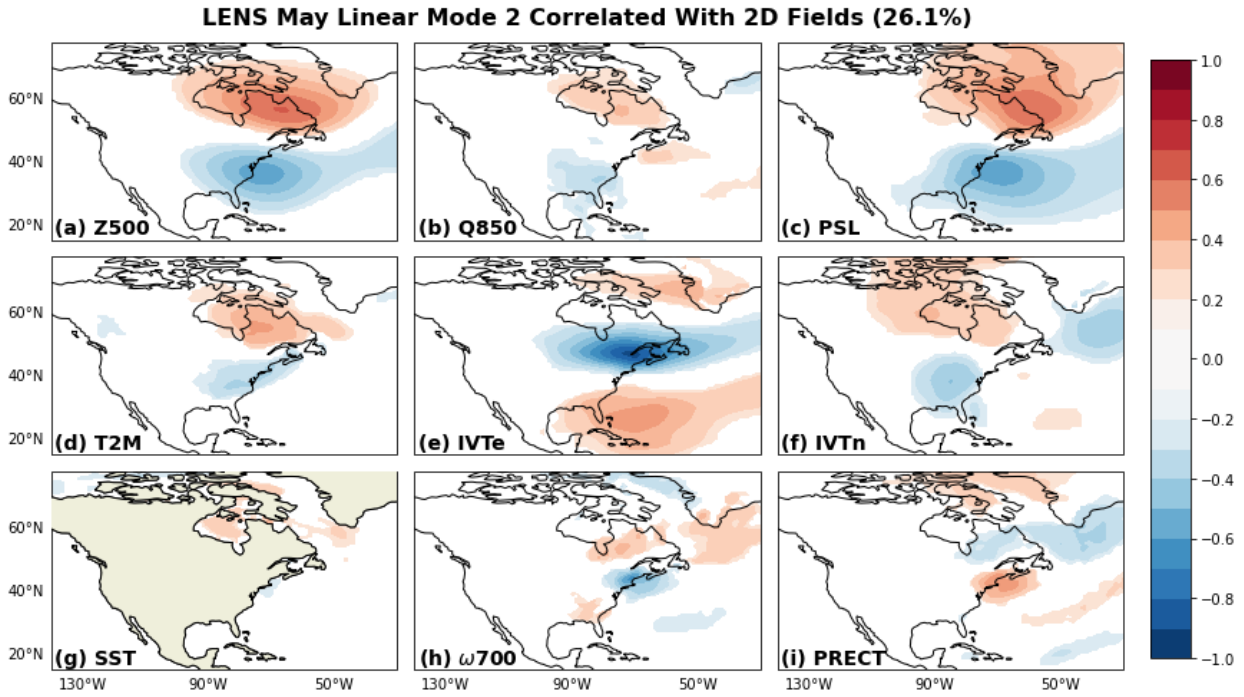

Fig. 2.5 Same as **Fig. 2.4**, but for Linear Mode 2

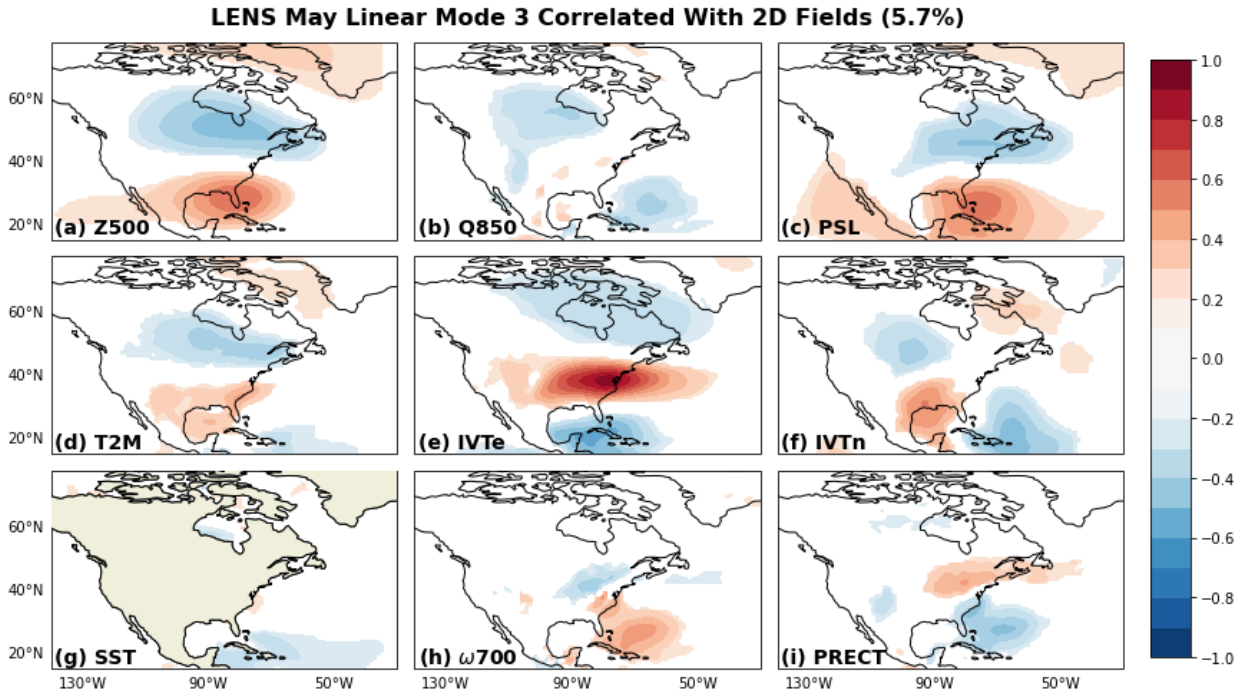

Fig. 2.6 Same as **Fig. 2.4**, but for Linear Mode 3

iii. Summer and Early Fall

Our results for July (Figs. 2.7 and 2.8) exhibit several notable differences from those discussed already for the winter and late spring months (similar results for June, August, and September; shown in Online Resource). While vapor transport from the Atlantic seaboard (first linear mode) is still a prominent process for the generation of precipitation, both the influence of extratropical cyclone activity (see subsection *v* in Section 2.4a) and vapor transport from the Gulf of Mexico are diminished during this seasonal period, and seem to be replaced in part by other processes. Regarding the second linear mode, inspection of the Z500 correlation field (Fig. 2.8a) indicates a pressure ridge in southeastern Canada. The anticyclonic flow associated with a ridge pattern in the north could facilitate moisture advection into the region. The warmer summer environment also leads to a substantial increase in moisture capacity, and warm, moist unstable air

suggests an association with convective activity (Fig. 2.8h), such as localized thunderstorms. Additionally, while localized convection can be important for generating precipitation, shortwave vorticity maxima propagating through longwave ridges can create a mechanism for convection to occur within these ridge patterns themselves (Milrad et al. 2014). Given that we are working with monthly aggregated data, it would be difficult to fully resolve the influence of localized convective activity, and the mechanisms proposed in the previous few sentences are only hypotheses about what large-scale drivers may be associated with the second linear mode. It may just be the case that extratropical cyclone activity is still the relevant driver of precipitation in the mode, but is reduced in importance, relative to the winter and spring periods. The third linear mode for July (as shown in the Online Resource) is difficult to physically interpret and provides only a small fraction of explained precipitation variance (1.9%), and as such is not discussed in great detail here. We hypothesize that this third linear mode may correspond to enhancement of the environment conducive to mesoscale convective system (MCS) activity. It must be noted, however, that MCSs are more of a prominent feature in the central U.S., and occur with much less frequency in the Northeast, even though these systems account for roughly 10-20% of total precipitation in the region during the summer period (Feng et al. 2019). So, while MCSs can be heavy-precipitation events when they do occur, they are infrequent and would not be resolved in our monthly aggregated data, and we would refer readers to Feng et al. (2019) for further discussion of these systems. If this third mode is in fact related to MCSs, this may explain why our third linear mode in July explains only 1.9% of the precipitation variance.

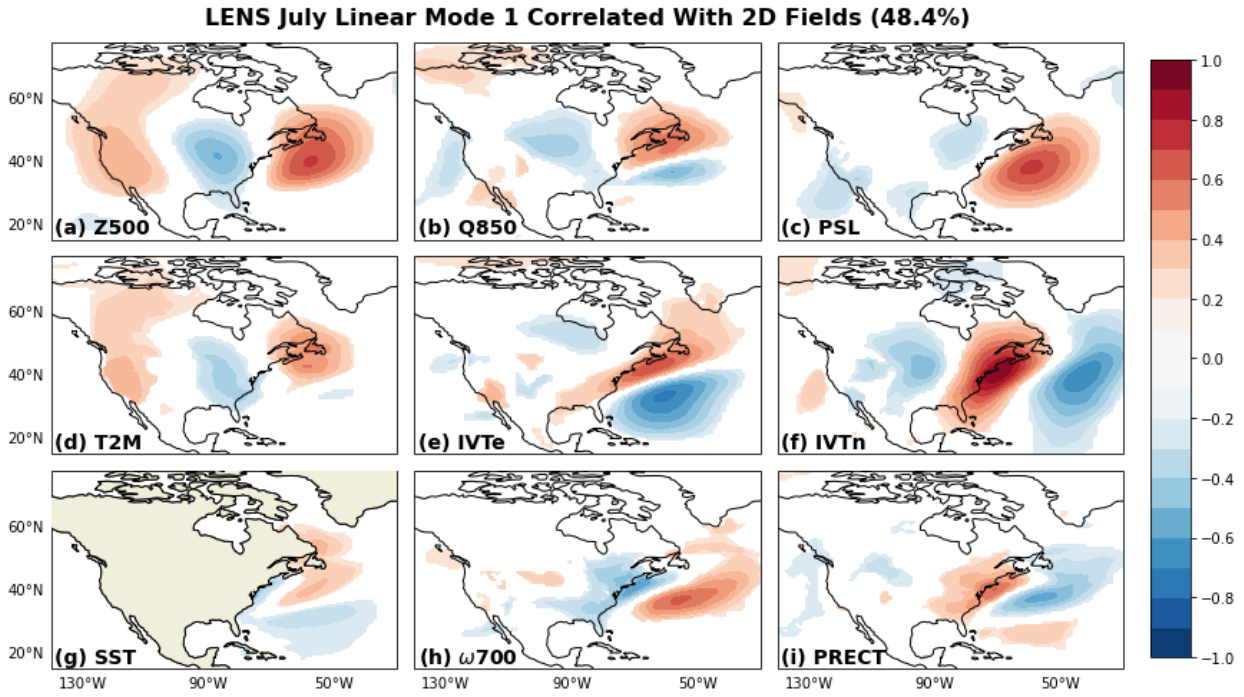

Fig. 2.7 CESM1 LENS July Linear Mode 1 for overall precipitation correlated with anomaly fields for a) 500-hPa geopotential height, b) 850-hPa specific humidity, c) sea-level pressure, d) two-meter temperature, e) eastward integrated vapor transport, f) northward integrated vapor transport, g) sea-surface temperature, h) 700-hPa omega, and i) total precipitation. Contour shading indicates significance at the 95% confidence level. Percentage is fraction of precipitation variance explained by the first linear mode in July

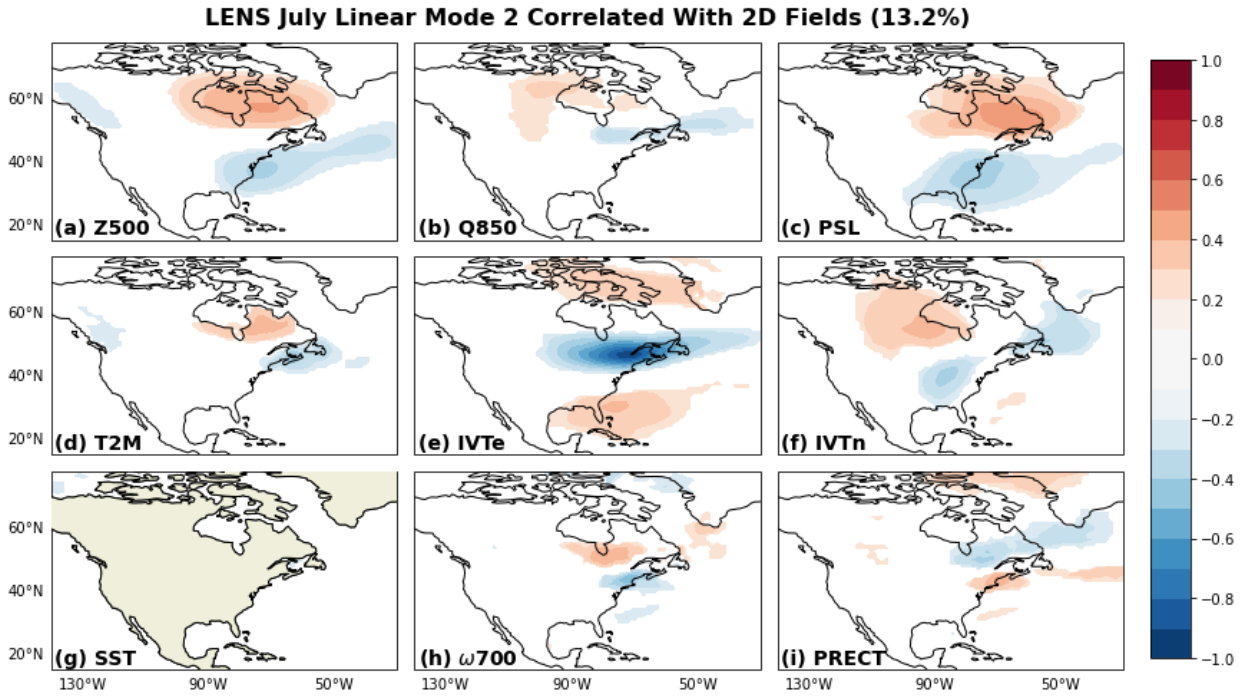

Fig. 2.8 Same as **Fig. 2.7**, but for Linear Mode 2

iv. Fall to Late Fall

Our analysis for October and November (as shown in the Online Resource) demonstrates a return to a large-scale configuration with drivers that are similar to those found during the winter and early spring, namely Atlantic seaboard vapor transport (first linear mode), westward vapor transport associated with extratropical cyclone activity (second linear mode), and vapor transport from the Gulf of Mexico (third linear mode). More specifically, the east-west Z500 dipole found during October and November is similar to the configuration found during April, in which the dipole is now phase-shifted westward. This is likely due to the late fall being a transition period before the winter, in which this Z500 dipole is shifted further westward and stays in place during much of the winter and into the early spring.

v. Extratropical Cyclone (ETC) Activity

We have proposed that the second linear mode during the fall, winter, and spring is most closely associated with extratropical cyclone (ETC) activity to the south of our region of interest. This assertion, however, has not yet been demonstrated. It can be difficult to directly link synoptic-scale (~1-3 day) systems, such as ETCs, with monthly precipitation totals, as averaging can potentially dilute the contribution of individual strong systems. However, in our study here, we are more interested in how our LOD modes modulate the large-scale environment in which these ETCs are present and not necessarily with their actual precipitation amounts. To examine this relationship, we track the total number of time steps in 6-hourly daily data when ETC activity is present for a specific geographic domain relevant to the Northeast. In this way, we are able to link the synoptic-scale influence of ETCs to their relevance in influencing monthly precipitation totals. For tracking ETCs, we use the TempestExtremes software package (Ullrich and Zarzycki 2017),

which allows for the tracking of pointwise features within climate datasets. Six-hourly data for surface pressure (PS) and geopotential at 300 hPa and 500 hPa (Z300 and Z500, respectively) are taken from CESM1 LENS for the period 1990-2005 in each of the first 35 ensemble members and used to drive TempestExtremes, which then outputs the relevant ETC tracking information, such as time, the latitude/longitude of the cyclone centers and local sea-level pressure. Output from TempestExtremes is then filtered for geographic relevance to the Northeast, with a latitude/longitude domain of 25-55°N and 60-100°W, respectively (Fig. 2.9, left). This choice of domain accounts for both the high-density North Atlantic storm track as well as the extratropical storms traveling across the Great Lakes region (Hoskins and Hodges 2002). After the filtering process, the total number of time steps with ETC activity are tabulated to generate separate "ETC Activity" time series for each calendar month of aggregated data (January – December). These time series are generated with the same aggregation method as discussed in Sections 2.2 and 2.3. The time series can then be correlated with the appropriate subsection of our linear mode time series (Table 2.4).

Fig. 2.9 (right) shows the monthly distribution of ETC activity. There are far more instances of ETC activity during the late fall and winter periods, and a decline during the late spring and summer. These results agree well with those of Hawcroft et al. (2012) and A015, which find that extratropical storms account for nearly 80-85% of total precipitation in late fall / winter periods, and indicates that extratropical cyclones are not a prominent feature for Northeast precipitation during the late spring and summer periods. We can further validate the role of ETC activity in certain calendar months by examining the correlation values between our linear modes and the ETC Activity time series. From Table 2.4, we see that ETC activity is not well correlated with either the first or third linear modes. For the second linear mode, the correlation values are much

higher and scale well with the total number of time steps with ETC activity in each month. This provides reasonable confidence that the second linear mode is related to ETCs traveling northward into the Northeast. As discussed previously, extratropical storms are an important driver of precipitation in the Northeast, and can be a primary driver of extreme precipitation conditions, as a large percentage of extreme precipitation along the Atlantic seaboard occurs near extratropical cyclone centers (Kunkel et al. 2012; Pfahl and Wernli 2012). Additionally, Pfahl and Sprenger (2016) showed that cyclone intensity and moisture availability scale well to precipitation amount, meaning that stronger cyclones and greater moisture content likely lead to increased precipitation totals. Looking back at our plots for the second linear mode, particularly during the late fall / winter periods, we see that this relationship is validated. It may seem surprising that the ETC Activity time series are generally not well correlated with the first linear mode, given the overall importance of ETCs in contributing to monthly precipitation totals. However, it is worth keeping in mind that LOD modes represent orthogonal contributions to monthly-averaged precipitation and as such can either reinforce or counteract one another. Effectively what we are seeing is that precipitation is a nonlinear combination of both moisture availability and dynamic uplift. Our first LOD mode appears to be primarily related to moisture availability in the Northeast, which is modulated primarily by southerly vapor transport. Our second LOD mode appears to be more strongly related to dynamic uplift, which is primarily influenced by frontal activity. Strong positive values in both modes would be indicative of both a moistening of the Northeast and strong dynamic uplift, likely contributing to extremely wet conditions in such a month. With that said, opposite dynamic patterns are apparent in the PSL field, and seem to limit the co-occurrence of these conditions: the first mode suggests that optimal moisture transport occurs when PSL is enhanced off the Atlantic

seaboard, while the second mode suggests that ETCs primarily occur in conjunction with negative PSL anomaly in this region.

Additionally, when testing alternative ETC tracking domains (see Section 6 of the Online Resource), we see that the strength of the correlation between the first linear mode and the ETC Activity time series is sensitive to the choice of domain (i.e., tracking ETCs in a particular domain can lead to more or less Atlantic seaboard vapor transport). While this sensitivity does exist regarding the first linear mode, the correlations with the second linear mode are insensitive to domain choice, such that the strongest correlations are between the ETC Activity time series and the second linear mode, regardless of domain choice. This further confirms our finding that the second linear mode is most strongly related to ETCs.

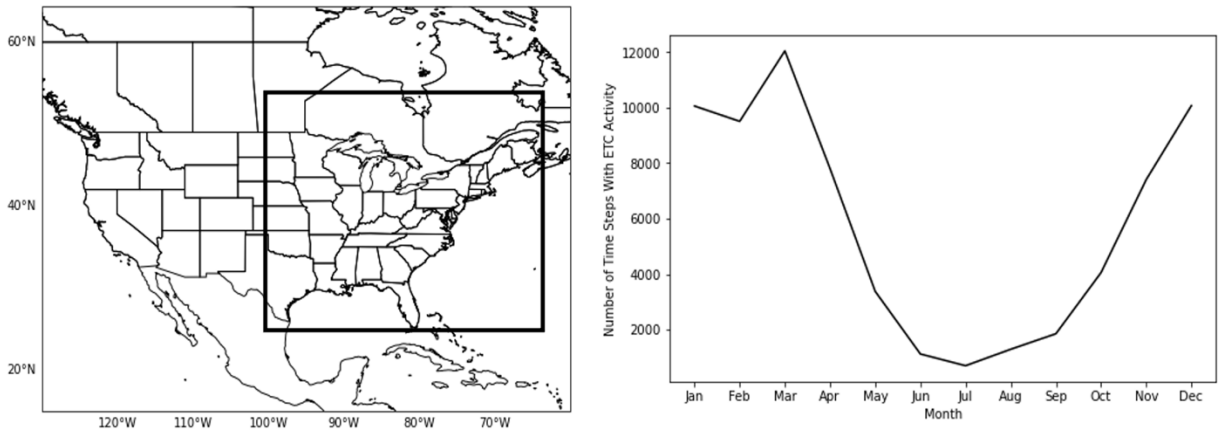

Fig. 2.9 Geographic domain for ETC tracking (left) and total monthly instances of ETC activity (right) for CESM1 LENS. ETC tracking domain accounts for storms that move northward along the Atlantic seaboard and those from the Great Lakes region

Table 2.4: Correlation Values Between Linear Modes and ETC Activity Time Series

	Jan	Feb	Mar	Apr	May	Jun	Jul	Aug	Sep	Oct	Nov	Dec
Linear Mode 1	**0.163**	0.027	0.072	0.059	0.022	0.060	0.046	0.097	0.048	0.025	0.049	**0.244**
Linear Mode 2	**0.411**	**0.485**	**0.435**	**0.304**	**0.232**	**0.279**	0.113	**0.161**	**0.215**	**0.193**	**0.436**	**0.390**
Linear Mode 3	0.079	0.003	0.022	0.044	0.093	0.047	0.017	0.025	0.137	0.115	0.011	0.002

Table 2.4 Correlation coefficient values between first three linear orthogonal modes and ETC Activity time series for CESM1 LENS. Bold font indicates correlation values that are significant at the 99% confidence level

vi. A Link Between the Daily and Monthly Large-Scale Circulations

These three mechanisms discussed thus far for the generation of precipitation, localized vapor transport into the region from the Atlantic seaboard, reduced westerlies associated in part with extratropical cyclone activity, and remote vapor transport from the Gulf of Mexico (for the winter and fall periods), suggest a prominent role for certain LSMPs in creating favorable conditions by which these mechanisms can occur. Several studies (Bradbury et al. 2002b; A017; Suriano et al. 2018) have examined how the large-scale circulation can influence the amount of precipitation received in the Northeast. For this region, a dominant troughing pattern in the eastern United States is often responsible for overall precipitation, with trough strength having a seasonal dependence, and this pattern is accompanied by increased southerly ocean-enhanced vapor transport that extends along the Atlantic seaboard, increased easterly zonal flow, and strong surface lows into the northern portion of the region (A017; Agel et al. 2019). Additionally, the relative zonal position of the trough can act to modulate precipitation amounts, such that a more western (eastern) trough position is associated with greater (lower) monthly-averaged precipitation (Bradbury et al. 2002b). This last point is reasonable, as the most active midlatitude storm tracks occur directly downstream of troughs (Lau 1988; Cai and Van den Dool 1991), while areas just

upstream of troughs are accompanied by surface anticyclones and generally have drier conditions (Harman 1991). Based on our above discussion, these processes seem to be well-captured in part by our extracted linear orthogonal modes. Previous studies conducted at different timescales (daily for A017 and monthly for Bradbury et al. (2002b) and Suriano et al. (2018)) indicate a similar role for the large-scale circulation in influencing precipitation totals. The clustering methods used by A017 on daily data (to study extreme precipitation) demonstrate in part that wintertime strength and positioning of troughs can modulate precipitation amounts. A similar conclusion is reached by Bradbury et al. (2002b) when correlating monthly trough position and strength indices to monthly winter precipitation amounts, and Suriano et al. (2018) when examining monthly mid-tropospheric wave train patterns over North America. This likely suggests that monthly analyses such as ours, Bradbury et al. (2002b), and Suriano et al. (2018) are in fact representing more frequent occurrences of particular daily large-scale configurations. If a particular daily, large-scale pattern occurs more frequently in a month, it will have a higher representation in the monthly-averaged large-scale pattern for that month. In the context of studies such as A017 that examine the daily LSMPs associated with extreme precipitation, this indicates that more frequent occurrences of high precipitation-causing LSMPs in a given month will likely lead to increased precipitation totals for that month. There is thus a direct link between daily large-scale patterns and monthly large-scale patterns and the variability associated with monthly precipitation totals. As such, our analysis suggests that, with regards to eastern United States trough strength and positioning, higher precipitation totals are more likely in a large-scale environment with an enhanced ridge in the North Atlantic, well-defined storm tracks with more frequent storms, and increased southerly moisture transport. Conversely, we would expect drier conditions to be accompanied by a weaker

ridge in the North Atlantic, weakly-defined storm tracks with less frequent storms, and reduced southerly moisture transport.

2.4b – CESM1 LENS: Multiple Linear Regression Using Linear Modes to Predict PRECT

As discussed in the methodology in Section 2.3, the linear modes for each month are used as predictors for the corresponding $\hat{\mathbf{p}}^0$ for each month in a multiple linear regression (MLR) model. The R-squared value generated for each model, which accounts for the variance of the precipitation that can be explained by our predictors, provides us with an estimation of how well our linear mode time series are able to predict $\hat{\mathbf{p}}^0$ for each month. Following this approach, in all months, all of our linear mode time series are significant at the 99% confidence level (p-value < 0.01). R-squared values are listed in Table 2.1 and example scatterplots comparing observations to MLR predictions for January, May, July, and October are shown in Fig. 2.10.

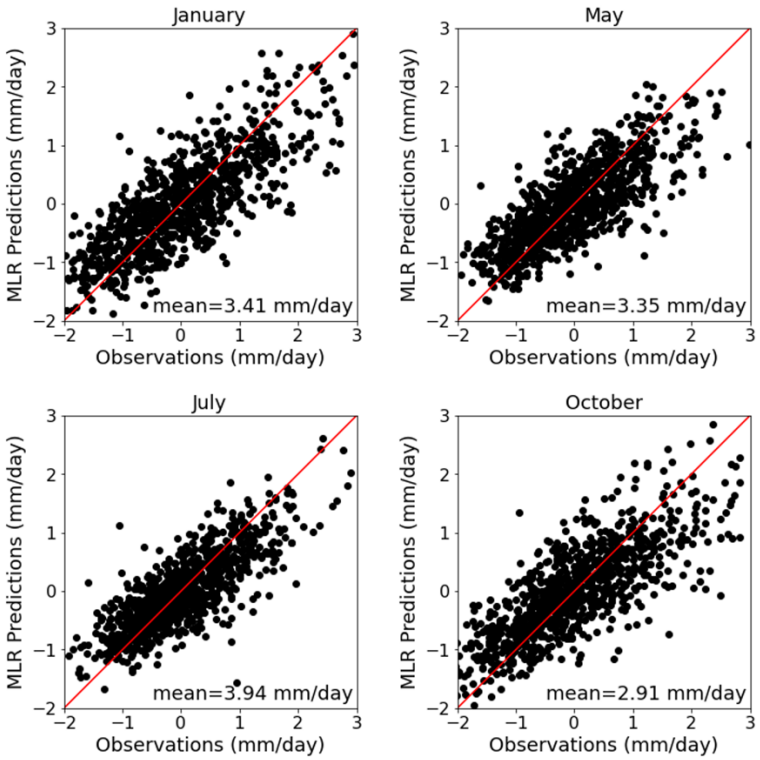

Fig. 2.10 Scatterplots for CESM1 LENS PRECT anomalies observations vs. MLR predictions for January, May, July and October. Red line in each frame represents the 1:1 line, and value in bottom right corner of each frame indicates the mean precipitation for that month

Predictability is somewhat similar across all calendar months, as the R-squared values range from 0.54 to around 0.65. Predictability is generally highest during the winter (December, January, February, and March) and early summer (June and July) seasons, and displays a noticeable decline for CESM1 LENS in April, May, August, and September. This raises the question as to what causes this decline in predictability? The decline can be explained by examining the seasonal cycle of precipitating days and precipitation intensity during these months. In April and May, there is a near peak in number of precipitating days, but a noticeable decline in precipitating intensity (A015). Mechanisms and processes such as blocking episodes, localized convection, and backdoor cold fronts are active features of the late spring period, and can contribute to consecutive days of light precipitation (i.e., more precipitating days with less intensity) (Bosart et al. 1973). Additionally, the April-May time period usually sees a shifting of the jet stream to a more northerly position, which can reduce the number of extratropical storms that move northward along the Atlantic seaboard (A015). This, combined with delayed warming due to cold ocean temperatures during the spring season (Trenberth et al. 2003), can limit precipitation intensity. In August and September, we see an opposite seasonal cycle behavior from that of April and May, in that there is a decline in number of precipitating days, but a near peak in precipitation intensity (A015). This indicates that some precipitation in August-September can tend to come from short-lived, intense systems such as mesoscale convective systems (Feng et al. 2019) or tropical cyclones (Barlow 2011).

Given the inherent interannual variability associated with the frequency and intensity of localized convection, fronts, and extratropical and tropical cyclones, and the infrequent and often spotty nature of MCSs, and the fact that the influence of these systems is not captured well in monthly data, this may explain in part the decline in linear predictability in the spring and summer periods. As discussed in A015, 50% of overall precipitation in the Northeast occurs as single-day events, and most extreme precipitation occurs over several multiday events. Additionally, Hawcroft et al. (2012) estimates that roughly 85% of total precipitation in DJF comes from extratropical storms. Similarly, Catto et al. (2012) find that cold fronts and warm fronts account for 28% and 29%, respectively, of midlatitude precipitation, with frontal activity accounting for 90% of extreme precipitation (Catto and Pfahl 2013). Given our analysis in this study, which is predicated on assessing monthly predictability of precipitation, it can be difficult to fully account for the sub-monthly time-scale processes discussed in these previous studies, as monthly averaging of precipitation totals will tend to partially dilute the impact of some high-precipitating events. We acknowledge this limitation, and would refer readers to the aforementioned studies for further discussion.

2.4c – Comparison Between CESM1 LENS, ERA5, and NOAA-CIRES-DOE 20CRv3

For the methods presented in Section 2.3, it is important to test whether the identified modes are reasonably consistent between the reanalysis products and CESM1 LENS. To validate this, the LOD method was applied to the data for ERA5, NOAA-CIRES-DOE 20CRv3 and CESM1 LENS. The results for each dataset are shown in Table 2.1 (CESM1 LENS), Table 2.2 (ERA5), and Table 2.3 (NOAA-CIRES-DOE 20CRv3). In terms of predictability, CESM1 LENS has a lower predictability range (determined by the R-squared values) of around 0.54 to 0.65, as

compared to the higher predictability range for ERA5 and NOAA-CIRES-DOE 20CRv3 of around 0.58 to 0.88. This is perhaps not surprising, as the two reanalysis products have a smaller sample size than CESM1 LENS, and thus a greater level of variability can be captured with fewer modes. More importantly, the lower predictability range for CESM1 LENS likely results from the model's internal variability with regards to representing the precipitation drivers. Overall, the maximum predictability afforded by the linear regression models for $\hat{\mathbf{p}}^0$ across all months and datasets (determined by the R-squared values) is limited to a value of 0.88. We hypothesize that this cap on linear predictability may be because the regional precipitation in the Northeast has inherent, complex variability (Ning and Bradley 2014) that cannot be fully captured by linear prediction methods.

Table 2.2: LOD Results for ERA5 (1950-2018)

	$d\hat{p}^1$	$d\hat{p}^2$	$d\hat{p}^3$	$d\hat{p}^4$	R-Squared Value
January	IVTn(69°W,40°N) 0.7071 [0.60,0.82] 50.0%	U850(70°W,46°N) 0.4780 [0.37,0.59] 22.8%	U850(122°E,25°N) 0.2293 [0.12,0.34] 5.3%	U850(18°E,13°N) 0.1810 [0.07,0.29] 3.3%	0.814
February	IVTn(71°W,44°N) 0.6525 [0.54,0.77] 42.6%	U850(103°W,22°N) 0.4276 [0.31,0.55] 18.3%	U850(71°E,41°N) 0.2937 [0.18,0.41] 8.6%	Z500(21°W,13°N) 0.2920 [0.18,0.41] 8.5%	0.780
March	IVTn(66°W,42°N) 0.5266 [0.39,0.66] 27.7%	U850(70°W,45°N) 0.4798 [0.35,0.61] 23.0%	U850(91°E,23°N) 0.3873 [0.25,0.52] 15.0%	Q850(178°W,15°N) 0.2395 [0.11,0.37] 5.7%	0.715
April	IVTn(69°W,41°N) 0.6635 [0.53,0.79] 44.0%	U850(66°W,45°N) 0.4085 [0.28,0.54] 16.7%	IVTn(93°E,39°N) 0.2636 [0.13,0.39] 6.9%	IVTe(48°E,27°N) 0.2266 [0.10,0.36] 5.1%	0.728
May	IVTn(67°W,43°N) 0.7061 [0.60,0.81] 49.9%	IVTe(67°W,35°N) 0.4215 [0.32,0.53] 17.8%	PSL(69°W,55°N) 0.3042 [0.20,0.41] 9.3%	PSL(12°W,15°N) 0.2338 [0.13,0.34] 5.5%	0.823
June	IVTn(65°W,44°N) 0.6028 [0.48,0.72] 36.3%	U850(71°W,46°N) 0.4446 [0.33,0.56] 20.0%	IVTe(71°W,39°N) 0.3621 [0.24,0.48] 13.1%	T2M(16°E,29°N) 0.2785 [0.16,0.40] 7.8%	0.770
July	IVTn(101°W,40°N) 0.6113 [0.45,0.77] 37.4%	U850(71°W,47°N) 0.3823 [0.22,0.54] 14.6%	PSL(127°E,35°N) 0.2401 [0.08,0.40] 5.8%		0.578
August	IVTn(71°W,40°N) 0.5323 [0.38,0.69] 28.3%	Q850(62°E,21°N) 0.4587 [0.31,0.61] 21.0%	T2M(177°E,16°N) 0.3569 [0.20,0.51] 12.7%		0.621
September	IVTn(70°W,39°N 0.5453 [0.41,0.68] 29.7%	U850(70°W,46°N) 0.4816 [0.35,0.61] 23.2%	U850(151°W,48°N) 0.3329 [0.20,0.47] 11.1%	IVTe(143°E,50°N) 0.2831 [0.15,0.42] 8.0%	0.720
October	IVTn(70°W,40°N) 0.6543 [0.54,0.77] 42.8%	U850(70°W,47°N) 0.4646 [0.35,0.58] 21.6%	Q850(124°W,28°N) 0.2977 [0.18,0.41] 8.9%	IVTn(100°E,9°N) 0.2351 [0.12,0.35] 5.5%	0.788
November	IVTn(71°W,39°N) 0.6535 [0.54,0.77] 42.7%	U850(70°W,47°N) 0.4781 [0.36,0.59] 22.8%	V850(93°E,51°N) 0.3045 [0.19,0.42] 9.3%	PSL(132°E,26°N) 0.2028 [0.09,0.32] 4.1%	0.789
December	IVTn(69°W,40°N) 0.7119 [0.63,0.80] 51.1%	U850(69°W,46°N) 0.4741 [0.38,0.56] 22.3%	Z500(114°W,37°N) 0.3377 [0.24,0.42] 11.0%	IVTe(19°E,23°N) 0.2082 [0.10,0.27] 3.4%	0.877

Table 2.2 Same as **Table 2.1**, but for ERA5 data

Table 2.3: LOD Results for NOAA-CIRES-DOE 20CRv3 (1950-2015)

	$d\hat{p}^1$	$d\hat{p}^2$	$d\hat{p}^3$	$d\hat{p}^4$	R-Squared Value
January	IVTn(71°W,39°N) 0.6280 [0.50,0.76] 39.4%	IVTn(104°W,52°N) 0.4260 [0.30,0.56] 18.2%	IVTe(110°E,39°N) 0.3259 [0.20,0.46] 10.6%	IVTn(126°W,2°N) 0.2556 [0.13,0.38] 6.5%	0.747
February	Q850(71°W,41°N) 0.6789 [0.55,0.81] 46.1%	T2M(92°W,42°N) 0.3864 [0.26,0.51] 14.9%	Q850(107°W,72°N) 0.2661 [0.14,0.39] 7.1%	Q850(89°W,12°N) 0.2651 [0.14,0.39] 7.0%	0.751
March	IVTn(70°W,39°N) 0.5420 [0.39,0.70] 29.4%	T2M(88°E,24°N) 0.3691 [0.21,0.52] 13.6%	IVTn(79°W,4°N) 0.3261 [0.17,0.48] 10.6%	IVTn(166°E,74°N) 0.3117 [0.16,0.47] 9.7%	0.633
April	IVTn(69°W,40°N) 0.7049 [0.58,0.83] 50.0%	U850(67°W,47°N) 0.3342 [0.21,0.46] 11.2%	PSL(100°E,21°N) 0.2690 [0.14,0.40] 6.4%	Q850(82°W,19°N) 0.2533 [0.12,0.38] 5.2%	0.728
May	IVTn(68°W,45°N) 0.6832 [0.57,0.80] 46.7%	U850(71°W,36°N) 0.4352 [0.32,0.55] 18.9%	T2M(140°E,61°N) 0.2966 [0.18,0.41] 8.8%	U850(100°E,48°N) 0.2270 [0.11,0.34] 5.2%	0.796
June	IVTn(68°W,42°N) 0.6114 [0.48,0.74] 37.4%	IVTe(74°W,37°N) 0.4232 [0.29,0.56] 17.9%	V850(137°E,11°N) 0.3236 [0.19,0.46] 10.5%	U850(82°E,44°N) 0.2733 [0.14,0.41] 7.5%	0.732
July	V850(73°W,39°N) 0.6938 [0.56,0.83] 48.1%	IVTe(8°W,34°N) 0.3812 [0.24,0.52] 14.5%	IVTn(109°W,31°N) 0.2713 [0.13,0.41] 7.4%		0.700
August	IVTn(73°W,39°N) 0.6064 [0.46,0.77] 36.8%	IVTn(22°E,40°N) 0.4004 [0.25,0.55] 16.0%	V850(67°E,32°N) 0.3562 [0.21,0.51] 12.7%		0.655
September	V850(71°W,40°N) 0.5827 [0.45,0.72] 34.0%	U850(69°W,48°N) 0.4522 [0.32,0.59] 20.5%	Q850(73°W,40°N) 0.3115 [0.18,0.45] 9.7%	Q850(141°E,12°N) 0.2913 [0.16,0.43] 8.5%	0.726
October	PSL(75°W,38°N) 0.6730 [0.54,0.81] 45.3%	IVTe(131°E,9°N) 0.3473 [0.21,0.48] 12.1%	PSL(58°W,39°N) 0.2903 [0.16,0.43] 8.4%	U850(169°W,39°S) 0.2503 [0.12,0.39] 6.3%	0.720
November	IVTn(74°W,35°N) 0.5516 [0.41,0.70] 30.4%	IVTe(76°W,48°N) 0.3913 [0.25,0.54] 15.3%	T2M(118°E,46°N) 0.3471 [0.20,0.49] 12.0%	U850(2°E,2°S) 0.3219 [0.18,0.47] 10.4%	0.682
December	V850(69°W,41°N) 0.6922 [0.58,0.81] 47.9%	Z500(123°W,46°N) 0.4378 [0.32,0.55] 19.2%	IVTn(98°E,40°N) 0.2738 [0.16,0.39] 7.5%	IVTe(86°W,44°N) 0.2334 [0.12,0.35] 5.4%	0.800

Table 2.3 Same as **Table 2.1**, but for NOAA-CIRES-DOE 20CRv3 data

Recall that in each iteration step of the LOD method, the selected time series of data (based on field and geographic location) is determined by absolute maximum correlation with the region-averaged precipitation anomaly time series. For each dataset in January, the first two iterations of

the methodology select for IVTn along the Atlantic seaboard and U850 in western New York for CESM1 LENS and ERA5, and IVTn for NOAA-CIRES-DOE 20CRv3, respectively. The third iteration selects for U850 in ERA5, IVTe in NOAA-CIRES-DOE 20CRv3, and IVTn in CESM1 LENS. The fourth iteration selects for U850 in ERA5, IVTn in NOAA-CIRES-DOE 20CRv3, and Z500 in CESM1 LENS. Although different fields and locations are selected for the latter modes, this does not necessarily indicate divergence in the meteorological patterns identified by these modes; it is instead largely indicative of strong correspondence between different fields and locations. By projecting these selected time series onto the 2D fields for each dataset, we can better ascertain similarities in the large-scale features that are selected within each dataset. Fig. 2.11 shows the projections onto the respective IVTn, Z500 and PRECT fields for each dataset for January (other fields and months are shown in the Online Resource). Visually, we see that there is good similarity across the three datasets for the correlation fields between the first two selected time series and the 2D fields. The visual similarity is reduced when examining the correlation fields between the third selected time series and the 2D fields. This similarity is quantitatively corroborated by calculating the spatial correlation in the domain of 25-60°N and 60-100°W between the three datasets (tabulated values for the first three linear orthogonal modes are shown in Section 2 of the Online Resource). This choice of domain allows us to account for how well the datasets compare with regards to capturing the large-scale features that influence precipitation in the Northeast. Generally, spatial correlation values are strongest during the fall and winter periods and for the first two linear orthogonal modes, with generally lower values during the spring and summer periods and for the third linear orthogonal mode. The fourth mode, however, exhibits very little visual or quantitative (not shown) similarity across the three datasets, which suggests that this mode is perhaps related to the inherent variability within each respective dataset. Interestingly, for

certain months, CESM1 LENS compares better with ERA5, and for other months, CESM1 LENS compares better with NOAA-CIRES-DOE 20CRv3, which again highlights some of the variability that exists across the three datasets. These results demonstrate several key points: 1) our methodology applies reasonably well to both reanalysis products and a large ensemble model dataset, and 2) the lack of consistency after the third iteration of the methodology amongst the three datasets suggests that the first three modes are the only modes that we can be reasonably confident in interpreting as drivers of precipitation in the Northeast.

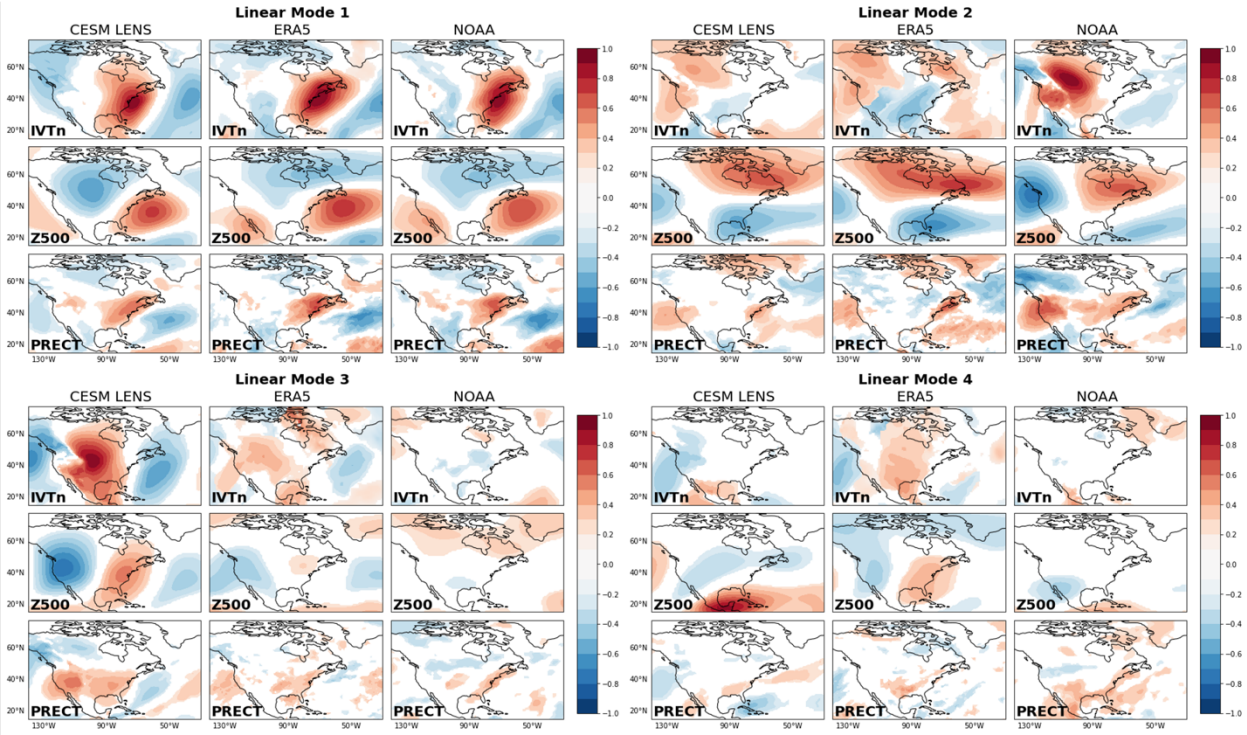

Fig. 2.11 Comparison for January between CESM1 LENS, ERA5, and NOAA-CIRES-DOE 20CRv3 for the projection of the first four linear orthogonal modes onto the respective IVTn, Z500, and PRECT fields. Contour shading indicates significance at the 95% confidence level

With regards to explained variance in January, ERA5 produces an R-squared value of 0.81, NOAA-CIRES-DOE 20CRv3 a value of 0.75, and CESM1 LENS a value of 0.64. The higher R-squared values associated with the reanalysis products begs the question as to whether there is

overfitting of the MLR model, due to the relatively small sample size of the reanalysis products. To determine whether overfitting is an issue here, a train/test procedure was used for the reanalysis results. For a given $\hat{\mathbf{p}}^0$ time series and the selected time series associated with each dataset, the data was partitioned, such that 80% of the data was used to train a linear model, and the remaining 20% was used to test the quality of the model. In order to get a robust result, 1000 random train/test samples were taken. The linear models were trained, and the test sets were used to see how well the models performed, as determined by the R-squared values from the 1000 samples. Nearly 40% of samples predict a R-squared value comparable to the R-squared value determined when all of the dataset is used. This seems to indicate that there is not an overfitting issue for the reanalysis datasets, and the increased level of predictability given by reanalysis products as compared to CESM1 LENS may be simply due to the difference in sample size and the overall methods used to generate the respective datasets.

Another question is whether the use of single ensemble members or smaller subsets of ensemble members (than using all 35) produce similar predictability and LOD modes to reanalysis, or are the shortcomings of the model output mitigated in part by using most of the ensemble members? To address this question, we implement the LOD method on single ensemble members and smaller non-overlapping groups of five and eleven ensemble members, respectively, and calculate the spatial correlation of the resulting LOD fields for Z500, IVTn, and PRECT compared to those of ERA5 in the domain of 25-60°N and 60-100°W. For individual ensemble members and some groupings of five and eleven ensemble members, R-squared values are comparable to that of ERA5, in the range of 0.65 to 0.95; however, the spatial correlation values are either small or negative for some of these, indicating that the LOD modes are not being captured well. Example scatterplot results for this approach in January are shown in Fig. 2.12. For all three fields and for

each of the linear modes, there is a broad range of spatial correlation values when considering individual ensemble members. This spread is reduced, and spatial correlation values are improved, as we include more ensemble members, with the best spatial correlation generally obtained when all 35 ensemble members are considered. This result highlights the usefulness and necessity of considering most of the ensemble members when working with CESM1 LENS. If one were to implement LOD on a single ensemble member at random, it could potentially lead to results that are unrepresentative of the larger ensemble. Given that there is good similarity between the results for the reanalysis products and CESM1 LENS, it is thus reasonable to suggest that use of the larger sample size of CESM1 LENS is a compromise between accurately capturing the LOD modes versus reduced predictability in terms of R-squared values relative to the reanalysis products.

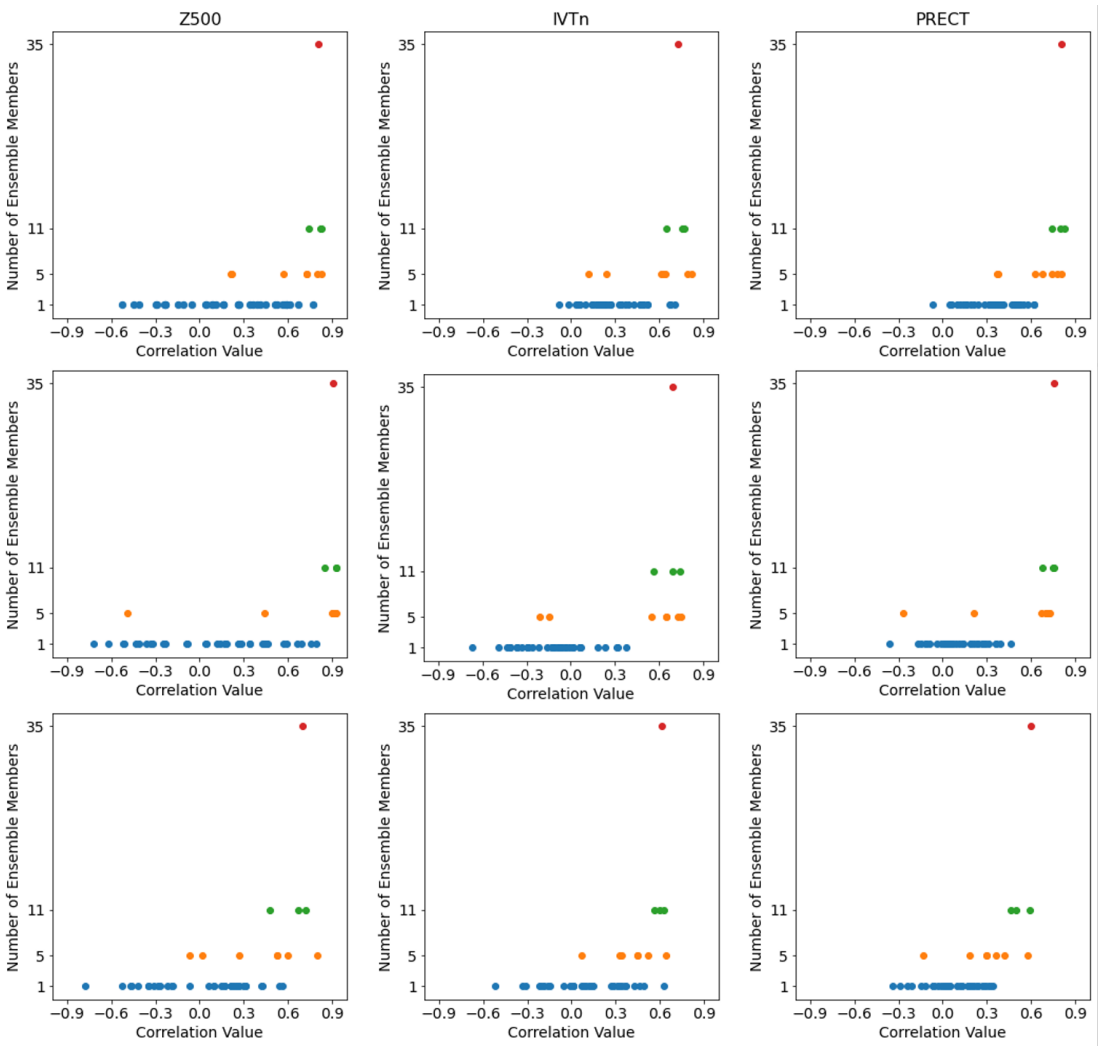

Fig. 2.12 Scatterplots of spatial correlation values between ERA5 and groups of 1, 5, 11, and all 35 ensemble members, respectively, from CESM1 LENS associated with January plots for Z500 (first column), IVTn (second column), and PRECT (third column). Rows in each column represent the first, second, and third linear modes, respectively

Overall, the consistency of the results across the datasets when our methodology is implemented provides confidence in its use. And again, the lack of consistency across the datasets once the third mode is extracted suggests that only three important modes are robust in our regional analysis. These findings demonstrate that the CESM1 LENS dataset approximates real-word observations reasonably well when a large sample size is considered, and thus can be useful for additional analyses related to understanding future precipitation conditions.

2.4d – CESM1 LENS: Multiple Linear Regression Using Climate Indices to Predict Linear Modes

As discussed in Ning and Bradley (2014), several modes of climate variability have important influences across the Northeast, and these influences manifest in certain LSMPs that act to suppress or enhance precipitation. For example, during years with high (above one standard deviation) NAO, there are significant high sea-level pressure anomalies over the northern part of the northeast United States, which can act to block winter storms from passing through and thus reduce wintertime precipitation (Ning et al. 2012b). Previous studies have also shown that the PNA pattern varies considerably with differences in tropical Pacific SST anomalies (Straus and Shukla 2002), and the PNA can, in turn, influence conditions over the Northeast. Overall, the three teleconnection patterns discussed above correspond to different placement and orientation of high pressure over North America, which can lead to different moisture transport patterns over the Northeast (Straus and Shukla 2000; 2002).

Following the methodology discussed in Section 2.3c, we can assess how well our linear modes and precipitation data can be predicted by the linear combination (MLR) of some of these teleconnection patterns. Generally speaking, the NAO, PNA, and ENSO serve as statistically significant predictors (p-value < 0.01) in our MLR model. The predictability of our linear modes by these teleconnection patterns is given in the last column of Table 2.5, where the three rows for each month in that column represent the MLR R-squared value for the first, second and third linear modes, respectively. Our discussion here focuses on the winter and late fall periods, as these periods generally have the highest R-squared values from the MLR. This is perhaps not surprising, as precipitation variability in the late spring and summer seasons is less significantly related to the large-scale circulation than during the fall and winter periods (Ning et al. 2012a). In December, January, February, March, October, and November, the second and third modes are reasonably

predicted by some of the teleconnection patterns (Table 2.5). The result for March is not surprising, as winter conditions can persist into March over this region (Kunkel and Angel 1999; Bradbury et al. 2003). Recall that the second linear mode during the winter period is associated with extratropical cyclone activity south of the Northeast, and the third mode is associated with vapor transport from the Gulf of Mexico. Our results here are in agreement with those of previous studies such as Straus and Shukla (2002), Ning and Bradley (2014), and Risser et al. (2021) regarding the role of the NAO, PNA, and ENSO in influencing wintertime precipitation totals over the Northeast by modulating cyclone development and the 3D circulation.

Table 2.5: CESM1 LENS MLR Results Including Teleconnection Patterns

	Predictability w/ LOD Modes	Predictability w/ Teleconnection Patterns	Predictability w/ LOD Modes + Teleconnection Patterns	Predictability of LOD Modes Using Teleconnection Patterns
January	0.624	0.109	0.635	0.116 0.160 0.117
February	0.628	0.087	0.630	0.023 0.253 0.332
March	0.619	0.071	0.624	0.023 0.267 0.330
April	0.580	0.054	0.591	0.015 0.117 0.132
May	0.600	0.043	0.602	0.025 0.088 0.036
June	0.643	0.019	0.646	0.013 0.059 0.013
July	0.646	0.053	0.650	0.032 0.011 0.104
August	0.565	0.035	0.569	0.016 0.033 0.216
September	0.527	0.010	0.532	0.048 0.041 0.027
October	0.603	0.032	0.607	0.049 0.030 0.174
November	0.572	0.055	0.577	0.024 0.193 0.231
December	0.599	0.062	0.607	0.079 0.163 0.231

Table 2.5 Multiple linear regression results related to teleconnection patterns for CESM1 LENS. First column is the predictability of precipitation using the first three linear modes from the linear orthogonal decomposition method only. Second column is the predictability of precipitation using only the teleconnection patterns. Third column is the combined predictability of precipitation using both the first three linear modes from the linear orthogonal decomposition method and the teleconnection patterns. Fourth column is the predictability of the linear modes from the linear orthogonal decomposition method using only the teleconnection patterns. Rows in the fourth column are the predictability (R-squared value) for the first, second, and third linear modes, respectively. Listed R-squared values reflect significance at the 99% confidence level

The teleconnection patterns are not good predictors of $\hat{\mathbf{p}}^0$ (second column of Table 2.5), as R-squared values are generally small. This result is in agreement with previous studies such as

Bradbury et al. (2002a) and Archambault et al. (2008) that did not find robust direct correlations between total winter precipitation and individual teleconnection patterns. As we have shown, different teleconnection patterns can have important influences on different precipitation modes that are decomposed from the total precipitation field. Additionally, it appears that many of these teleconnection patterns act only to influence the 3D circulation (i.e., zonal and meridional flow, trough/ridge location, etc..) and not necessarily the moisture processes that are most important for precipitation development. As discussed earlier in Section 2.4 and reiterated here, these teleconnection patterns seem to manifest themselves via the large-scale circulation. This is confirmed by including the indices for the teleconnection patterns as predictors along with the LOD selected time series in the MLR models to predict $\hat{\mathbf{p}}^0$ (third column of Table 2.5). The addition of the climate modes does not lead to a substantial increase in the predictability of $\hat{\mathbf{p}}^0$ (this predictability is given in the first column of Table 2.5, using the first three linear orthogonal modes), and this reinforces the point that their influence is already encapsulated in our extracted modes. This point is further reinforced by generating composites for the Z500 field associated with +/- 1 standard deviation of our linear orthogonal mode time series, and then comparing those composites with corresponding ones associated with +/- 1 standard deviation for the time series for NAO, Nino3.4, and PNA. This comparison is quantified by calculating the spatial correlation across the composites in the domain of 25-60°N and 60-100°W (tabulated spatial correlation values given in Section 3 of the Online Resource). Focusing on the winter period (December-March), there is excellent correlation between the linear orthogonal mode composites and the climate mode composites (magnitude of correlation values in the range of around 0.60-0.90). Generally, it seems as though the teleconnection patterns drive the large-scale circulation in which our linear orthogonal modes are embedded, but the circulation itself does not necessarily drive precipitation.

Instead, the large-scale circulation acts to generate environments that are conducive (or not conducive) for precipitation to occur.

2.5 – Summary and Discussion

The present study aims to build upon the existing literature related to assessing the large-scale drivers associated with monthly precipitation variability in the Northeast via the use of a novel linear orthogonal decomposition method.

The results of our analysis are summarized in part here:

1) During the winter (Figs. 2.1, 2.2, and 2.3) and fall periods (available in the Online Resource), the dominant, large-scale atmospheric drivers of monthly precipitation variability in the Northeast are integrated vapor transport northward along the Atlantic seaboard (first linear mode), extratropical cyclone activity (second linear mode) and associated frontal systems, and integrated vapor transport from the Gulf of Mexico (third linear mode). In the summer season (Figs. 2.7 and 2.8), while vapor transport along the Atlantic seaboard is still important, extratropical cyclone activity is reduced, and the third linear mode is difficult to physically interpret, although we believe it may be related to MCSs. As constructed, these modes are linearly independent from one another, and so multiple such modes over a given month can contribute to precipitation totals for that month.
2) MLR models, based on using the LOD modes as predictors, are able to predict monthly, region-averaged precipitation totals reasonably well, with R-squared values in the range of around 0.54 to 0.65 for CESM1 LENS (Table 2.1), and higher values in the range of 0.58 to 0.88 for the ERA5 (Table 2.2) and NOAA-CIRES-DOE 20CRv3 (Table 2.3) reanalysis products. Predictability is generally best during the late fall / winter and early to mid-summer periods,

and is generally lowest during April-May and August-September for CESM1 LENS, due in part to the seasonal cycle of precipitation in the region and the diluted influence of sub-monthly time scale systems in the monthly averaging. Overall, the cap on linear predictability may be related to the inherent, complex variability of regional precipitation that cannot be fully encapsulated by linear prediction methods.

3) CESM1 LENS compares reasonably well with reanalysis products both in terms of their linear orthogonal modes, and also in the projection of those modes onto the atmospheric fields we have considered (Fig. 2.11). The first three linear orthogonal modes (or two, in the summer period) are very similar between the three datasets we have analyzed, with significant divergence only occurring with the fourth linear mode across all three datasets. With the inherent variability associated with the fourth linear mode across all three datasets, we conclude that the first three linear modes are likely the most important for understanding the processes associated with monthly precipitation in the Northeast.

4) The large-scale atmospheric drivers of Northeast precipitation, particularly those associated with the second and third linear orthogonal modes, are linked in some capacity with the NAO, ENSO, and PNA (Table 2.5). We can conclude that the mechanisms by which these teleconnection patterns influence monthly precipitation totals over the region are through modification of the intensity and frequency of the linear orthogonal modes. That is, the teleconnection patterns influence the linear orthogonal modes, which in turn influence the monthly precipitation totals.

Our results are in general agreement with the existing literature related to understanding monthly precipitation variability in the Northeast. While we have not specifically examined smaller-scale phenomena (besides ETCs) that can contribute to this variability, our linear modes

indicate that the modulation of precipitation totals in the region are directly linked with the large-scale circulation. In favorable large-scale environments, phenomena such as ETCs, MCSs, and localized convection are likely to occur more frequently, resulting in greater monthly precipitation totals. By contrast, if the large-scale environment is not conducive to the development of these systems, then monthly precipitation totals on average would be reduced. In the context of the drivers within these large-scale environments, as the analysis of our linear modes indicates, there seems to be some seasonal differences in the manifestation of certain drivers. While the three linear modes for winter and fall are robust and are easily interpreted physically by examining our figures, it is more difficult to gain physical insight into the processes associated with the third linear mode in the spring and summer periods. We hypothesize that these seasonal differences may be due in part to the difference in jet stream behavior, as the jet stream is stronger and more easily identified in the cold seasons, and as such the large-scale circulation is also more clearly defined. Additionally, these seasonal differences occur across the three datasets we have analyzed, thus ruling out any product-specific deficiency. We have proposed several mechanisms to explain this third mode in the spring and summer periods, but since this mode contributes little to the precipitation variability in these seasons, and tends to vary in structure between the data products, it is unclear if it conveys any physical meaning about the upstream drivers of monthly precipitation.

The findings presented here also provide several opportunities for further work. The applicability of our linear orthogonal decomposition technique to both reanalysis data and model output provides confidence in the reliability of CESM1 LENS in replicating observations. Given this reliability, CESM1 LENS data can be used, and our analysis can be extended, to examine precipitation characteristics and the associated large-scale drivers in the Northeast in the near-future and far-future. Such a study could be a valuable resource for future, regional water

management practices in the face of ongoing anthropogenic climate change. Furthermore, our methodology can be reasonably applied to other regions of the world as well. Doing so can provide insight into the precipitation characteristics of those regions, as well as the LSMPs that modulate those characteristics. Finally, as touched on briefly in our discussion, our analysis in this study is linked to linear predictability – it is nonetheless relevant to understand how much additional predictability could be afforded if a nonlinear approach, such as a machine learning model, were employed.

2.6 – Appendix A

Linear Orthogonal Decomposition (LOD)

We begin with local precipitation time series vector $\mathbf{p}$ with components $p_k = p(t_k)$ and associated 2D field time series $\mathbf{F}_i(\mathbf{x}_j)$ with components $\mathbf{F}_i(t_k,\mathbf{x}_j)$. Here t_k and $\mathbf{x}_j$ denote temporal and spatial coordinates, respectively. In this study, time is discretized at the monthly time scale, but this method can be applied to other time scales.

The first step involves removal of a reference field (here taken to be the climatological mean) along the time axis in both precipitation and 2D fields:

$$\hat{\mathbf{p}}^0 = \mathbf{p} - \mathrm{E}[\mathbf{p}], \qquad \hat{\mathbf{F}}_i(t_k,\mathbf{x}_j) = \mathbf{F}_i(\mathbf{x}_j) - \mathrm{E}[\mathbf{F}_i(\mathbf{x}_j)]$$

If an obvious and undesired trend is present in the time series, it can be removed by using a time-dependent linear field instead. Here we can interpret the quantity $\hat{\mathbf{p}}^{\mathrm{n}}$ as the component of the precipitation time series that is unpredicted at stage n (this is the whole precipitation time series at stage 0). To proceed, we perform an iterative process analogous to a Gram-Schmidt decomposition. Specifically, we iterate over the following three steps (n = 1,…,N), where N is the termination point:

1. Calculate correlation between $\widehat{\mathbf{p}}^n$ and $\widehat{\mathbf{F}}_i(\mathbf{x}_j)$ at each point (the value of the correlation field should be between -1 and 1):

$$c^n(\mathbf{x}_j) = \frac{\widehat{\mathbf{p}}^{n-1} \cdot \hat{\mathbf{F}}_i(\mathbf{x}_j)}{\mathrm{StdDev}[\widehat{\mathbf{p}}^{n-1}] \cdot \mathrm{StdDev}[\hat{\mathbf{F}}_i(\mathbf{x}_j)]}$$

2. Identify the point of maximum absolute correlation x^n in field i^n. Define the predicted component of the precipitation field from this point as:

$$\mathbf{d}\widehat{\mathbf{p}}^n = c^n(\mathbf{x}^n)[\hat{\mathbf{F}}_{i^n}(\mathbf{x}^n) - \sum_{m=1}^{n-1} \frac{\hat{\mathbf{F}}_{i^n}(\mathbf{x}^n) \cdot \mathbf{d}\widehat{\mathbf{p}}^m}{\mathbf{d}\widehat{\mathbf{p}}^m \cdot \mathbf{d}\widehat{\mathbf{p}}^m} \mathbf{d}\widehat{\mathbf{p}}^m]$$

Note that $\mathbf{d}\widehat{\mathbf{p}}^n$ here is multiplied by the correlation by convention.

3. Calculate the remaining unpredicted component of the precipitation:

$$\widehat{\mathbf{p}}^n = \widehat{\mathbf{p}}^0 - \sum_{m=1}^{n} \frac{\widehat{\mathbf{p}}^0 \cdot \mathbf{d}\widehat{\mathbf{p}}^m}{\mathbf{d}\widehat{\mathbf{p}}^m \cdot \mathbf{d}\widehat{\mathbf{p}}^m} \mathbf{d}\widehat{\mathbf{p}}^m = \widehat{\mathbf{p}}^{n-1} - \frac{\widehat{\mathbf{p}}^0 \cdot \mathbf{d}\widehat{\mathbf{p}}^n}{\mathbf{d}\widehat{\mathbf{p}}^n \cdot \mathbf{d}\widehat{\mathbf{p}}^n} \mathbf{d}\widehat{\mathbf{p}}^n$$

As this is an orthogonal decomposition, the following properties should hold for each step of the process:

(a) $\mathrm{E}[\mathbf{d}\widehat{\mathbf{p}}^n] = 0$ and $\mathrm{E}[\widehat{\mathbf{p}}^n] = 0$

(b) $\mathbf{d}\widehat{\mathbf{p}}^m \cdot \mathbf{d}\widehat{\mathbf{p}}^n = 0$ for $n \neq m$

(c) $\widehat{\mathbf{p}}^n \cdot \mathbf{d}\widehat{\mathbf{p}}^m = 0$ for $m < n$

(d) $||\widehat{\mathbf{p}}^m||^2 > ||\widehat{\mathbf{p}}^n||^2$ for $m < n$

By orthogonality of $\mathbf{d}\widehat{\mathbf{p}}^n$ and using $\mathrm{E}[\mathbf{d}\widehat{\mathbf{p}}^n] = 0$, we have

$$\mathrm{Var}[\sum_{m=1}^{n} \frac{\widehat{\mathbf{p}}^0 \cdot \mathbf{d}\widehat{\mathbf{p}}^m}{\mathbf{d}\widehat{\mathbf{p}}^m \cdot \mathbf{d}\widehat{\mathbf{p}}^m} \mathbf{d}\widehat{\mathbf{p}}^m] = \sum_{m=1}^{n} \left(\frac{\widehat{\mathbf{p}}^0 \cdot \mathbf{d}\widehat{\mathbf{p}}^m}{\mathbf{d}\widehat{\mathbf{p}}^m \cdot \mathbf{d}\widehat{\mathbf{p}}^m}\right)^2 \mathrm{Var}[\mathbf{d}\widehat{\mathbf{p}}^m]$$

$$= \frac{1}{N-1} \sum_{m=1}^{n} \frac{(\widehat{\mathbf{p}}^0 \cdot \mathbf{d}\widehat{\mathbf{p}}^m)^2}{\mathbf{d}\widehat{\mathbf{p}}^m \cdot \mathbf{d}\widehat{\mathbf{p}}^m}$$

where N is the number of elements in $\mathbf{d}\widehat{\mathbf{p}}^m$.

Using $\mathrm{E}[\mathbf{d}\widehat{\mathbf{p}}^n] = 0$, we have

$$\mathrm{Var}[\widehat{\mathbf{p}}^0] = \frac{1}{N-1}(\widehat{\mathbf{p}}^0 \cdot \widehat{\mathbf{p}}^0)$$

Combining these equations, the total fraction of variance (*fov*) explained at stage n of the process is given by:

$$fov = \sum_{m=1}^{n} fov^m \quad \text{where} \quad fov^m = \frac{(\hat{\mathbf{p}}^0 \cdot \mathbf{d}\hat{\mathbf{p}}^m)^2}{(\hat{\mathbf{p}}^0 \cdot \hat{\mathbf{p}}^0)(\mathbf{d}\hat{\mathbf{p}}^m \cdot \mathbf{d}\hat{\mathbf{p}}^m)}$$

The total fraction of variance is equal to the R-squared provided by an MLR model acting either on time series $\{\mathbf{d}\hat{\mathbf{p}}^1,\ldots,\mathbf{d}\hat{\mathbf{p}}^n\}$ or $\{\hat{\mathbf{F}}_{i^1}(\mathbf{x}^1),\ldots,\hat{\mathbf{F}}_{i^n}(\mathbf{x}^n)\}$.

2.7 – References

Agel L, Barlow M, Qian J-H, Colby F, Douglas E, Eichler T (2015) Climatology of daily precipitation and extreme precipitation events in the northeast United States. J Hydrometeorol 16:2537– 2557. doi:10.1175/JHM-D-14-0147.1

Agel L, Barlow M, Feldstein SB, Gutowski WJ (2017) Identification of large-scale meteorological patterns associated with extreme precipitation in the US northeast. Clim Dyn. doi:10.1007/s00382-017-3724-8

Agel L, Barlow M, Colby F, et al. (2019) Dynamical analysis of extreme precipitation in the US northeast based on large-scale meteorological patterns. Clim Dyn 52, 1739–1760 doi:10.1007/s00382-018-4223-2

Archambault HM, Bosart LF, Keyser D, and Aiyyer AR (2008) Influence of large-scale flow regimes on cool-season precipitation in the northeastern United States, Mon. Weather Rev., 136, 2945–2963. doi:10.1175/2007MWR2308.1

Barlow M (2011) Influence of hurricane-related activity on North American extreme precipitation. Geophys. Res. Lett., 38, L04705. doi:10.1029/2010GL046258.

Barnston AG and Livezey RE (1987) Classification, seasonality, and persistence of low-frequency atmospheric circulation patterns, Mon. Weather Rev., 115, 1083–1126. doi:10.1175/1520-0493(1987)115<1083:CSAPOL>2.0.CO;2

Bosart, LF, Pagnotti V, and Lettau B (1973) Climatological aspects of eastern United States back-door cold frontal passages. Mon. Wea. Rev., 101, 627–635, doi:10.1175/1520-0493(1973)101,0627:CAOEUS.2.3.CO;2.

Bradbury JA, Dingman SL, and Keim BD (2002a) New England drought and relations with larger scale atmospheric circulation patterns, J. Am. Water Resour. Assoc., 38, 1287–1299.

doi:10.1111/j.1752-1688.2002.tb04348.x

Bradbury JA, Keim BD, and Wake CP (2002b) U.S. east coast trough indices at 500 hPa and New England winter climate variability, J. Clim., 15, 3509–3517. doi:10.1175/1520-0442(2002)015<3509:USECTI>2.0.CO;2

Bradbury JA, Keim BD, and Wake CP (2003) The influence of regional storm tracking and teleconnections on winter precipitation in the Northeastern United States, Ann. Assoc. Am. Geogr., 93, 544–556. doi:10.1111/1467-8306.9303002.

Cai M and van den Dool HM (1991) Low-frequency waves and traveling storm tracks. Part I: Barotropic component. J. Atmos. Sci., 48, 1420–1436. doi:10.1175/1520-0469(1991)048%3C1420:LFWATS%3E2.0.CO;2

Catto JL, Pfahl S, Jakob C, Berry G, and Nicholls N (2012) Relating global precipitation to atmospheric fronts. Geophys. Res. Lett., 39, L10805, doi:10.1029/2012GL051736.

Catto JL and Pfahl S (2013) The importance of fronts for extreme precipitation. J. Geophys. Res. Atmos., 118, 10791– 10 801, doi:10.1002/jgrd.50852.

DeGaetano AT (2009) Time-dependent changes in extreme- precipitation return-period amounts in the continental United States. J. Appl. Meteor. Climatol., 48, 2086–2099, doi:10.1175/2009JAMC2179.1.

Feng Z et al (2019) Spatiotemporal characteristics and large-scale environments of mesoscale convective systems east of the Rocky Mountains. Journal of Climate, 32(21), 7303–7328. doi:10.1175/JCLI-D-19-0137.1

Grotjahn R et al (2016) North American extreme temperature events and related large scale meteorological patterns: a review of statistical methods, dynamics, modeling, and trends. Clim Dyn 46:1151–1184. doi:10.1007/s00382-015-2638-6

Harman JR (1991) Synoptic Climatology of the Westerlies: Process and Patterns. Association of American Geographers, 80 pp.

Hartley S and Keables MJ (1998) Synoptic associations of winter climate and snowfall variability in New England, USA, 1950–1992, Int. J. Climatol., 18, 281–298. doi:10.1002/(SICI)1097-0088(19980315)18:3<281::AID-JOC245>3.0.CO;2-F

Hawcroft MK, Shaffrey LC, Hodges KI, and Dacre HF (2012) How much Northern Hemisphere precipitation is associated with extratropical cyclones? Geophys. Res. Lett., 39, L24809, doi:10.1029/2012GL053866.

Hayhoe K, Wake CP, Huntington TG, et al. (2007) Past and future changes in climate and hydrological indicators in the US Northeast. Clim Dyn 28, 381–407. https://doi.org/10.1007/s00382-006-0187-8

Hersbach H and Coauthors (2020) The ERA5 global reanalysis. Quart. J. Roy. Meteor. Soc., doi:10.1002/qj.3803

Hoskins BJ and Hodges KI (2002) New perspectives on the northern hemi- sphere winter storm tracks. J Atmos Sci 59:1041–1061. https://doi.org/10.1175/1520-0469(2002)059<1041:npotnh>2.0.co;2

Howarth ME, Thorncroft CD, and Bosart LH (2019) Changes in extreme precipitation in the Northeast United States: 1979–2014. J. Hydrometeorol. 20, 673–689. doi:10.1175/JHM-D-18-0155.1

Hurrell JW (1995) Decadal trends in the North Atlantic Oscillation: Regional temperature and precipitation, Science, 269, 676–679. doi:10.1126/science.269.5224.676

Kay JE, Deser C, Phillips A, Mai A, Hannay C, Strand G, Arblaster J, Bates S, Danabasoglu G, Edwards J, Holland M, Kushner P, Lamarque J-F, Lawrence D, Lindsay K, Middleton A,

Munoz E, Neale R, Oleson K, Polvani L, and Vertenstein M (2015) The Community Earth System Model (CESM1) Large Ensemble Project: A community resource for studying climate change in the presence of internal climate variability. Bulletin of the American Meteorological Society, 96, 1333–1349. doi:10.1175/BAMS-D-13-00255.1

Kocin PJ and Uccellini LW (2004) Northeast Snowstorms. Meteor. Monogr., No. 54, Amer. Meteor. Soc., 818 pp. doi:10.1007/978-1-878220-32-5

Kunkel KE and Angel JR (1999) Relationship of ENSO to snowfall and related cyclone activity in the contiguous United States, J. Geophys. Res., 104, 19,425–19,434, doi:10.1029/1999JD900010.

Kunkel KE, Andsager K, and Easterling DR (1999) Long-term trends in extreme precipitation events over the conterminous United States and Canada. J. Climate, 12, 2515–2527, doi:10.1175/1520-0442(1999)012,2515:LTTIEP.2.0.CO;2.

Kunkel KE, Easterling DR, Kristovich DAR, Gleason B, Stoecker L, and Smith R (2012) Meteorological causes of the secular variations in observed extreme precipitation events for the conterminous United States. J Hydrometeorol 13:1131–1141. https://doi.org/10.1175/ jhm-d-11-0108.1

Kunkel KE and Coauthors (2013a) Monitoring and understanding trends in extreme storms: State of knowledge. Bull. Amer. Meteor. Soc., 94, 499–514, doi:10.1175/BAMS-D-11-00262.1.

Kunkel KE and Coauthors (2013b) Regional climate trends and scenarios for the U.S. National Climate Assessment. Part 1. Climate of the Northeast U.S., NOAA Tech. Rep. NESDIS 142-1, 80 pp. [Available online at http://www.nesdis.noaa.gov/technical_reports/NOAA_NESDIS_Tech_Report_142-1-Climate_of_the_Northeast_U.S.pdf.]

Lau NC (1988) Variability of the observed midlatitude storm tracks in relation to low-frequency changes in the circulation pattern. J. Atmos. Sci., 45, 2718–2743. doi:10.1175/1520-0469(1988)045%3C2718:VOTOMS%3E2.0.CO;2

Leathers, DJ, Yarnal B, and Palecki MA (1991) The Pacific/North American teleconnection pattern and United States climate. Part I: Regional temperature and precipitation associations, J. Clim., 4, 517–528. doi:10.1175/1520-0442(1991)004<0517:TPATPA>2.0.CO;2

Lott N and Ross T (2006) Tracking and evaluating U. S. billion-dollar weather disasters, 1980–2005. AMS Forum: Environ- mental Risk and Impacts on Society: Successes and Challenges, Atlanta, GA, Amer. Meteor. Soc., 1.2. [Available online at https://ams.confex.com/ams/Annual2006/techprogram/ paper_100686.htm.]

Melillo, JM, Richmond TC, and Yohe GW (2014) Climate Change Impacts in the United States: The Third National Climate Assessment. U.S. Global Change Research Program, 841 pp., doi:10.7930/J0Z31WJ2.

Milrad SM, Atallah EH, Gyakum JR, Dookhie G (2014) Synoptic typing and precursors of heavy warm-season precipitation events at Montreal, Québec. Weather Forecast 29:419–444. doi:10.1175/WAF-D-13-00030.1

Namias J (1966) Nature and possible causes of the northeastern United States drought during 1962–1965, Mon. Weather Rev., 94, 543–554. doi:10.1175/1520-0493(1966)094<0543:NAPCOT>2.3.CO;2

Ning L and Bradley RS (2014) Winter precipitation variability and corresponding teleconnections over the northeastern United States, J. Geophys. Res. Atmos., 119, 7931–7945, doi:10.1002/ 2014JD021591.

Ning L, Mann ME, Crane R, and Wagener T (2012a) Probabilistic projections of climate change for the mid-Atlantic region of the United States—Validation of precipitation downscaling during the historical era, J. Clim., 25, 509–526. doi:10.1175/2011JCLI4091.1

Ning L, Mann ME, Crane R, Wagener T, Najjar RG, and Singh R (2012b) Probabilistic projections of anthropogenic climate change impacts on precipitation for the mid-Atlantic region of the United States, J. Clim., 25, 5273–5291. doi:10.1175/JCLI-D-11-00565.1

Pfahl S and Wernli H (2012) Quantifying the relevance of cyclones for precipitation extremes. J. Climate, 25, 6770–6780, doi:10.1175/JCLI-D-11-00705.1.

Pfahl S and Sprenger M (2016) On the relationship between extratropical cyclone precipitation and intensity. Geophys Res Lett 43:1752– 1758. https://doi.org/10.1002/2016GL068018

Pryor SC, Howe JA, and Kunkel KE (2009) How spatially coherent and statistically robust are temporal changes in extreme precipitation in the contiguous USA? Int. J. Climatol., 29, 31–45, doi:10.1002/joc.1696.

Risser MD, Wehner MF, O'Brien JP et al (2021) Quantifying the influence of natural climate variability on in situ measurements of seasonal total and extreme daily precipitation. Clim Dyn 56, 3205–3230. doi:10.1007/s00382-021-05638-7

Ropelewski CF, and Halpert MS (1986) North American precipitation and temperature patterns associated with the El Niño/Southern Oscillation (ENSO), Mon. Weather Rev., 114, 2352–2361. doi:10.1175/1520-0493(1986)114<2352:NAPATP>2.0.CO;2

Schumacher RS, Johnson RH (2005) Organization and environmental properties of extreme-rain-producing mesoscale convective systems. Mon Weather Rev 133:961–976. doi:10.1175/MWR2899.1

Seager R, Pederson N, Kushnir Y, Nakamura J, and Jurburg S (2012b) The 1960s drought and the subsequent shift to a wetter climate in the Catskill Mountains Region of the New York City watershed, J. Clim., 25, 6721–6742. doi:10.1175/JCLI-D-11-00518.1

Slivinski LC, Compo GP, Whitaker JS, Sardeshmukh PD, Giese BS, McColl C, Allan R, Yin X, Vose R, Titchner H, Kennedy J, Spencer LJ, Ashcroft L, Brönnimann S, Brunet M, Camuffo D, Cornes R, Cram TA, Crouthamel R, Domínguez-Castro F, Freeman JE, Gergis J, Hawkins E, Jones PD, Jourdain S, Kaplan A, Kubota H, Le Blancq F, Lee T, Lorrey A, Luterbacher J, Maugeri M, Mock CJ, Moore GK, Przybylak R, Pudmenzky C, Reason C, Slonosky VC, Smith C, Tinz B, Trewin B, Valente MA, Wang XL, Wilkinson C, Wood K and Wyszyński P (2019) Towards a more reliable historical reanalysis: Improvements for version 3 of the Twentieth Century Reanalysis system. Q J R Meteorol Soc. (accepted) doi:10.1002/qj.3598.

Straus DM and Shukla J (2000) Distinguishing between the SST-forced variability and internal variability in mid latitudes: Analysis of observations and GCM simulations, Q. J. R. Meteorol. Soc., 126, 2323–2350. doi:10.1002/qj.49712656716

Straus DM and Shukla J (2002) Does ENSO force the PNA?, J. Clim., 15, 2340–2358. doi: 10.1175/1520-0442(2002)015<2340:DEFTP>2.0.CO;2

Suriano ZJ, Benjamin AE, Leathers DJ, Schroeter D, and Corradina V (2018) Northeast United States growing season moisture conditions: Associations with a North American mid-tropospheric wave train. Int J Climatol. 38:5542–5550. doi:10.1002/joc.5746

Trenberth KE (1997) The definition of El Niño, Bull. Am. Meteorol. Soc., 78, 2771–2777. doi:10.1175/1520-0477(1997)078<2771:TDOENO>2.0.CO;2

Trenberth KE, Dai A, Rasmussen RM, and Parsons DB (2003) The changing character of precipitation. Bull. Amer. Meteor. Soc., 84, 1205–1217, doi:10.1175/ BAMS-84-9-1205.

Ullrich PA and Zarzycki CM (2017) TempestExtremes: a framework for scale-insensitive pointwise feature tracking on unstructured grids, Geosci. Model Dev., 10, 1069–1090, https://doi.org/10.5194/gmd-10-1069-2017, 2017.

Wallace JM and Gutzler DS (1981) Teleconnections in the geopotential height field during the Northern Hemisphere winter, Mon. Weather Rev., 109, 784–812. doi:10.1175/1520-0493(1981)109<0784:TITGHF>2.0.CO;2

Chapter 3 – Two Large-Scale Meteorological Patterns are Associated with Short-Duration Dry Spells in the Northeastern United States

Abstract

Large-scale meteorological pattern (LSMP) – based analysis is used novelly to understand meteorological conditions before and during short-duration dry spells over the northeastern United States. These LSMPs are useful to assess models and select better-performing models for future projections. Dry spell events are identified from histograms of consecutive dry days below a daily precipitation threshold. Events lasting twelve days or longer, which correspond to ~10% of dry spell events, are examined. The 500-hPa stream function anomaly fields for the first twelve days of each event are time-averaged and *k*-means clustering is applied to isolate the dry spell-related LSMPs. The first cluster has a strong, low-pressure anomaly over the Atlantic Ocean, southeast of the region, and is more common in winter and spring. The second cluster has strong, high-pressure over east-central North America and is most common during autumn. Over the region, both clusters have negative specific humidity anomalies, negative integrated vapor transport from the north, and subsidence associated with a midlatitude jet stream dipole structure that reinforces upper-level convergence. Subsidence is supported by cold air advection in the first cluster and the location on the east side of the lower-level high pressure in the second cluster. Extratropical cyclone storm tracks are generally shifted southward of the region during the dry spells. Individual events lie on a continuum between two distinct clusters. These clusters have similar local, but different remote, properties. While dry spells occur with greater frequency during drought months, most dry spells occur during non-drought months.

3.1 – Introduction

The northeastern United States (hereafter, the Northeast) (Fig. 3.1, red box) is densely populated with many economic interests, all of which rely on a heavily managed water supply. However, precipitation in this region has been changing (Walsh et al. 2014). Despite a general wetting trend since the 1970s, climate change is expected to disrupt and strain the water supply in the Northeast (Horton et al. 2014), with rising temperatures causing increased evaporative demand, decreased winter snowpack, and earlier snowmelt (Trombulak and Wolfson 2004; Burns et al. 2007; Hayhoe et al. 2007; Xue and Ullrich 2021). Examining the large-scale meteorology associated with dry spells in this region fosters deeper understanding of the meteorological processes driving dryness, and can improve the predictability of anomalous meteorological conditions in a changing climate.

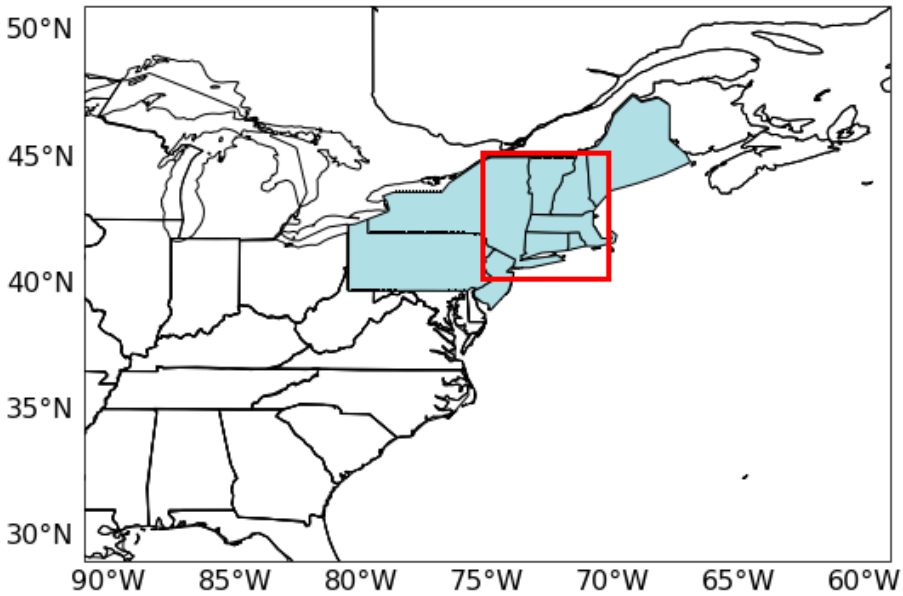

Fig. 3.1 Geographic domain used in the methodology discussed in Section 3.3. All or parts of the states shaded in blue have some contribution to the region used here. Area enclosed by the red box is the Northeast as defined for this study. Clustering domain used in Section 3.3 is 30-50°N / 60-90°W

The Northeast has experienced intermittent droughts (Seager et al. 2005b) including: 1980 (Namias 1982), 1988-1990 (Trenberth 1988), and 1998-2004 (Lyon et al. 2005; Seager 2007). The

most severe drought over this region in recent decades occurred from 1962 to 1966 (Namias 1966, 1983; Cook and Jacoby 1977). This drought has served as the standard for assessing future water management practices in the Northeast. Consequently, several studies (e.g., Namias 1966; Barlow et al. 2001; Seager et al. 2012) have focused on examining the unique large-scale meteorological conditions associated with this event. Many of the Northeast's water supply systems were constructed almost 70 years ago (Bone et al. 2006); since then both the number of consecutive dry days (Hatfield et al. 2014) and population have increased. Significant economic hardships and water supply strains could follow if drought events were to become more frequent, even if the climate is becoming wetter. However, long-term drought events in the Northeast are not associated with a single meteorological driver of persistent below-average precipitation. Instead, these events are often composed of short-term dry periods punctuated by occasional precipitation.

In contrast with longer-duration drought events, short-duration dry spells (events lasting at least a week to several weeks, but shorter than a drought timescale) are more amenable to dynamical analysis because they are dominated by a single meteorological pattern. Model simulations of future climate scenarios suggest that certain watersheds in the Northeast will experience more short-duration dry spells due to increased warming and evaporative demand (Hayhoe et al. 2007). Given the current dearth of studies related to understanding the large-scale meteorology associated with short-duration dry spells and the potential risks from an increase in these types of events, the goal of this present work is to fill an important knowledge gap by examining the large-scale meteorology associated with short-duration dry spells over the Northeast.

We focus on short-duration dry spells (i.e., sequential days with daily precipitation below a given threshold) and the meteorological conditions surrounding reduced precipitation in the

Northeast. We do not focus on "drought months" because we want to identify and study naturally-occurring dry periods of a specified rarity without the artificial constraints of when a month starts or ends. Additionally, our analysis of dry spells is distinguished from that for short-term flash droughts, the latter of which are heavily influenced by increased evaporative stress. For the Northeast, approximately 10% of dry spells last for twelve days or more. For assessing the large-scale meteorology, large-scale meteorological patterns (LSMPs; Grotjahn 2011; Grotjahn et al. 2016) analysis is implemented. LSMP analysis was previously applied to "instantaneous" fields. While time-averaged fields have been linked to LSMPs (Lee and Grotjahn 2019), this is the first study to apply LSMP analysis to time-averaged fields. This is also the first LSMP-based analysis of meteorological conditions associated with persistent dryness, and thus the LSMPs and large-scale meteorology described here may assist dry spell prediction.

The remainder of the paper is organized as follows. Datasets are described in Section 3.2. Methodology is discussed in Section 3.3. Results and analyses related to the dry spell LSMPs are provided in Section 3.4. The paper concludes with a summary and discussion in Section 3.5.

3.2 – Data

This study makes use of both daily gauge-based precipitation data and daily reanalysis data. The gauge-based precipitation data comes from the CPC Unified Gauge-Based Analysis of Daily Precipitation over CONUS (Xie et al. 2007). This precipitation data has 0.25° x 0.25° grid spacing, with a spatial domain of 20.125 – 49.875°N / 230.125 – 304.875°E. Reanalysis data are drawn from the ERA5 dataset (Hersbach et al. 2020) with 0.25° x 0.25° grid spacing and the full, global, spatial domain, for the 1961-2021 time period. From ERA5, both daily total fields and anomaly fields are considered for selected atmospheric variables. Before calculating daily anomalies for a particular field, the long-term daily mean of that field (January 1st – December

31st) is calculated and smoothed via Fourier-transform by retaining only the first four harmonics of the yearly cycle. Daily anomalies are then calculated by subtracting that Fourier-transformed long-term daily mean from the total field for individual days. Some of the atmospheric fields we consider include total precipitation, the 500 hPa geopotential height (Z500), 200 hPa zonal wind (U200), 850 hPa specific humidity (Q850), 700 hPa omega (ω700), vertically-integrated vapor transport (IVT) in the eastward and northward directions, and 925 hPa temperature advection (TA925). The 500 hPa stream function field (SF) is calculated via the windspharm Python package (Dawson 2016) using the zonal and meridional winds at 500 hPa.

3.3 – Methodology

3.3a – Event Isolation

Space and time criteria are used to identify short-duration dry spell events from the CPC Unified Gauge precipitation dataset to isolate those events in which most of the region experiences dry conditions at the same time. To begin, the precipitation data is area-averaged in the domain of 40–45°N / 70–75°W to generate a daily precipitation time series. This domain omits certain subregions that are in various definitions of "The Northeast" for two reasons. First, parts of a smaller region are more likely to have the simultaneous dry conditions than a large region. Second, results for parts of the Northeast outside our region might be estimated by "phase-shifting" our LSMPs. Next, we examine consecutive dry days (CDDs). Each "dry day" must have area-averaged precipitation below a threshold. Tested thresholds were: <1 mm, <2 mm, and <3 mm. Others have tested various thresholds; see discussion and additional references in Rivoire et al. (2019). We selected <2 mm of area-averaged precipitation to define our "dry day" to get both a larger sample size and longer periods of persistent dryness. We use area-averaged precipitation because we seek a persistent, broader-scale, quasi-stationary, meteorological pattern. Alternatively, low

accumulated precipitation, a more appropriate metric for longer-term drought periods, could emerge from intermittent meteorological patterns that may not be amenable to LSMP analysis. The frequency tabulation and duration lengths of these CDD events are shown in the histogram of Fig. 3.2. The distribution of CDD events approximately follows a geometric distribution fit (GDF) when considering events lasting ≥ 8 days (see Supplemental Materials). The GDF assumes no autocorrelation in the data, and when considering events lasting ≥ 1 to 7 day(s), respectively, autocorrelation in the data leads to the GDF overestimating the probability of these events. Additionally, the GDF to our data implies that there is no preferred CDD duration. Hence, our CDD events of interest are based upon the fraction of all CDDs greater than some threshold duration.

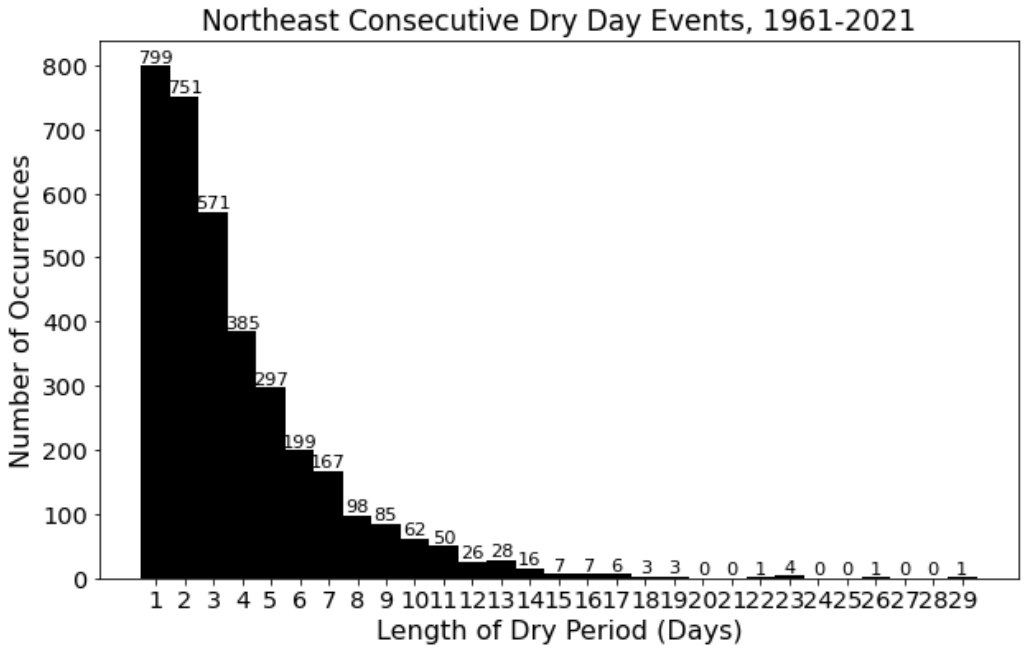

Fig. 3.2 Histogram distribution of consecutive dry day (CDD) events duration in the Northeast from 1961-2021. Lengths of events (in days) are given along the x-axis, with total number of occurrences given along the y-axis. Number on top of histogram bars indicates total count of events for that particular dry period length. Dry spells in this report are 12 days or longer

Looking at the right tail end of the distribution, the days within events lasting at least 12 days or longer account for roughly 10% of all "dry" days, according to our < 2 mm threshold. We thus define "short-duration dry spells" as CDD events in which the number of CDDs is ≥ 12 days. This choice reflects a compromise between obtaining a large enough sample for analysis, while also identifying events that are "extreme" in terms of an extended time with minimal precipitation. This process identifies 103 short-duration dry spell events. These events range in duration from 12 to 29 days. The start and end dates and duration of the 103 events are given in Table 3.1. This space and time method identifies short-duration dry spells, but it results in a small sample size of around 1.7 events per year. The reason behind choosing events that are so rare is that the dynamics associated with these dry spells are expected to have a stronger signal that distinguishes them from the "noise" of natural variability.

Event No.	Cluster	Event Start Date	Event End Date	Duration (days)
1	2	Jan 3rd, 1961	Jan 15th, 1961	13
2	2	Oct 16th, 1961	Oct 29th, 1961	14
3	1	Mar 14th, 1962	Mar 30th, 1962	17
4	1	Apr 15th, 1962	Apr 28th, 1962	14
5	2	Jun 27th, 1962	Jul 8th, 1962	12
6	1	Apr 5th, 1963	Apr 17th, 1963	13
7	2	Oct 5th, 1963	Oct 27th, 1963	23
8	2	Apr 24th, 1964	May 8th, 1964	15
9	1	Oct 4th, 1964	Oct 16th, 1964	13
10	--	*Mar 31st, 1965*	*Apr 11th, 1965*	*12*
11	2	Apr 28th, 1965	May 16th, 1965	19
12	--	*Jul 20th, 1965*	*Aug 1st, 1965*	*13*
13	1	Oct 24th, 1965	Nov 8th, 1965	16
14	1	Jan 10th, 1966	Jan 22nd, 1966	13
15	1	Mar 26th, 1966	Apr 7th, 1966	13
16	1	Apr 10th, 1966	Apr 21st, 1966	12
17	--	*Oct 21st, 1966*	*Nov 1st, 1966*	*12*
18	2	Nov 12th, 1966	Nov 25th, 1966	14
19	2	Jan 9th, 1967	Jan 26th, 1967	18
20	--	*May 27th, 1967*	*Jun 7th, 1967*	*12*
21	1	Feb 4th, 1968	Feb 29th, 1968	26
22	--	*Sep 13th, 1968*	*Sep 24th, 1968*	*12*
23	1	Mar 4th, 1969	Mar 19th, 1969	16
24	2	Oct 7th, 1969	Oct 19th, 1969	13
25	1	Jan 1st, 1970	Jan 17th, 1970	17
26	1	Apr 4th, 1970	Apr 19th, 1970	16
27	1	Mar 21st, 1971	Apr 2nd, 1971	13
28	--	*Apr 12th, 1971*	*Apr 24th, 1971*	*13*
29	2	Sep 22nd, 1971	Oct 5th, 1971	14

30	2	Oct 12th, 1971	Oct 23rd, 1971	12
31	--	*Nov 9th, 1971*	*Nov 21st, 1971*	*13*
32	1	Jan 5th, 1973	Jan 19th, 1973	15
33	2	Oct 7th, 1973	Oct 19th, 1973	13
34	--	*Oct 3rd, 1974*	*Oct 14th, 1974*	*12*
35	1	Oct 18th, 1974	Oct 30th, 1974	13
36	1	Apr 7th, 1975	Apr 18th, 1975	12
37	2	Jun 15th, 1975	Jun 28th, 1975	14
38	1	Apr 3rd, 1976	Apr 15th, 1976	13
39	1	Nov 7th, 1976	Nov 28th, 1976	22
40	2	Oct 21st, 1977	Nov 3rd, 1977	14
41	1	Feb 9th, 1978	Mar 3rd, 1978	23
42	1	Apr 22nd, 1978	May 4th, 1978	13
43	1	Jul 4th, 1979	Jul 15th, 1979	12
44	1	Jan 24th, 1980	Feb 15th, 1980	23
45	--	*Jan 18th, 1981*	*Feb 1st, 1981*	*15*
46	1	May 8th, 1981	May 26th, 1981	19
47	--	*Jul 7th, 1983*	*Jul 19th, 1983*	*13*
48	--	*Sep 2nd, 1983*	*Sep 16th, 1983*	*15*
49	2	Oct 5th, 1984	Oct 21st, 1984	17
50	--	*Nov 14th, 1984*	*Nov 28th, 1984*	*15*
51	1	Mar 14th, 1985	Mar 31st, 1985	18
52	2	Sep 12th, 1985	Sep 23rd, 1985	12
53	--	*Jan 7th, 1986*	*Jan 18th, 1986*	*12*
54	1	Feb 23rd, 1986	Mar 6th, 1986	12
55	1	Feb 11th, 1987	Feb 22nd, 1987	12
56	--	*Mar 4th, 1986*	*Mar 20th, 1986*	*17*
57	1	Feb 21st, 1988	Mar 3rd, 1988	12
58	1	Mar 11th, 1988	Mar 24th, 1988	14
59	--	*Jun 6th, 1988*	*Jun 19th, 1988*	*14*
60	1	Nov 30th, 1988	Dec 13th, 1988	14
61	1	Apr 18th, 1989	Apr 29th, 1989	12
62	1	Dec 17th, 1989	Dec 29th, 1989	13
63	--	*Feb 26th, 1990*	*Mar 11th, 1990*	*14*
64	1	Jan 18th, 1991	Jan 30th, 1991	13
65	2	Oct 19th, 1991	Oct 30th, 1991	12
66	2	Jun 16th, 1995	Jul 1st, 1995	16
67	2	Aug 16th, 1995	Aug 31st, 1995	16
68	2	May 12th, 1998	May 24th, 1998	13
69	2	Oct 17th, 1998	Oct 28th, 1998	12
70	1	Oct 30th, 1998	Nov 10th, 1998	12
71	--	*Apr 14th, 2001*	*May 12th, 2001*	*29*
72	2	Nov 7th, 2001	Nov 19th, 2001	13
73	2	Aug 4th, 2002	Aug 16th, 2002	13
74	1	Jan 10th, 2003	Feb 2nd, 2003	23
75	1	Sep 7th, 2004	Sep 18th, 2004	12
76	2	Feb 8th, 2004	Feb 21st, 2004	14
77	2	Feb 23rd, 2004	Mar 5th, 2004	12
78	2	Apr 9th, 2005	Apr 20th, 2005	12
79	2	Sep 2nd, 2005	Sep 14th, 2005	13
80	1	Mar 16th, 2006	Apr 1st, 2006	17
81	1	Jan 20th, 2007	Feb 2nd, 2007	14
82	2	Apr 13th, 2008	Apr 28th, 2008	16
83	--	*Jan 30th, 2009*	*Feb 11th, 2009*	*13*
84	2	Mar 13th, 2009	Mar 26th, 2009	14
85	--	*Aug 31st, 2009*	*Sep 11th, 2009*	*12*
86	2	Nov 2nd, 2009	Nov 13th, 2009	12
87	1	Jan 5h, 2010	Jan 17th, 2010	13
88	1	Jan 27th, 2010	Feb 10th, 2010	15
89	--	*Feb 9th, 2011*	*Feb 24th, 2011*	*16*
90	2	Jan 29th, 2012	Feb 16th, 2012	19
91	2	Nov 15th, 2012	Nov 27th, 2012	13

92	2	Apr 25th, 2013	May 8th, 2013	14
93	--	*Sep 23rd, 2013*	*Oct 4th, 2013*	*12*
94	1	Oct 19th, 2013	Oct 31st, 2013	13
95	1	Jan 20th, 2014	Feb 3rd, 2014	15
96	1	Apr 24th, 2015	May 10th, 2015	17
97	--	*Aug 27th, 2015*	*Sep 8th, 2015*	*13*
98	1	May 16th, 2016	May 29th, 2016	14
99	1	Jan 26th, 2017	Feb 7th, 2017	13
100	--	*Sep 8th, 2017*	*Sep 19th, 2017*	*12*
101	2	Oct 11th, 2017	Oct 24th, 2017	14
102	1	Dec 4th, 2018	Dec 16th, 2018	13
103	--	*Sep 12th, 2020*	*Sep 29th, 2020*	*18*

Table 3.1 Start and end dates and duration (in days) of short-duration dry spell events. Events in italicized font are of mixed type, and are excluded from the subsequent analysis in this report

Two potential issues with the above approach are: 1) the atmospheric conditions that reinforce the individual dry spell events do not "lock in place" at onset, but may continue to evolve over time, and 2) our 103 events have different total lengths, ranging from 12 to 29 days. To rectify these issues, we utilize a twelve-day averaging approach, whereby we time-average the first twelve total days for each event to generate a composite for that individual event. Therefore, we reconstitute our 103 individual dry spell events as the time-average of the first twelve days (hereafter, the onset period) of each respective event. This approach addresses the first issue, since the time-average is a filter isolating lower frequency parts of the fields. Regarding the second issue, by using the same time-averaging for each respective event, we can now reliably compare the large-scale meteorology associated with the 103 different events.

3.3b – k-Means Clustering

Clustering analysis can group similar patterns among the 103 events, thereby providing a quantitative tool to isolate distinct atmospheric LSMPs associated with the dry spells. In this study, the *k*-means clustering approach is applied to the 500 hPa stream function (SF) anomaly fields defined for the 103 dry spell events in the domain 30-50°N / 60-90°W (Fig. 3.1). This approach is iterative, and moves events from one group to another until there is no added improvement in

reducing the overall distance between patterns among events in the created groups (Lee and Grotjahn 2016). The distance can be defined as the squared Euclidean point-to-centroid distance in each cluster, where each centroid is the mean of the patterns in its cluster (Spath 1985; Seber 2009). In every iteration step, the clustering process creates clusters objectively. For our analysis, we choose to apply clustering to anomalous 500 hPa SF rather than Z500 because SF produces a discernible pattern in the tropics as well as higher latitudes. Additionally, the 500 hPa level is chosen because it is a commonly-used level for showing large-scale, upper-level patterns in the midlatitudes.

Two potential concerns arise when applying *k*-means clustering to atmospheric data: 1) there is some uncertainty in choosing an optimal number of clusters, and 2) assigning an event to one cluster over another is less clear when sample size is small. To address these concerns, first we applied a technique analogous to the "distance of dissimilarity" metric [as in Stefanon et al. (2012)] to determine the optimal number *k*. The number *k* with a sudden drop of intercluster distance for the next higher value of $k + 1$ is considered the optimal number of clusters. Intercluster distance of our SF anomaly field has a notably abrupt drop from $k = 2$ to higher *k*. While a larger number of *k* may lead to less uncertainty in the classification process, the goal of the clustering analysis is to gain physical insight into the conditions surrounding the events without creating a distinct group for each event (Lee and Grotjahn 2016).

The distance of dissimilarity metric, as well as our visual inspection of individual events, led us to choose k=2 clusters in this study. Additionally, spatial projection analysis is applied (as in Lee and Grotjahn 2016) to assess how well individual events are sorted into the two clusters. Projection coefficients p_{kj} of the *j*th event against the *k*th cluster composite means are calculated for the same domain of the 500 hPa stream function anomaly above:

$$p_{kj} = \frac{\sum_{i=1}^{N}(x_i^j y_i^k)}{\sum_{i=1}^{N}(y_i^k)^2}, \quad \text{for } k = 1,2 \text{ and } j = 1,\ldots,n,$$

where k is a cluster, j identifies an individual event, n is the total number of events (n=103), i is a specific grid point, N is the total number of grid points, x is the field of a variable of individual events j to be projected, and y^k is the composite mean field of x for cluster k.

The projection coefficients are plotted on a scatterplot in Fig. 3.3. In the scatterplot, individual events generally fall into groups along a diagonal line between two groups where the projection on one cluster mean is much higher than the projection onto the other cluster mean. The two cluster means will be shown as two ways in which the synoptic pattern creates similar conditions *over our region of interest*. We want to identify as many events as we can that are assignable to one or the other cluster. In Fig. 3.3, we see that there are some events that project weakly and/or similarly onto both cluster means. These events, here labeled "mixed" (those depicted in-between the dashed lines), will not be considered in detail, and were determined as follows: Initially, the clustering algorithm was applied to all events as detailed above using k = 2. Then initial cluster composite means were calculated from the constituents of the respective clusters. Next, each event was projected onto both initial cluster composite means. Final cluster membership requires each event to fall outside of the two dashed lines in Fig. 3.3. Events falling between the dashed lines were declared mixed events, and excluded from the final sets of cluster constituents. The separation of events during the SF clustering process is also relatively insensitive to reasonable changes in the domain boundaries (of ±5°), and similar composite means are generated when a different clustering field is used (i.e., Z500 instead of SF; see Supplemental Materials of the online article).

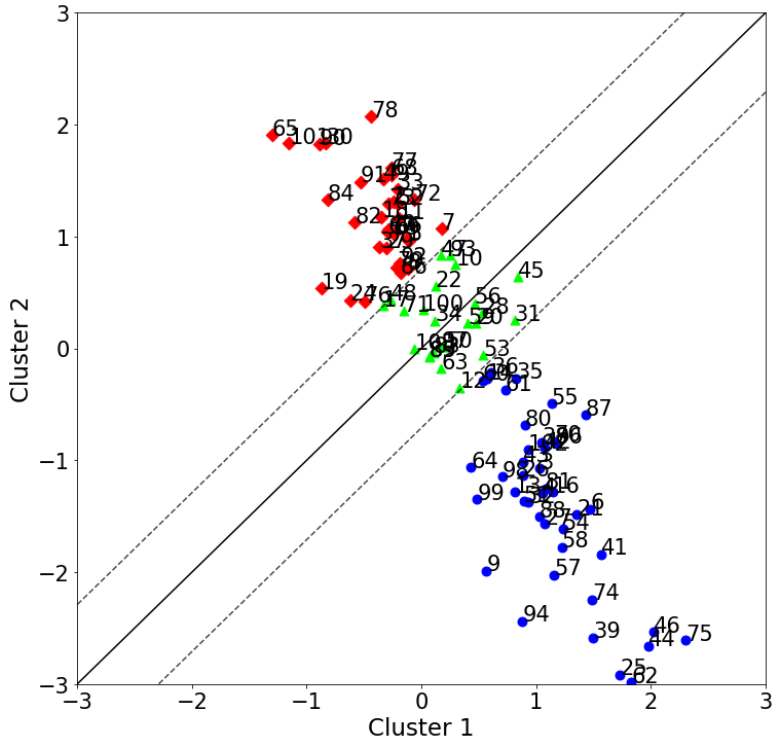

Fig. 3.3 Scatterplot of two projection coefficients for each of the 103 events. The numbers match the event numbers specified in Table 1. Blue disks mark events in Cluster 1, while red diamonds mark events in Cluster 2, and green triangles mark mixed events and fall within the dashed lines. Dashed lines are used as a visual aid to show the separation of Cluster 1 and Cluster 2 events from mixed events. Shift of the dashed lines from the 1:1 line is 0.70. For individual events, the anomalous 500 hPa stream function field is projected onto the composite means of the two clusters. Thirty-four mixed events are excluded from the analysis hereafter

Of the 103 events initially identified, 34 mixed events were excluded. Cluster 1 is left with 45 events, while Cluster 2 is left with 34 events. Within these clusters, events are further grouped by month to reveal seasonal differences. Monthly distributions are shown in Fig. 3.4. The winter (DJF) and spring (MAM) periods for Cluster 1, along with the fall (SON) period for Cluster 2, have the larger sample sizes of events. As such, we focus on these three combinations of cluster type and season in Section 3.4. The LSMPs for these combinations are shown in Fig. 3.5. Results for other seasons are shown in the Supplemental Materials of the online article.

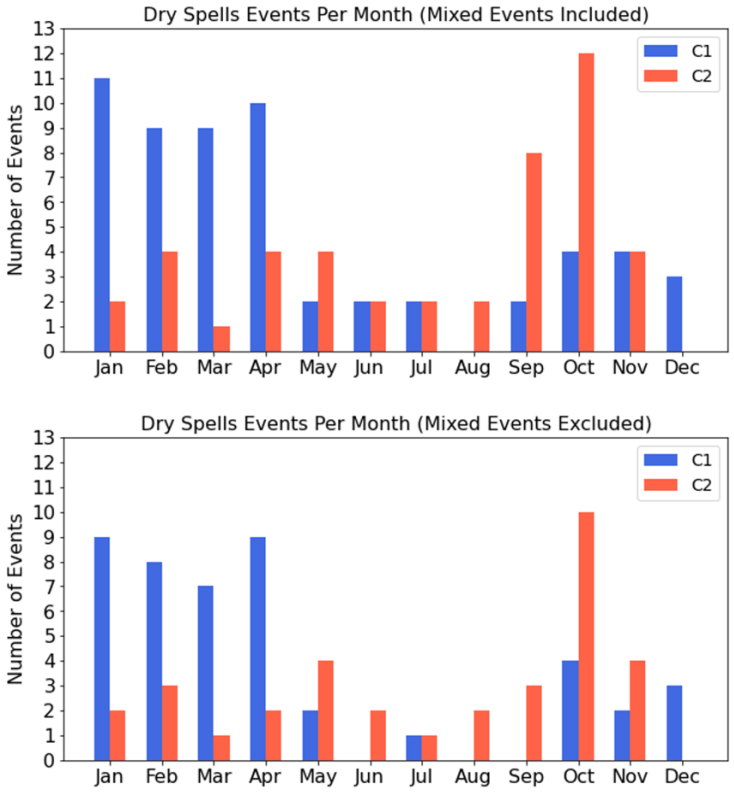

Fig. 3.4 Distribution of dry spell events by month (**top**, mixed events included; **bottom**, mixed events excluded). C1 denotes Cluster 1 and C2 denotes Cluster 2

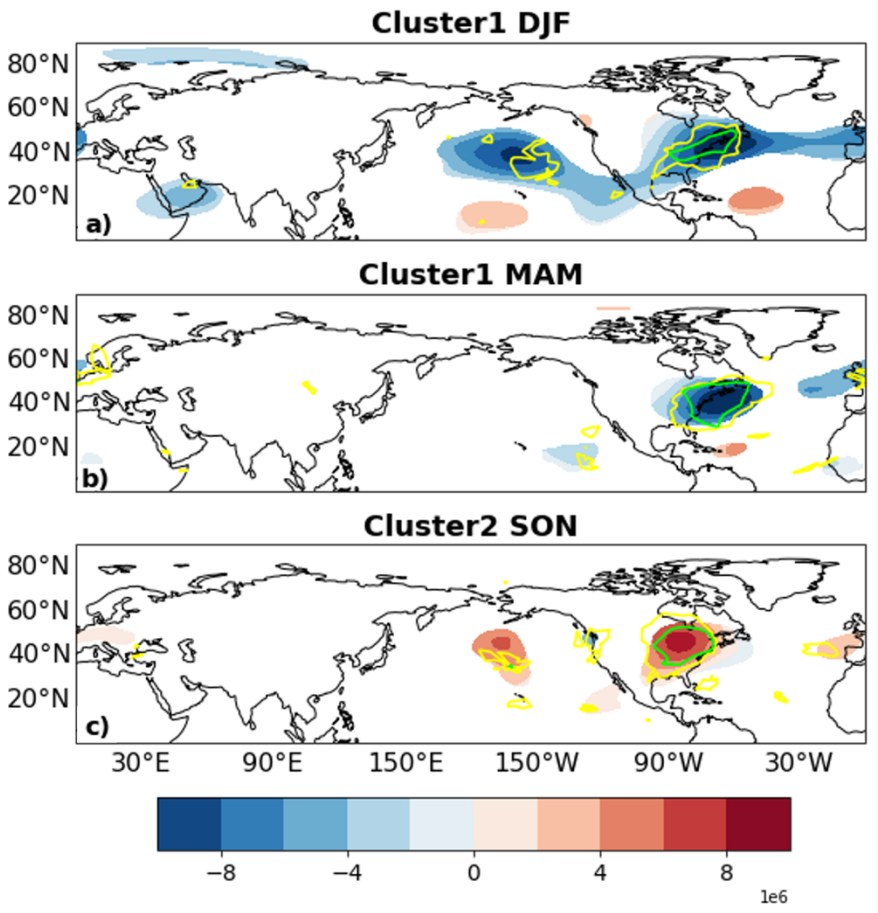

Fig. 3.5 Large-scale meteorological patterns (LSMPs), defined by the 500 hPa stream function anomaly field (m^2/s; contours), for the short-duration dry spell events in Cluster 1 in a) DJF (20 events) and b) MAM (18 events), and c) Cluster 2 in SON (17 events). Contour shading indicates areas of significance determined by bootstrap resampling. Yellow and green contours indicate: sign count magnitude of 0.6 and 0.8, such that 80% and 90% of the members in the cluster have the same sign, respectively. Stream function values are scaled by 10^6

3.3c – Wave Activity Flux

To track the propagation of wave energy, we use the wave activity flux (WAF), as formulated in Takaya and Nakamura (2001) (hereafter, TN01), to track the propagation of wave energy. This method allows one to analyze specific periods in time, like the wave activity flux developed by Plumb (1986). We use the quasi-stationary WAF formulation to track the time evolution of wave activity associated with the development of the dry spell events. TN01 show that this wave activity is locally parallel to the group velocity of quasi-geostrophic Rossby wave

packets. Convergence of WAF at a ridge in geopotential is expected to amplify the ridge, while the same ridge would decay if WAF was diverging there. Depending on where the convergence and divergence of WAF occurs relative to the geopotential pattern, these areas can be interpreted as driving both the propagation and amplitude changes of troughs and ridges. The TN01 WAF formulation has been used to study the dynamics of many phenomena, such as blocking formation over Siberia (Nakamura et al. 1997; TN01) and the formation of hot spells in the California Central Valley during the summertime (Lee and Grotjahn 2016). Here, WAF is used to interpret the respective trough and ridge formations in the LSMPs that are associated with short-duration dry spells in the Northeast. Our results focus on analyzing WAF in conjunction with the SF anomaly. Similar results are obtained using the WAF as defined in Plumb (1986) (see Supplemental Materials of the online article).

3.3d – Lead-Lag Composites

Another tool that is used to understand the time evolution of the dry spell events is to form composites of total and daily anomaly fields for atmospheric fields for the clusters at fixed times prior to and after the dry spells, for individual events. For the prior time period, we look at 3, 2, and 1 day(s), respectively, before the onset start date for each individual event. For each of these periods, the events are averaged to generate composites. The composites for these days represent our "lead" periods. An analogous procedure constructs the lag periods, in which the "lag" periods are 1, 2, and 3 day(s), respectively, after each *individual* dry spell events has ended.

The lead and lag periods for the events in Cluster 1 DJF, Cluster 1 MAM and Cluster 2 SON show differences between the clusters in the development of the corresponding LSMPs and related dynamics. The patterns and their evolution are consistent among the events within a cluster

subgrouping. The consistency is measured by using a sign counts procedure (Grotjahn 2011), which involves counting the number of events whose corresponding anomaly field has the same sign of the cluster mean anomaly at each grid point. Sign counts are calculated as follows: in a cluster, the number of events with a negative sign at a grid point is subtracted from the number of events having positive sign at that grid point; that difference is then divided by the total number of events in that cluster. This facilitates comparison among clusters that have a different number of events. For example, a sign count of 1.0 would indicate that all events in that cluster have positive anomaly at a particular grid point. A sign count of -1/3 means that 2/3 of the events have negative anomaly at that grid point. The sign counts procedure is combined with significance from a bootstrap test to identify true LSMPs (Reed et al. 2022). The bootstrap compares the cluster mean to a large number (order 1000) of random means formed from the same membership size and drawn with replacement. Regions where the cluster mean is $< 5\%$ or $\geq 95\%$ of the random means are labeled significant for the LSMP composites.

3.4 – Two Different Types of Dry Spell Events

3.4a – Evolution of Precipitation Anomalies

The evolution of the precipitation anomalies for the three combinations is considered first. While negative anomalies are located over the Northeast during the onset period for each season, there are some differences in their evolution. For Cluster 1 DJF, a negative precipitation anomaly develops in the lower Mississippi Valley region at two days before onset (Fig. 3.6b) and strengthens until onset (Fig. 3.6d). This strengthening coincides with the development of negative precipitation anomalies over the Atlantic coast and the Northeast. Similar development is observed with Cluster 1 MAM, with the gradual strengthening of the negative anomaly near the Gulf Coast

and Northeast (Fig. 3.6i – Fig. 3.6l). Cluster 2 SON does exhibit the same strong negative anomaly near the Gulf Coast; but the negative anomalies are more widespread across the central United States (Fig. 3.6s). The strongest negative anomalies first occur over the Northeast at the onset (Figs. 3.6d, l, t). The dry anomaly persists for the whole dry spell (Figs. 3.6e, m, u). In all three combinations, it is apparent that dry anomalies are present across large portions of the eastern United States in the period before and during the dry spells, and are not confined solely to the Northeast. This indicates that Northeast dry spells are typically part of a much larger region of reduced precipitation. Additionally, the expansive dry anomalies along the eastern United States, especially during winter, suggest changes to the trajectory of midlatitude weather systems. Our results will confirm this by finding a narrowing and shifting southward of the frontal cyclone storm track along the Atlantic seaboard during the dry spell events.

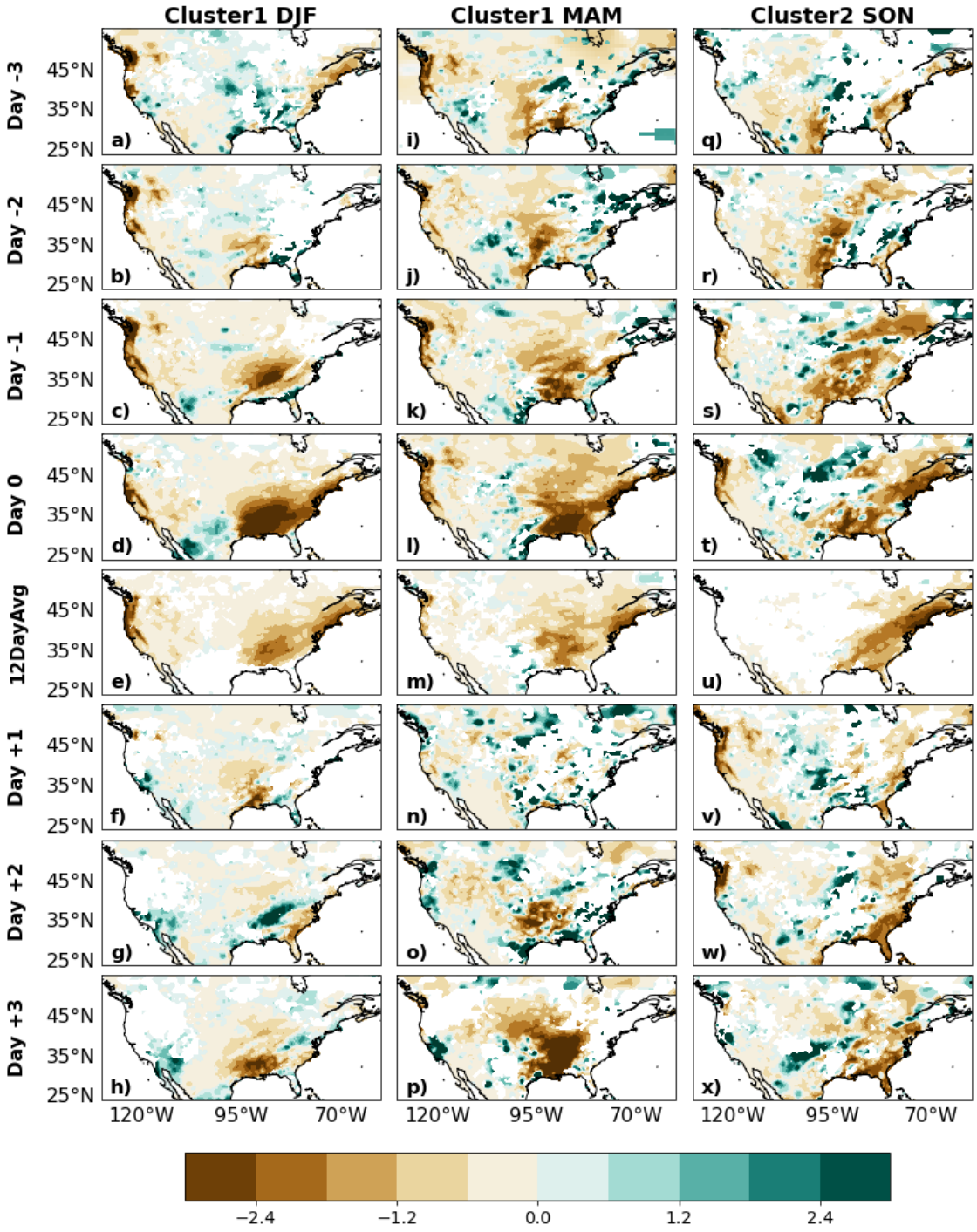

Fig. 3.6 Evolution of composites of total precipitation anomaly (mm/day; shading) for the cluster type and season indicated by the label at the top of each column. For the anomaly field, grid points are plotted only when the sign count has magnitude greater than 1/3 (thus 2/3 of the members have the same sign). Rows from top to bottom show the following periods, respectively: 3 days before onset, 2 days before onset, 1 day before onset, onset, 12-day dry spell period, 1 day after dry spells end, 2 days after dry spells end, and 3 three days after dry spells end

3.4b – Dynamical Differences Driving Two Types of Dry Spells: SF, WAFs, and Jet Stream

We now develop a dynamical picture of the differences in the evolution of the LSMPs of the three seasons as defined by the 500 hPa stream function (SF) anomaly and the associated WAF fields (Figs. 3.7 and 3.8). Corresponding jet stream field changes are shown in Figs. 3.9 and 3.10. Cluster 1 DJF (Fig. 3.7e) and MAM (Fig. 3.7m) during dry spells are defined by a strong negative pressure anomaly centered off the midlatitude Atlantic seaboard. Another negative center is found in the central Pacific (Fig. 3.5a, 3.7e) in Cluster 1 during DJF but not during MAM (Fig. 3.5b, 3.7m). Cluster 2 SON, in contrast, features a strong positive pressure anomaly center in east-central North America (Fig. 3.5c, 3.8e).

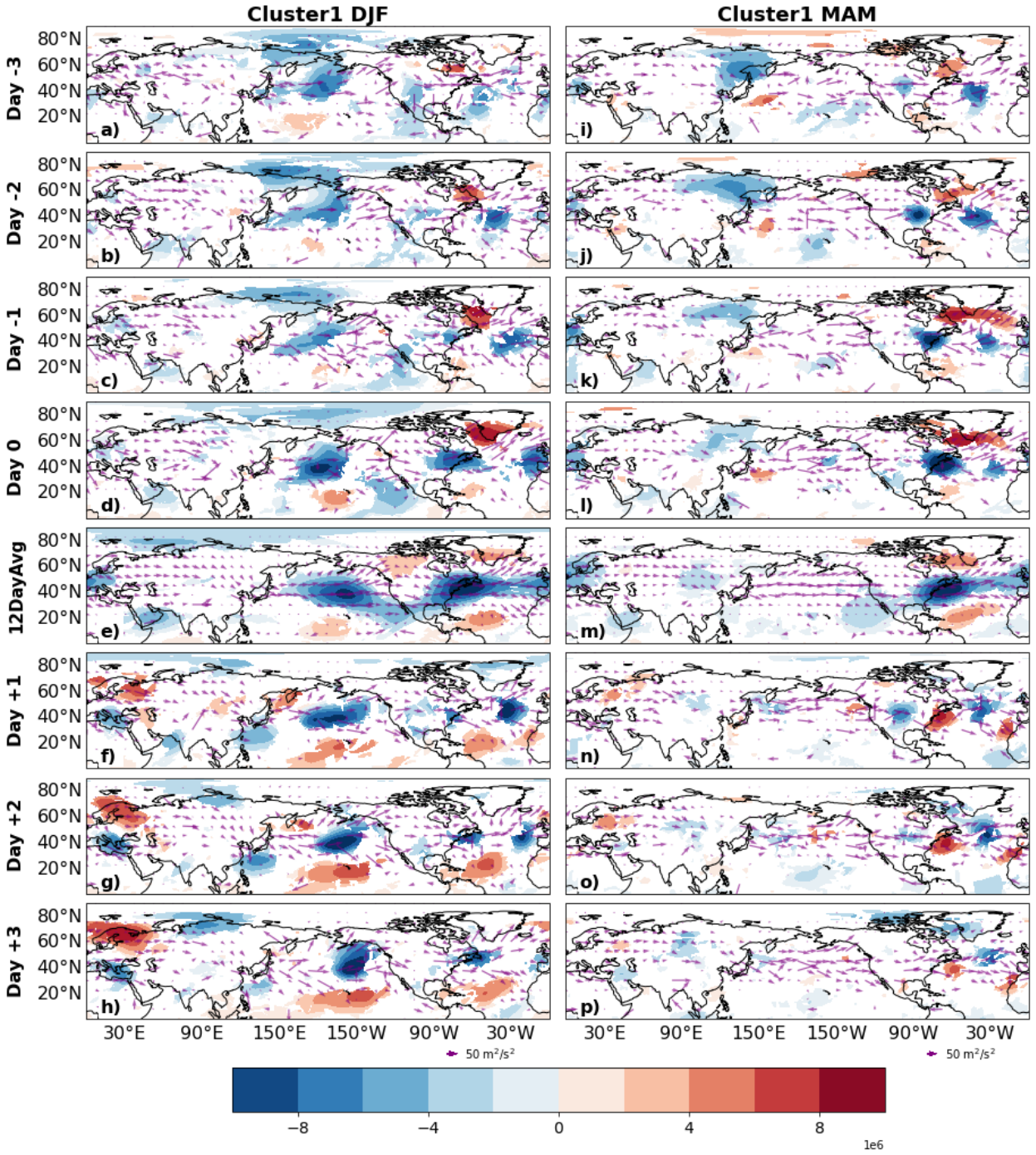

Fig. 3.7 Same format as **Fig. 3.6**, except showing evolution of composites of 500 hPa stream function anomaly (m^2/s; contours) and total horizontal WAF (m^2/s^2; vectors) for Cluster 1 during DJF and MAM. For the anomaly field, grid points are plotted only when the sign count has magnitude greater than 1/3. WAF is plotted only when either the zonal or meridional component has a sign count whose magnitude exceeds 1/3. Stream function is scaled by 10^6

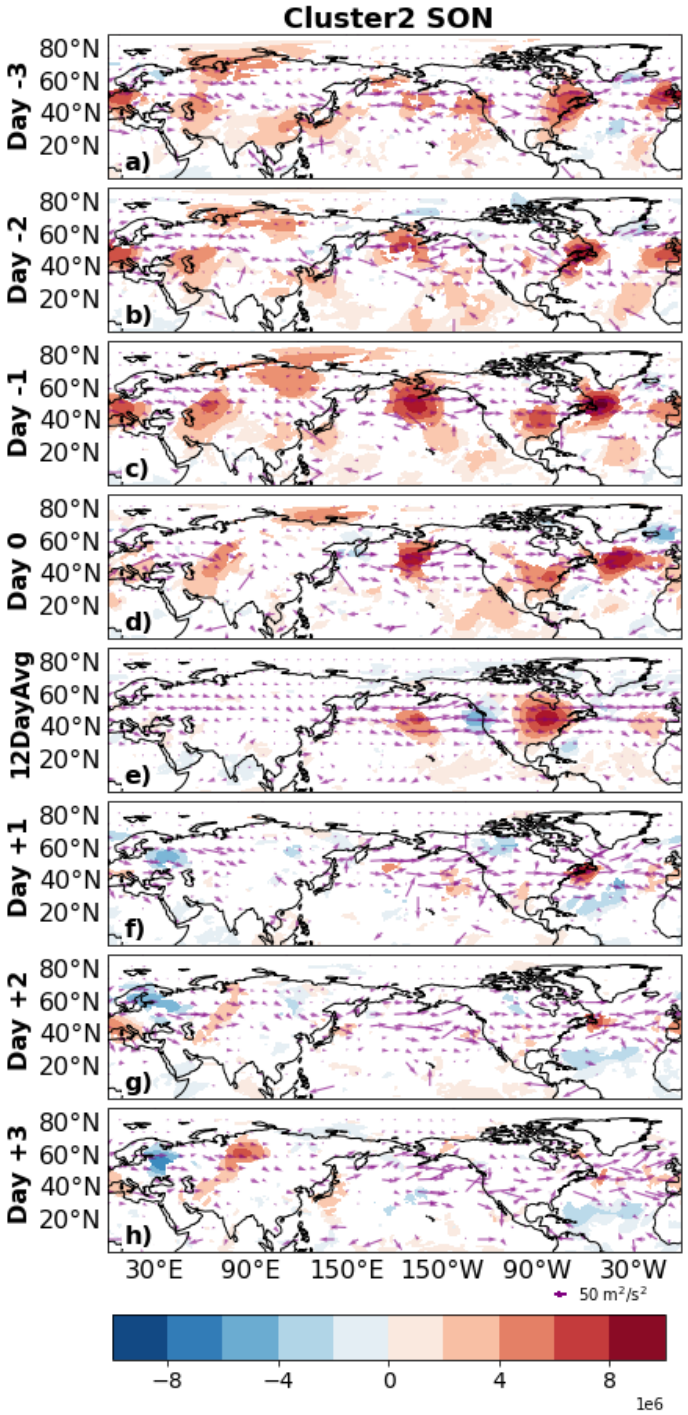

Fig. 3.8 Same format as **Fig. 3.7**, except showing Cluster 2 during SON

The evolutions toward these SF fields differ between the dry spell combinations. For Cluster 1 DJF, a negative low-pressure anomaly is located in the northern Pacific and in the western

United States at three days before onset (Fig. 3.7a). The central Pacific anomaly slowly develops and expands, while the continental anomaly moves eastward (Fig. 3.7b-c) and expands at the onset date (Fig. 3.7d), with both anomalies reaching peak magnitude during the onset period (Fig. 3.7e). The development of the Cluster 1 MAM (Fig. 3.7i-k) is similar to that of DJF, as a negative anomaly develops in the central US and moves eastward and expands by the onset date (Fig. 3.7l), with the notable absence of the negative SF anomaly in the central Pacific. Cluster 2 SON features a strong positive pressure anomaly center in east-central North America (Fig. 3.8e). For Cluster 2 SON, a high-pressure anomaly is centered near Maine at three days before onset (Fig. 3.8a) that begins to move offshore a day later (Fig. 3.8b). At the same time, a small area of high-pressure develops in the central US. This area strengthens and expands (Fig. 3.8c) and moves eastward by the onset date (Fig. 3.8d), with the high-pressure area reaching peak magnitude during the onset period (Fig. 3.8e).

After the dry spells: the low-pressure anomaly in the midlatitude Atlantic Ocean for Cluster 1 DJF (Fig. 3.7f-h) and MAM (Fig. 3.7n-p) weakens and moves farther eastward away from the shore. The low-pressure in the central Pacific in Cluster 1 DJF is still present, but is less expansive in its eastward extent (Fig. 3.7f-h). Similarly, the high-pressure area in Cluster 2 SON also weakens and shifts eastward (Fig. 3.8f-h).

Fig. 3.7 and Fig. 3.8 also show cluster mean WAF vectors for evolution of the dry spells. The WAFs differ between the three combinations in ways partly consistent with the above discussion. In Cluster 1 DJF, WAF vectors cross north-central North America with convergence in the midlatitude Atlantic Ocean, just offshore of North America, a location consistent with the build-up of the trough during the day -1 lead plot (Fig. 3.7c). During the onset period (Fig. 3.7e), WAF converges into the trough, helping to strengthen and maintain it. Elements of the pattern can

travel differently and thus be out of phase (and WAF convergence appears weak) before coming into phase at onset and the onset period. In general, WAF for Cluster 1 DJF during the onset period indicates convergence in the midlatitude Atlantic Ocean. By the lag periods (Fig. 3.7f-h), WAF convergence is weaker near the Northeast, coinciding with the weakening of the trough and its shift eastward. This development is similar for Cluster 1 MAM (Fig. 3.7i-p). In Cluster 2 SON, the WAF vectors are often weaker than those in Cluster 1, and convergence of WAF is less clear in east-central North America as the high-pressure ridge builds up (Fig. 3.8a-d) and reaches peak strength during the onset period (Fig. 3.8e). Hence, WAF convergence is less useful in explaining the build-up of the high-pressure ridge in Cluster 2 SON.

Given the different mid-tropospheric 500 hPa SF LSMPs, one would expect some differences in the midlatitude jet stream as well. Fig. 3.9 and Fig. 3.10 show total zonal wind (contours) and zonal wind anomaly (shading) at 200 hPa, for the three combinations. In Cluster 1 DJF and MAM (Fig. 3.9), the wind anomaly pattern suggests a narrowing of the jet stream. The northern dipole pair of wind anomalies in the midlatitude Atlantic strengthens and expands the midlatitude jet eastward into the central Atlantic Ocean (Fig. 3.9d,l) while weakening it over eastern Canada. The total zonal component peaks during the onset period (Fig. 3.9e,m). As a consequence, the jet stream peak value increases from lead to onset at 25-45°N from the North American east coast out over the Atlantic, and a clear region of deceleration sets up from Hudson's Bay eastward out over the Atlantic. From balancing terms: zonal advection and ageostrophic Coriolis in the zonal momentum equation, this jet stream deceleration region would have northerly ageostrophic motion. Allowing ageostrophic winds to approximate divergent winds, an upper-level pattern of northerlies over the Great Lakes together with southerly ageostrophic wind to the south (Fig. 3.11a,b), is consistent with subsidence over the Northeast. Hence, ageostrophic northerlies in

the deceleration region coupled with ageostrophic southerlies in the acceleration region (Fig. 3.11a,b) act to generate upper-level convergence (Fig. 3.11d,e) and sinking beneath (Fig. 3.11g,h). This sinking might also be understood from the vorticity equation, where the divergence term and planetary vorticity advection terms may approximately balance (Grotjahn and Osman 2007), such that upper-level northerlies imply convergence. However, further east, where the northerly ageostrophic winds are northerly (Fig. 3.11a,b), the zonal wind anomaly is still positive, though weakened downstream over the Atlantic (Fig. 3.9e,m).

For Cluster 2 SON (Fig. 3.10), a different jet stream anomaly pattern is also observed, though the consequence is similar to that of Cluster 1. A negative anomaly centered over the southeastern US quadrant, coupled with a positive anomaly over Hudson's Bay (Fig. 3.11c), creates acceleration over the east coast of the United States. To the north, a positive anomaly peaks near Hudson's Bay, so the winds decelerate over eastern Canada. These anomalies strengthen the total zonal component whose value peaks at 2-day lead (Fig. 3.10b) such that the total wind jet axis is north of the region of interest during the onset period (Fig. 3.10e). The jet deceleration would imply northerly ageostrophic motion, visible in Fig. 3.11c. Over northeastern North America, ageostrophic winds turn anticyclonically, creating upper-level convergence (Fig. 3.11f) and sinking over the Northeast (Fig. 3.11i).

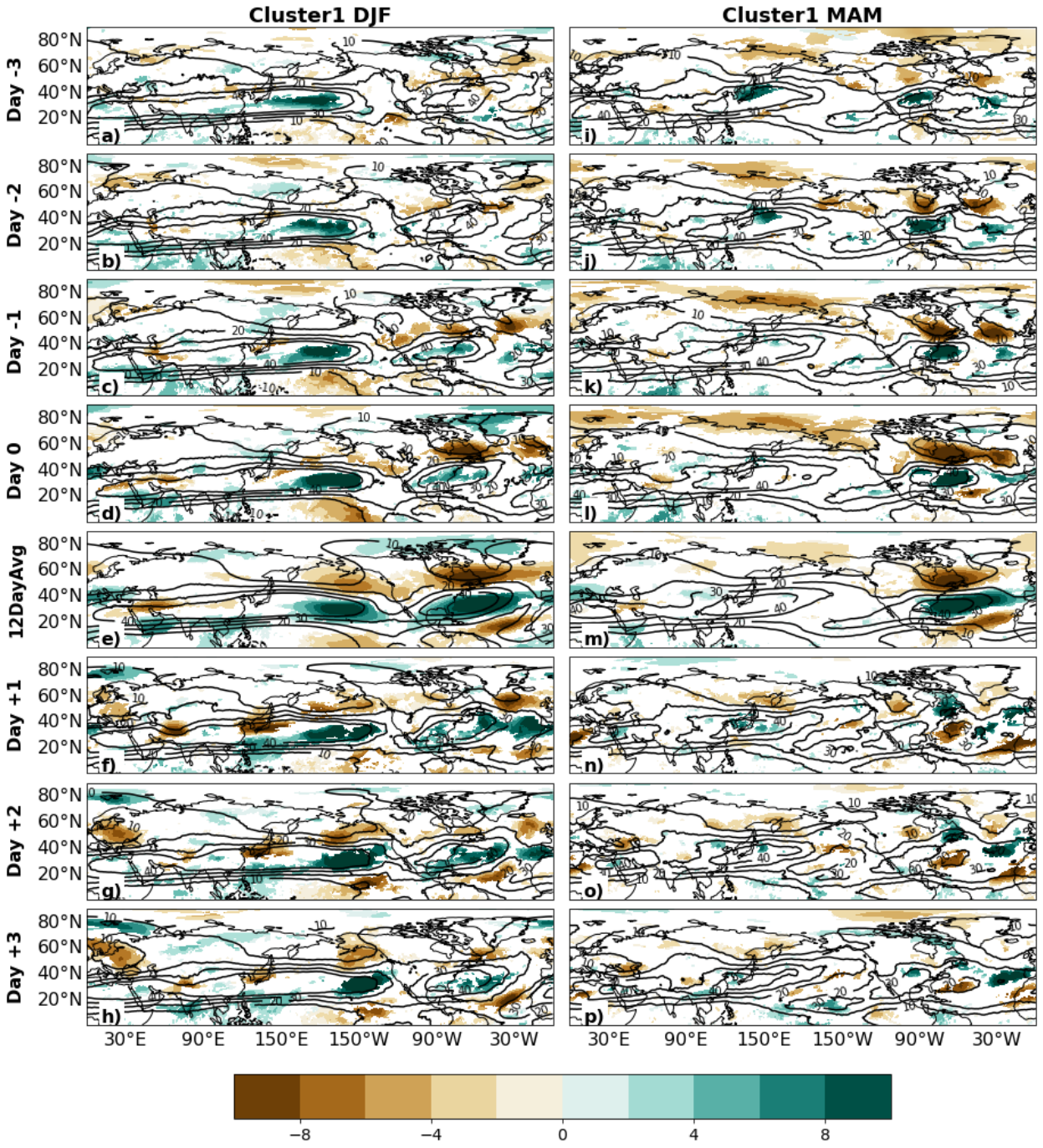

Fig. 3.9 Similar format as **Fig. 3.7**, except showing evolution of composites of total zonal wind speed (lined contours) and anomalous zonal winds (shading) at 200 hPa for Cluster 1 during DJF and MAM. For the anomaly field, grid points are plotted only when the sign count has magnitude greater than 1/3. Contour interval is 2 m/s for the anomaly field. Only total field contours from 10-40 m/s are plotted, with a 10 m/s contour interval

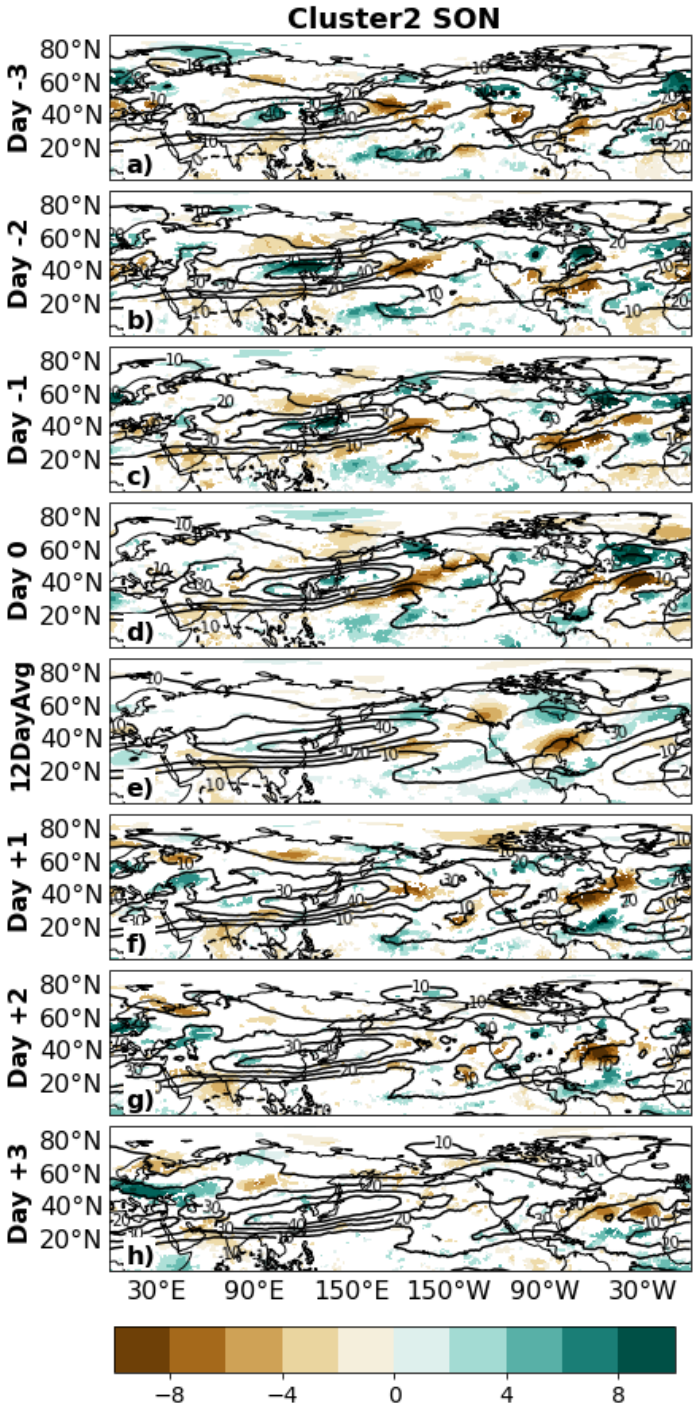

Fig. 3.10 Same format as **Fig. 3.9**, except showing Cluster 2 during SON

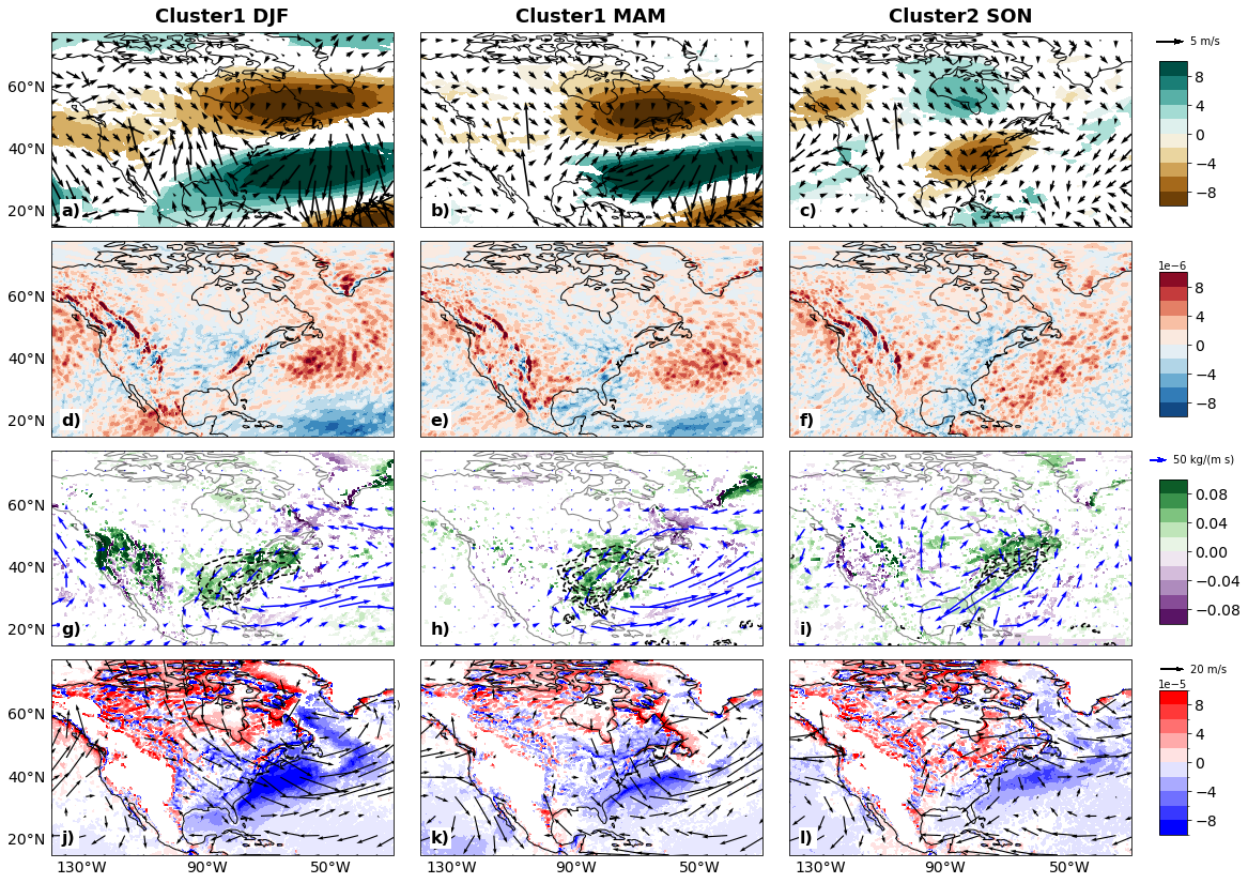

Fig. 3.11 Several meteorological fields during the 12-day dry spell period. **Top row:** Anomalous zonal winds at 200 hPa (m/s; shading) and total ageostrophic winds at 200 hPa (m/s; vectors). For the anomaly field, grid points are plotted only when the sign count has magnitude greater than 1/3. Vectors are plotted only when either the zonal or meridional component has a sign count whose magnitude exceeds 1/3. **Second row:** Total horizontal divergence at 200 hPa (s^{-1}; shading). **Third row:** Anomalous omega at 700 hPa (ω700) (Pa/s; shading), anomalous specific humidity at 850 hPa (Q850) (g/kg; contours), and anomalous integrated vapor transport (IVT) (kg/(m s); vectors). For all three fields, only grid points with sign count magnitude over 1/3 are plotted. Vectors are plotted at grid points where either the zonal or meridional component passes the 1/3 sign counts criterion. Lined contour interval is 0.20 g/kg, and minimum contour magnitude is 0.55 g/kg. For clarity, only negative Q850 dashed contours are shown. **Bottom row:** Total 925 hPa temperature advection (TA925) (K/s; shading) and total winds at 925 hPa (m/s; vectors). For contours, only grid points with sign count magnitude over 1/3 are plotted. Vectors are plotted at grid points where either the zonal or meridional component passes the 1/3 sign counts criterion

The discussion thus far of the dynamics associated with the dry spell combinations may be summarized as follows. In Cluster 1, WAF accompanies the development of a low-pressure area in the midlatitude Atlantic Ocean. Changes to the zonal flow link to ageostrophic motions that foster upper-level convergence and sinking over the Northeast. A high-pressure area in east-central

North America is built up in Cluster 2 SON, with less influence from WAF convergence. While the zonal flow changes also differ from Cluster 1, the ageostrophic motions again lead to upper-level convergence and sinking over the Northeast. Next, the thermal and moisture changes critical to the creation of the dry spells are discussed.

3.4c – Thermodynamical Differences Driving Two Types of Dry Spells

We now discuss anomalous 700 hPa omega (ω700), integrated vapor transport (IVT), 850 hPa specific humidity (Q850), and total 925 hPa temperature advection (TA925), during the onset period of the dry spells, to further the analysis in Section 3.4b. We narrow our discussion to the conterminous United States to focus on local conditions during dry spells.

Upper-level convergence and divergence anticipated from our discussion of the zonal jet stream (U200) anomalies are consistent with ω700 anomalies shown in Fig. 3.11. In each combination, there are strong, positive ω700 anomalies over the Northeast during the onset period (Fig. 3.11g-i). Subsidence brings down air having low moisture content over the northeastern United States. Sinking also suppresses cloud formation and precipitation, thereby partly explaining the dry spells.

The horizontal moisture transport (Fig. 3.11g-i) suggests strong flow off the continent off over our northeastern region in each combination. The IVT vectors circulate in a manner consistent with the SF anomalies shown. Over the Northeast: Cluster 1 IVT northerly component occurs on the west side of an anomalous oceanic low, while similar Cluster 2 IVT is on the east side of the anomalous continental high. This anomalous flow of moisture into the Northeast likely reduces moisture and also partly explains the dry spells. During the onset period, the counterclockwise (CCW) IVT in Cluster 1 is generally strengthened when flowing offshore, but northerly flow into

the Northeast is much weaker (Fig. 3.11g-h). In Cluster 2 SON, the clockwise (CW) IVT is strengthened coming up from the Gulf of Mexico, and stronger northerly flow is observed into the Northeast (Fig. 3.11i) than is observed in Cluster 1. Given the importance of southerly IVT along the Atlantic seaboard for providing moisture to this region (Sukhdeo et al. 2022), these results provide additional context for the Q850 anomalies discussed below. As the mid-level stream function LSMPs develop, they act to divert the normal IVT away from the Northeast, leading to negative Q850 anomalies there during the onset period. For Cluster 1, the IVT anomaly is northeasterly and generally weak as it enters the Northeast during the onset period. In contrast, there is a wrap-around IVT associated with the Cluster 2 SON, as the strong high-pressure in east-central North America brings moisture-rich air northward into central North America.

The IVT vectors in Cluster 1 and Cluster 2 are generally similar *locally* over the northeastern region. While they differ away from the region, they are each strong in a different location. One can see how *mixed events can occur when the oceanic low and continental high are both present to suppress clouds and reduce moisture transport.*

Regarding Q850, negative anomalies are located near and over the Northeast during the onset period in the three seasons, with some differences between them. In Cluster 1 DJF and MAM, negative Q850 anomalies are centered parallel to the eastern US coast, extending from Louisiana to Maine (Fig. 3.11g,h). As the mid-level stream function LSMPs develop, they act to divert the normal IVT away from the Northeast, leading to negative Q850 anomalies there during the onset period. In Cluster 2 SON, the negative anomalies do not extend as far south and west as in Cluster 1, but instead are concentrated over the northeastern United States (Fig. 3.11i). Strong, positive $\omega 700$ anomalies tend to be collocated with these strong, negative Q850 anomalies.

Lastly, the role of temperature advection is considered, with Fig. 3.11j-l. showing TA925 for the three combinations. During the onset period for Cluster 1 DJF, there is strong cold advection just south of the Northeast in the midlatitude Atlantic Ocean (Fig. 3.11j). Cluster 1 MAM has cold advection in the same area, but the magnitude of the advection is much weaker than in DJF (Fig. 3.11k). The low-level oceanic low off Labrador creates anomalous cold advection to support the anomalous upper-level low to the southwest. For Cluster 2 SON (Fig. 3.11l), there is some cold advection south of the Northeast, and some warm advection just west of the region. The latter supports the anomalous upper-level continental high and is likely due to the CW rotation of the low-level high pressure centered over the southeastern United States. Cold air advection over the Northeast would reinforce the observed subsidence during the onset period, although the cold air advection appears to be much weaker for Cluster 2 SON.

3.4d – Changes in ETC Activity and Storm Track Density During Dry Spells

Extratropical cyclones (ETCs) and their tracks play a key role in the seasonal cycle of precipitation in the Northeast (Kunkel et al. 2012; Pfahl and Wernli 2012; Agel et al. 2015; Sukhdeo et al. 2022). There are generally two broad regions with the highest storm track densities: one over the Great Lakes region and another along the Atlantic seaboard (Hoskins and Hodges 2002; Kocin and Uccellini 2004; Pfahl and Wernli 2012; Agel et al. 2015). Track density is typically highest during the winter and spring, and is often weaker and shifted more northward into southern Canada during the summer and fall. As we have shown, the short-duration dry spells are in part associated with a suppression of normal onshore IVT, and given the climatological importance of ETCs for precipitation in the Northeast, it warrants discussing how the dry spell LSMPs relate to ETC storms tracks. We investigate this by identifying ETC tracks for the time

steps in 6-hourly data when ETCs are present in a specific geographic domain relevant to the Northeast. For tracking ETCs, we use the TempestExtremes software package (Ullrich and Zarzycki 2017), which allows for the tracking of pointwise elements within climate datasets. Six-hourly data for surface pressure (PS) and geopotential at 300 hPa and 500 hPa (Z300 and Z500, respectively) are taken from the ERA5 dataset for the period 1961-2021 and input to TempestExtremes, which then outputs the relevant ETC tracking information, such as time, latitude, and longitude of cyclone centers, and local sea-level pressure. Output from TempestExtremes is then selected for geographic relevance to the Northeast (25-55°N / 20-100°W). From the selected data, we can identify individual ETCs and their associated storm tracks before, during, and after each respective event. Because we are studying events that range in duration from 12-29 days, care must be taken when choosing the "after" period for looking at ETC tracks, as longer duration events persist after the 12-day onset period. Since tracks vary seasonally, we identify individual ETCs and their associated storm tracks before, during, and after each respective event. Thus, we define the "before," "during," and "after" periods as follows, using Event 2 (October 16th – 29th, 1961) as an example. The "during" period refers to the first twelve days of a particular dry spell event (in this case, October 16th – 27th, 1961). For the "before" period, we use a 12-day lead period (in this case, October 4th – 15th, 1961). Similarly, for the "after" period, we look at the first twelve days after the end of a particular dry spell event (in this case, October 30th – November 10th, 1961).

The track analyses are shown in Fig. 3.12. During the dry spell events, ETCs do not pass over the Northeast. This indicates that the dry spells are related to the absence of ETC activity in the region. Additionally, during the dry spells, the ETC storm track is shifted farther south of our region of interest for Cluster 1 during DJF and MAM (Fig. 3.12a-f). During DJF, the southern

ETCs are concentrated into a narrower track than other DJF times shown. This concentration supports the anomalous low there in Fig. 3.5a. This shift is less apparent for Cluster 2 SON (Fig. 3.12g-i). There are also some other key differences before and after the dry spell events. For Cluster 1 during DJF and MAM, before and after the dry spells, some of the ETCs moving through the Great Lakes region move southeasterly, and some of the ETCs pass through or nearer to the Northeast. Additionally, the ETC storm track is less concentrated off the Atlantic coast and is more evenly distributed in latitude. For Cluster 2 in SON, ETCs are in closer proximity to the Northeast in the before and after periods than they are during the dry spells. These differences between the ETC storm tracks during the dry spell events versus before and after the dry spells highlight the role that the dry spell LSMPs have in shifting the storm tracks. These results agree in part with those of Namias (1966), who found that the wintertime circulation near the Northeast during the 1960s drought diverted ETCs away from the region. Overall, our results indicate that the dry spell LSMPs are consistent with ETC storm tracks being diverted away from the Northeast, with a preference for diversion south of the Northeast during the winter and spring of Cluster 1. Sukhdeo et al. (2022) showed that increased ETC density in a similar tracking domain enhances mean precipitation in the Northeast. Here, our results indicate that dry spells occur in part when ETCs do not cross over the region.

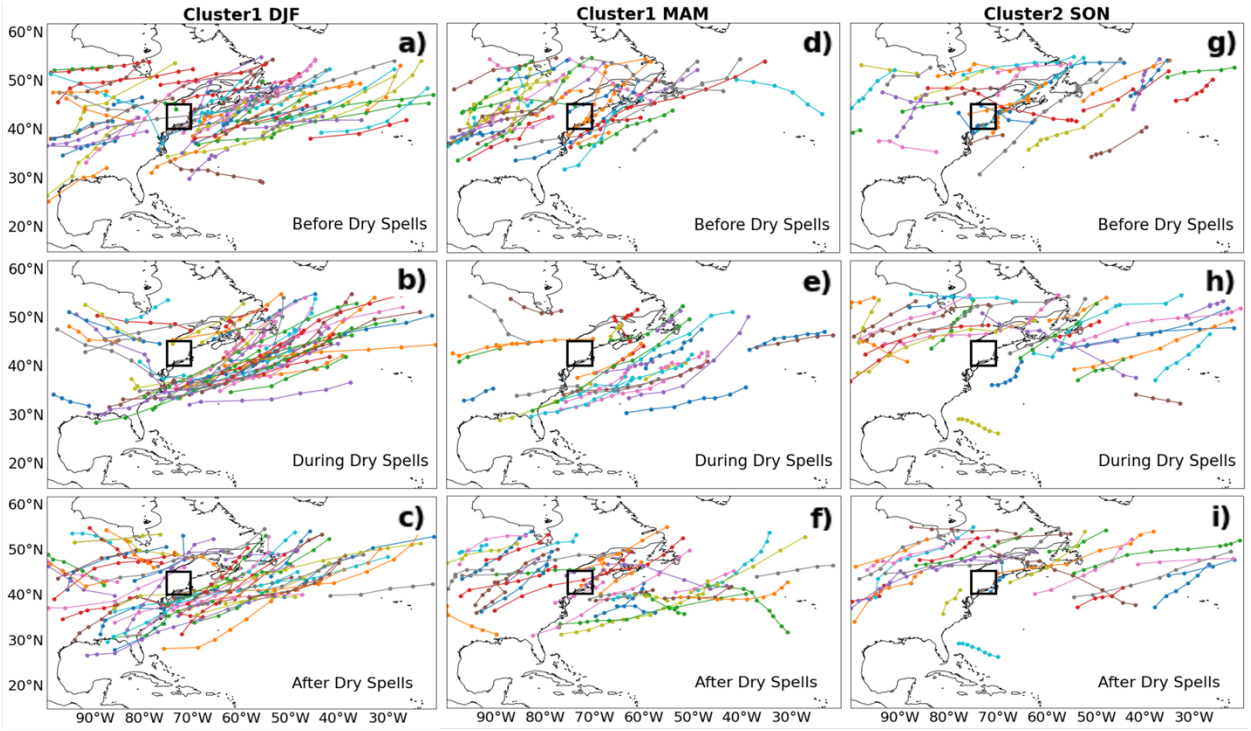

Fig. 3.12 Extratropical cyclone (ETC) storm tracks for 12-day periods before, during, and after the dry spell events. Each line represents an individual ETC storm track. Dots along each ETC storm track represent the location of the cyclone center at 6-hour increments during the ETC lifespan. The black box in each panel is the Northeast region as defined for this study

3.4e – Seasonality in Short-Duration Dry Spell Occurrence

The monthly distribution of short-duration dry spell events shown in Fig. 3.4 show seasonal variation in the occurrence of dry spells, with most of the events occurring during the winter, spring, and fall periods. Here, we speculate on why fewer dry spell events meet our criteria during summer as compared to the other seasons.

Fig. 3.13a shows the monthly-averaged time series of large-scale vs. convective precipitation from ERA5. Large-scale precipitation is greater than convective precipitation for most of the seasonal cycle, except during the summer. This change in precipitation type is primarily related to A) a reduction in extratropical cyclone (ETC) activity in the warm season (see Section 4D and Supplemental Materials), and B) an increase in sporadic, localized convection in and

around the Northeast (Agel et al. 2015). The decrease in ETC activity can partly be explained by reduced baroclinicity over the warm continent during summer (Gertler and O'Gorman 2019), and by increased localized convection attributed to a warm and moist environment in the Northeast that facilitates greater atmospheric convective instability during the late afternoon and early evening (Hurlbut and Cohen 2014).

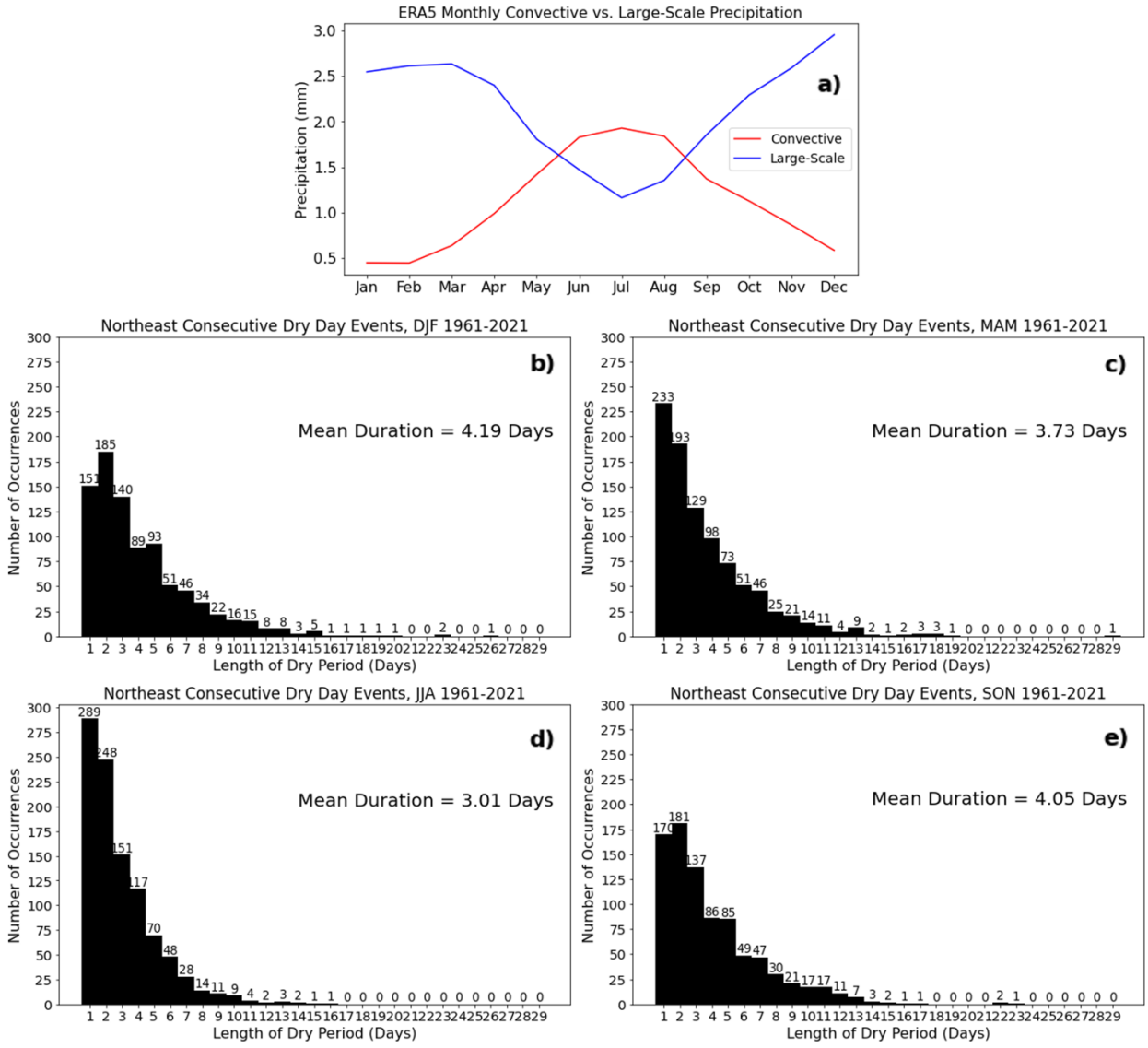

Fig. 3.13 Time series plot of area-averaged, monthly large-scale vs. convective precipitation over the Northeast from ERA5 (1961-2021) **(top)**; and CDD histograms for winter (DJF), spring (MAM), summer (JJA), and fall (SON) from 1961-2021 **(bottom)**. Histograms use the same format as in **Fig. 3.2**. Mean duration in each panel is the average CDD event duration for each season, respectively. The total number

of dry spells lasting 12 days or longer (all CDD events of any duration) in each season, including mixed type are: DJF 29 (874), MAM 30 (920), JJA 10 (1009), and SON 34 (863)

The summer period is also unique in terms of its distribution of CDD durations. Fig. 3.13b-e shows CDD histograms for each of the four seasons separately. The winter (DJF), spring (MAM), and fall (SON) periods have mean CDD durations of 4.19, 3.73, and 4.05 days, respectively. For the summer period, the mean CDD duration is nearly a day shorter (3.01 days). The summer period also has a much larger percentage (and number) of events lasting only 1 or 2 days as compared to the other seasons. Summer has ~10% or more CDD periods than the other seasons, but many fewer CDDs last 12 days or longer.

These results are consistent with the changes in precipitation type in the seasonal cycle. During the winter, spring, and fall, as ETC activity is one of the primary drivers of precipitation (Agel et al. 2015; Sukhdeo et al. 2022), precipitation is concentrated along the ETC "storm track." As the storm track changes position due to a block, then the time elapsed between consecutive ETCs affecting our region is lengthened. In contrast, summer precipitation is less guided by large-scale features, and coupled with enhance instability, convection occurs more frequently and sporadically, so CDD periods are shorter in duration.

3.4f – How do Short-Duration Dry Spells Compare with Drought Months?

The top roughly 10% of CDD periods are 12 days or longer, a shorter timescale than would be used *if* this was a drought study. Because of this, there can be dry spells that meet our event duration criterion during a month with near-normal (or even above normal) precipitation, depending on what happens during the other days of that month. Hence, some of our CDD events can occur in months that are not "drought" months. Additionally, care must be taken when defining a drought, as the occurrence of a dry spell in a particular month can inaccurately attribute drought

conditions to a non-drought month. The question is then what fraction of dry events occurs in drought versus non-drought months?

To understand better the connection between short-duration dry spells and drought months, it is necessary to identify longer-term periods of drought that have specifically impacted the Northeast. Gridded, 3-month Standardized Precipitation Index (SPI) values (formulated based on Guttman 1999) over the Northeast from 1961-2021 are employed to identify drought (SPI ≤ -1) months. The 3-month SPI seems more appropriate than a 1-month SPI here, as it provides a more accurate assessment of short- to medium-term moisture conditions. After identifying these months, we then cross-reference the dates of the short-duration dry spells with these drought months to determine the number of our dry spell events that occur in these months (Readers can find tables listing specific drought months and the dry spell events in those months in the Supplemental Materials of the online article). During 1961-2021, ~15% (111/732) of the months are so-identified as drought months, while ~27% (28/103) of our dry spells occur during those months, using the 3-month SPI. Alternatively, ~18% (131/732) of the months are so-identified as drought months, and ~44% (45/103) of our dry spells occur during those months, using the 1-month SPI. Since the ratios differ, a 1-month SPI seems inappropriate for assessing a connection between short-duration dry spells and "drought" months, as the occurrence of a dry spell (12 days or longer) in a month can lead to a biased correlation with a low 1-month SPI value for that month. With the stricter drought criteria of the 3-month SPI, only about a quarter (N=28) of dry spell events are associated with short- to medium-term drought conditions. This indicates that there is only a small connection between dry spells and drought, and while dry spells can occur during longer-term droughts, more dry spells occur during non-drought conditions.

3.5 – Summary and Discussion

In this study, LSMPs related to short-duration dry spells in the Northeast are examined. These LSMPs are identified via the use of *k*-means clustering on the 500 hPa stream function anomaly data for CDD events lasting at least 12 days or longer, and two clusters are shown to adequately represent the data. The key findings from our study are as follows:

1) There is a seasonal preference for DJF and MAM in Cluster 1, and SON in Cluster 2.

2) Cluster 1 is associated with a strong anomalous trough stretching from the midlatitude North American east coast across much of the midlatitude Atlantic Ocean. The pressure trough associated with the first cluster has a north-south zonal wind dipole anomaly that shifts the Atlantic midlatitude zonal jet stream to the south; that dipole anomaly enhances upper-level convergence and sinking motion beneath. This sinking motion, coupled with cold air advection into the Northeast, and accompanied by negative Q850 anomalies due to sinking and changes in horizontal moisture transport, produces an environment of lower-than-normal moisture that suppresses precipitation.

3) Cluster 2 is associated with a strong anomalous ridge over the North American continent which creates a downstream dipole structure in the upper-level zonal wind anomaly that also produces upper-level convergence. Given that cold air advection is weaker here than in the first cluster, the sinking motion is consistent with upper-level convergence and subsidence from the mid-level high-pressure area to the west. This sinking motion, coupled with negative Q850 anomalies due to subsidence and changes to horizontal moisture transport, also suppresses precipitation.

4) Dry spells occur much less frequently during JJA than in other seasons due to the limited influence of ETCs and higher frequency of localized convective precipitation.

5) ETC storm tracks are diverted away from the Northeast during the dry spells, thereby reducing precipitation from ETCs.

6) Individual dry spells can have a mix of the larger-scale features of both cluster means, and so individual events lie on a continuum between two distinct clusters.

7) More dry spells occur in non-drought months than in drought months, meaning that dry spells can occur without pre-existing drought conditions.

Our results provide several promising opportunities for further investigation. Several studies have linked large-scale circulation patterns associated with precipitation variability to low-frequency modes of climate variability, such as the North Atlantic Oscillation (NAO) (e.g., Wallace and Gutzler 1981; Barnston and Livezey 1987), the El Niño-Southern Oscillation (ENSO) (e.g., Trenberth 1997), the Pacific-North American pattern (PNA) (e.g., Wallace and Gutzler 1981; Leathers et al. 1991), and the Madden-Julian Oscillation (MJO) (reviewed in Zhang 2013). Several studies (Namias 1966, Barlow et al. 2001, Seager 2007, and Seager et al. 2012) have shown that these climate modes can influence drought-like conditions over the Northeast. Winter precipitation is more significantly related to the large-scale circulation than in other seasons (Ning et al. 2012a), and as determined in Archambault et al. (2008), Ning and Bradley (2014) and Sukhdeo et al. (2022), these climate modes can have significant influences on certain large-scale patterns that overlap the Northeast region. Any linkage between short-duration dry spells and these low-frequency and remote modes is left for future work.

Historical model simulations can be compared to our reanalysis results to determine the fidelity of models in capturing short duration dry spell properties: the cluster mean structures and their frequency, duration, and intensity. In turn, end-of-century model simulations by those models

can be utilized to gain insight into how these dry spell events may change in future periods. Such work would provide important insight regarding future precipitation conditions in the Northeast.

3.6 – References

Agel L, M. Barlow, J-H, Qian, F. Colby, E. Douglas, and T. Eichler, 2015: Climatology of daily precipitation and extreme precipitation events in the northeast United States. *J. Hydrometeorol*, **16**, 2537–2557, doi:10.1175/JHM-D-14-0147.1.

Archambault, H. M., L. F. Bosart, D. Keyser, and A. R. Aiyyer, 2008: Influence of large-scale flow regimes on cool-season precipitation in the northeastern United States, *Mon. Weather Rev.*, **136**, 2945– 2963, doi:10.1175/2007MWR2308.1.

Barlow, M., S. Nigam, and E. H. Berbery, 2001: ENSO, Pacific decadal variability, and U.S. summertime precipitation, drought, and stream flow, *J. Clim.*, **14**, 2105– 2128, doi:10.1175/1520-0442(2001)014<2105:EPDVAU>2.0.CO;2.

Barnston, A. G., and R. E. Livezey, 1987: Classification, seasonality, and persistence of low-frequency atmospheric circulation patterns, *Mon. Weather Rev.*, **115**, 1083– 1126, doi:10.1175/1520-0493(1987)115<1083:CSAPOL>2.0.CO;2.

Bone, K., G. Pollara, and P. Deppe, 2006: *Water-Works: The Architecture and Engineering of the New York City Water Supply*. Monacelli Press, 268 pp.

Burns, D. A., J. Klaus, and M. R. McHale, 2007: Recent climate trends and implications for water resources in the Catskill Mountain region, New York, USA. *J. Hydrol.*, **336**, 155–170, doi:10.1016/j.jhydrol.2006.12.019.

Cook, E. R., and G. C. Jacoby, 1977: Tree-ring-drought relationships in the Hudson Valley, New York. *Science*, **198**, 399–401, doi:10.1126/science.198.4315.399

Dawson, A., 2016: Windspharm: A High-Level Library for Global Wind Field Computations Using Spherical Harmonics. *Journal of Open Research Software*, **4(1)**, p.e31. doi:10.5334/jors.129.

Gertler, C. G., and P.A. O'Gorman, 2019: Changing available energy for extratropical cyclones and associated convection in Northern Hemisphere summer. *Proceedings of the National Academy of Sciences of the United States of America*, **116**, 4105–4110, doi:10.1073/pnas.1812312116.

Grotjahn, R., 2011: Identifying extreme hottest days from large scale upper air data: A pilot scheme to find California Central Valley summertime maximum surface temperatures. *Clim Dyn.*, **37**, 587–604, doi:10.1007/s00382-011-0999-z.

Grotjahn, R., and M. Osman, 2007: Remote weather associated with North Pacific subtropical sea level high properties. *Int. J. Climatol.*, **27**, 587–602, doi:10.1002/joc.1423.

Grotjahn, R., and Coauthors, 2016: North American extreme temperature events and related large scale meteorological patterns: a review of statistical methods, dynamics, modeling, and trends. *Clim Dyn.*, **46**, 1151–1184, doi:10.1007/s00382-015-2638-6.

Guttman, N. B., 1999: Accepting the Standardized Precipitation Index: A calculation algorithm. *J. Amer. Water Resour. Assoc.*, **35(2)**, 311-322, doi:10.1111/j.1752-1688.1999.tb03592.x.

Hatfield, J., G. Takle, R. Grotjahn, P. Holden, R. C. Izaurralde, T. Mader, E. Marshall, and D. Liverman, 2014: Ch. 6: Agriculture. *Climate Change Impacts in the United States: The Third National Climate Assessment*, J. M. Melillo, Terese (T.C.) Richmond, and G. W. Yohe, Eds., U.S. Global Change Research Program, 150-174. doi:10.7930/J02Z13FR.

Hayhoe, K., and Coauthors, 2007: Past and future changes in climate and hydrological indicators in the US Northeast. *Clim Dyn.*, **28**, 381–407, doi:10.1007/s00382-006-0187-8.

Hersbach H., and Coauthors, 2020: The ERA5 global reanalysis. *Q J R Meteorol Soc.*, **146**, 1999–2049, doi:10.1002/qj.3803.

Horton, R., G. Yohe, W. Easterling, R. Kates, M. Ruth, E. Sussman, A. Whelchel, D. Wolfe, and F. Lipschultz, 2014: Ch. 16: Northeast. *Climate Change Impacts in the United States: The Third National Climate Assessment*, J. M. Melillo, Terese (T.C.) Richmond, and G. W. Yohe, Eds., U.S. Global Change Research Program, 16-1-nn.

Hoskins B.J., and K.I. Hodges, 2002: New perspectives on the northern hemi- sphere winter storm tracks. *J. Atmos. Sci.*, **59**, 1041–1061, doi:10.1175/1520-0469(2002)059%3c1041:npotnh%3e2.0.co;2.

Hurlbut, M. M., and A. E. Cohen, 2014: Environments of northeast U.S. severe thunderstorm events from 1999 to 2009. *Wea. Forecasting*, **29**, 3–22, doi:10.1175/WAF-D-12-00042.1.

Kocin P.J., and L.W. Uccellini, 2004: Northeast Snowstorms. *Meteor. Monogr.*, **54**, Amer. Meteor. Soc., 818 pp. doi:10.1007/978-1-878220-32-5.

Kunkel K.E., D.R. Easterling, D.A.R. Kristovich, B. Gleason, L. Stoecker, and R. Smith, 2012: Meteorological causes of the secular variations in observed extreme precipitation events for the conterminous United States. *J. Hydrometeorol*, **13**, 1131–1141, doi:10.1175/jhm-d-11-0108.1.

Leathers, D. J., B. Yarnal, and M. A. Palecki, 1991: The Pacific/North American teleconnection pattern and United States climate. Part I: Regional temperature and precipitation associations, *J. Clim.*, **4**, 517– 528, doi:10.1175/1520-0442(1991)004<0517:TPATPA>2.0.CO;2.

Lee, Y.-Y., and R. Grotjahn, 2016: California Central Valley summer heat waves form two ways. *J. Climate*, **29**, 1201–1217, doi:10.1175/JCLI-D-15-0270.1.

Lee, Y.-Y., and R. Grotjahn, 2019: Evidence of specific MJO phase occurrence with summertime California Central Valley extreme hot weather. *Advances Atmos. Sci*., **36**(6), 589–602, doi: 10.1007/s00376-019-8167-1.

Lyon, B., N. Christie-Blick, and Y. Gluzberg, 2005: Water shortages, development, and drought in Rockland County, New York. *J. Water Res. Assoc.*, **41**, 1457–1469, doi:10.1111/j.1752-1688.2005.tb03812.x.

Melillo, J. M., T. C. Richmond, and G. W. Yohe, 2014: *Climate Change Impacts in the United States: The Third National Climate Assessment.* U.S. Global Change Research Program, 841 pp., doi:10.7930/J0Z31WJ2.

Nakamura, H., M. Nakamura, and J. L. Anderson, 1997: The role of high- and low-frequency dynamics in blocking formation. *Mon. Wea. Rev.*, **125**, 2074–2093, doi:10.1175/1520-0493(1997)125<2074:TROHAL>2.0.CO;2.

Namias, J., 1966: Nature and possible causes of the northeastern United States drought during 1962–65. *Mon. Wea. Rev.*, **94**, 543–554, doi:10.1175/1520-0493(1966)094<0543:napcot>2.3.co;2.

Namias, J., 1982: Anatomy of Great Plains protracted heat waves (especially the 1980 U.S. summer drought). *Mon. Weather Rev*., **110**, 824–838, doi:10.1175/1520-0493(1982)110<0824:AOGPPH>2.0.CO;2.

Namias, J., 1983: Some causes of United States drought. *J. Climate Appl. Meteor.*, **22**, 30–39, doi:10.1175/1520-0450(1983)022<0030:SCOUSD>2.0.CO;2.

Ning, L., and R. S. Bradley, 2014: Winter precipitation variability and corresponding teleconnections over northeastern United States. *J. Geophys. Res. Atmos.*, **119**, 7931–7945, doi:10.1002/2014JD021591.

Ning, L., M. E. Mann, R. Crane, and T. Wagener, 2012a: Probabilistic projections of climate change for the mid-Atlantic region of the United States—Validation of precipitation downscaling during the historical era, *J. Clim.*, **25**, 509– 526, doi:10.1175/JCLI-D-11-00565.1.

Pfahl S., and H. Wernli, 2012: Quantifying the relevance of cyclones for precipitation extremes. *J Clim.*, **25**, 6770–6780, doi:10.1175/JCLI-D-11-00705.1

Plumb, R. A., 1986: Three-dimensional propagation of transient quasi-geostrophic eddies and its relationship with the eddy forcing of the time–mean flow. *J. Atmos. Sci.*, **43**, 1657–1678, doi:10.1175/1520-0469(1986)043<1657:TDPOTQ>2.0.CO;2.

Reed, K.A. and Coauthors, 2022: Metrics as tools for bridging climate science and applications. *WIRES Clim. Chg*. In press, doi:10.1002/WCC.799.

Rivoire, P., Y. Tramblay, L. Neppel, E. Hertig, and S.M. Vicente-Serrano, 2019: Impact of the dry-day definition on Mediterranean extreme dry-spell analysis. *Nat. Hazards Earth Syst. Sci.*, **19**, 1629–1638, doi:10.5194/nhess-19-1629-2019.

Seager, R., 2007: The turn-of-the-century North American drought: Dynamics, global context, and prior analogues. *J. Climate*, **20**, 5527–5552, doi:10.1175/2007JCLI1529.1.

Seager, R., Y. Kushnir, C. Herweijer, N. Naik, and J. Velez, 2005b: Modeling of tropical forcing of persistent droughts and pluvials over western North America: 1856–2000. *J. Climate*, **18**, 4068–4091, doi:10.1175/JCLI3522.1.

Seager, R., N. Pederson, Y. Kushnir, J. Nakamura, and S. Jurburg, 2012: The 1960s drought and the subsequent shift to a wetter climate in the Catskill Mountains region of the New York City watershed. *J. Climate*, **25**, 6721–6742, doi:10.1175/JCLI-D-11-00518.1.

Seber, G. A., 2009: *Multivariate Observations*. Wiley Series in Probability and Statistics, Vol. 252, John Wiley and Sons, 686 pp.

Spath, H., 1985: *Cluster Dissection and Analysis: Theory, FORTRAN Programs, Examples*. Prentice-Hall, 226 pp.

Stefanon, M., F. D'Andrea, and P. Drobinski, 2012: Heatwave classification over Europe and the Mediterranean region. *Environ. Res. Lett.*, **7**, 014023, doi:10.1088/1748-9326/7/1/014023.

Sukhdeo, R., P.A. Ullrich, and R. Grotjahn, 2022: Assessing the large-scale drivers of precipitation in the northeastern United States via linear orthogonal decomposition. *Clim Dyn*, doi:10.1007/s00382-022-06289-y.

Takaya, K., and H. Nakamura, 2001: A formulation of a phase-independent wave-activity flux for stationary and migratory quasigeostrophic eddies on a zonally varying basic flow. *J. Atmos. Sci.*, **58**, 608–627, doi:10.1175/1520-0469(2001)058<0608:AFOAPI>2.0.CO;2.

Trenberth K.E., G.W. Branstator, and P.A. Arkin, 1988: Origins of the 1988 north american drought. *Science*., **242**, 1640-6455, doi:10.1126/science.242.4886.1640.

Trenberth, K. E., 1997: The definition of El Niño, *Bull. Am. Meteorol. Soc.*, **78**, 2771– 2777, doi:10.1175/1520-0477(1997)078<2771:TDOENO>2.0.CO;2.

Trombulak, S. C., and R. Wolfson, 2004: Twentieth-century climate change in New England and New York, USA. *Geophys. Res. Lett.*, **31**, L19202, doi:10.1029/2004GL020574.

Ullrich P.A., and C.M. Zarzycki 2017: TempestExtremes: a framework for scale-insensitive pointwise feature tracking on unstructured grids. *Geosci. Model. Dev.,* **10**, 1069–1090, doi:10.5194/gmd-10-1069-2017.

Wallace, J. M., and D. S. Gutzler, 1981: Teleconnections in the geopotential height field during the Northern Hemisphere winter, *Mon. Weather Rev.*, **109**, 784– 812, doi:10.1175/1520-0493(1981)109<0784:TITGHF>2.0.CO;2.

Walsh, J., D. Wuebbles, K. Hayhoe, J. Kossin, K. Kunkel, G. Stephens, P. Thorne, R. Vose, M. Wehner, J. Willis, D. Anderson, S. Doney, R. Feely, P. Hennon, V. Kharin, T. Knutson, F. Landerer, T. Lenton, J. Kennedy, and R. Somerville, 2014: Ch. 2: Our Changing Climate. *Climate Change Impacts in the United States: The Third National Climate Assessment*, J. M. Melillo, Terese (T.C.) Richmond, and G. W. Yohe, Eds., U.S. Global Change Research Program, 19-67. doi:10.7930/J0KW5CXT.

Xie, P., A. Yatagai, M. Chen, T. Hayasaka, Y. Fukushima, C. Liu, and S. Yang, 2007: A gauge-based analysis of daily precipitation over East Asia, *J. Hydrometeorol.*, **8**, 607-626.

Xue, Z., and P.A. Ullrich, P.A., 2021: A retrospective and prospective examination of the 1960s U.S. northeast drought. *Earth's Future*, **9**, e2020EF001930, doi:10.1029/2020EF001930.

Zhang, C., 2013: Madden–Julian oscillation: Bridging weather and climate. *Bull. Am. Meteorol. Soc.*, **94**(12), 1849–1870. doi:10.1175/BAMS-D-12-00026.1.

Chapter 4 – Simulation of Northeastern United States Short-Duration Dry Spells and Their Associated Large-Scale Meteorological Patterns by CMIP6 Models

Abstract

Historical simulations from 15 models participating in Phase 6 of the Coupled Model Intercomparison Project (CMIP6) are evaluated for their ability to reproduce several important characteristics related to short-duration dry spells over the northeastern United States and their accompanying large-scale meteorology. The models are compared to observations in terms of capturing the correct number of dry spells, their representation of the associated large-scale meteorological patterns (LSMPs), and their ability to represent upper-level zonal flow, as well as low-level moisture. The LSMPs are identified using *k*-means clustering on the 500-hPa stream function anomaly data during the dry spell events for each data product. There are substantial differences from observations in terms of the models' ability to capture the correct number of dry spell events, with models tending to overestimate the number of short events (1 or 2 days long) and underestimate the number of long events (12 days or longer). Furthermore, while the LSMPs derived in the models are visually similar to those from observations, the location and magnitude of specific troughs and ridges within those patterns, as well as the seasonality of those patterns, may differ substantially from those in observations. Several metrics and a model weighting scheme are devised based on regional characteristics of interest in order to facilitate comparisons between the models and to rank the models based on performance in key categories.

4.1 – Introduction

Droughts are among the most devastating extreme weather events, as they are often responsible for severe impacts on rural communities, regional agriculture, and water management infrastructure (Andreadis and Lettenmaier 2006; Strezepek et al. 2010). With ongoing climate change, many regions are expected to experience increased drought risk due to rising temperatures, increased evapotranspiration, and greater climate variability (Dai 2013; Strezpek et al. 2010). The northeastern United States (hereinafter, the Northeast) is one such region that is anticipated to experience this increased drought risk, particularly with regards to short-duration droughts (dry spells) (Hayhoe et al. 2007; Xue and Ullrich 2021a; Sukhdeo et al. 2023).

At present, climate models are the primary means by which to project anticipated climate change and its potential impacts (Frumhoff et al. 2007; Kharin et al. 2007; Wagener et al. 2010; Xue and Ullrich 2021b, Reed et al. 2022). However, all models are known to possess certain biases which can cause issues with simulation results (Nasrollahi et al. 2015; Moon et al. 2018). Biases present in a single modeling system can be quantified and mitigated using an ensemble of global circulation models (GCMs), such as the multi-model ensemble featured in Phase 6 of the Coupled Model Intercomparison Project (CMIP6) (Eyring et al. 2016). Nonetheless, there is still significant value in understanding these biases in singular models, or across an ensemble, particularly before making climate projections or investing into climate adaptation strategies (Collier et al. 2018; Lee et al. 2018; Eyring et al. 2019). As such, the goal of this work is to evaluate the performance of 15 CMIP6 models with regards to their ability to simulate consecutive dry days, seasonality, and the large-scale meteorology associated with short-duration dry spells over the Northeast.

Short-duration dry spells in the Northeast during the 1961-2021 period have been examined in Sukhdeo et al. (2023), and some of those findings are briefly summarized here. Firstly, a “dry”

day is defined as one in which the area-averaged precipitation for a day is less than 2mm. In this analysis, short-duration dry spells are defined as events in which the area-averaged precipitation is less than 2mm each day for 12 days or longer. The 500-hPa stream function (SF500) anomaly data for these dry spells (n = 103) are extracted and input to *k*-means clustering to determine the circulation patterns associated with these dry spells. Two large-scale meteorological patterns (LSMPs; Grotjahn et al. 2016) are found to be associated with these short-duration dry spells in the Northeast. The first LSMP (Cluster 1) is associated with a strong low-pressure anomaly in the midlatitude Atlantic Ocean, while the second LSMP (Cluster 2) is associated with a strong high-pressure anomaly in east-central North America. Both LSMP configurations produce a dipole anomaly structure in the upper-level zonal wind field that facilitates sinking motion at lower levels. This, coupled with negative low-level moisture anomalies, provides a conducive environment for persistent dry conditions. In terms of seasonality, the first LSMP occurs more preferentially in the winter (DJF) and spring (MAM), while the second LSMP occurs more preferentially in the fall (SON). Dry spells occur least often during the summer, due primarily to the reduced influence of extratropical cyclones and the increased frequency of convective precipitation. Based on the analysis provided by Sukhdeo et al. (2023), the fields that are of most relevance for evaluation in CMIP6 are: 1) the frequency and length of the dry spell events, 2) the seasonal distribution of the dry spell events, 3) the representation of the dry spell SF500 LSMPs, and 4) the corresponding upper-level zonal wind and lower-level moisture LSMPs associated with those SF500 LSMPs.

Our evaluation here prioritizes the correct representation of the dry spell SF500 LSMPs because of their importance to atmospheric circulation, but LSMPs (based on the SF500 LSMPs) are also shown for upper-level zonal wind and low-level moisture. Based on previous evaluations of general circulation models (Fereday et al. 2018; Li et al. 2018; Agel et al. 2020a,b), realistic

representation of circulation patterns is one of the most important factors in producing realistic precipitation. Fereday et al. (2018) found that circulation variability was the leading cause of precipitation variability between considered models. Also, certain types of circulation features may be easier to reproduce than others. Li et al. (2018) found that a general circulation model set in weather forecast mode for an extreme event in the Yangtze River valley reproduced precipitation better when the circulation features had a larger spatial scale. In more recent work, Agel et al. (2020a,b) found that CMIP models vary considerably in their abilities to represent extreme precipitation and its associated LSMPs over the Northeast, with models having issues with the placement of troughs and ridges within the LSMPs. Here, we identify LSMPs by performing *k*-means clustering on the SF500 anomaly field for a set of short-duration dry spell events, which are based on identifying consecutive dry days from a high-resolution gridded precipitation dataset. A similar analysis is performed for selected CMIP6 models, using precipitation and circulation output fields from the "historical" simulations. We choose to identify LSMPs on the 500-hPa level because the stream function field can be calculated from the horizontal winds available for the CMIP6 models, and can capture major synoptic movement and structure.

The remainder of this study is organized as follows. Data is described in Section 4.2. Methodology is discussed in Section 4.3. The major results of this study are presented in Section 4.4. These results are summarized and discussed in Section 4.5.

4.2 – Data

4.2a – Observational and Reanalysis Data

This study makes use of both daily gauge-based precipitation data and daily-averaged reanalysis data. The gauge-based precipitation data come from the CPC Unified Gauge-Based

Analysis of Daily Precipitation over the conterminous United States (Xie et al. 2007). These precipitation data have 0.25° x 0.25° grid spacing, with a spatial domain of 20.125° - 49.875°N, 230.125° - 304.875°E.

Reanalysis data are drawn from the ERA5 dataset (Hersbach et al. 2020) with 0.25° x 0.25° grid spacing and the full, global, spatial domain, for the 1954-2014 period. From ERA5, both daily total fields and anomaly fields are considered for selected atmospheric variables. Before calculating daily anomalies for a particular field, the long-term daily mean of that field (1 January – 31 December) is calculated and smoothed via Fourier-transform by retaining only the first four harmonics of the yearly cycle. Daily anomalies are then calculated by subtracting that Fourier-transformed long-term daily mean from the total field for individual days. The atmospheric fields we consider from ERA5 for this study include: 250-hPa zonal wind (U250), 850-hPa specific humidity (Q850), and 500-hPa horizontal winds (UV500). The 500-hPa stream function field (SF500) is calculated via the windspharm Python package (Dawson 2016) using UV500. These fields are also regridded to 1.0° x 1.0° grid spacing to facilitate comparison with the models.

4.2b – CMIP6 Models

Fifteen CMIP6 models were selected for this study, based on availability (at the time of access) of total precipitation, U250, Q850, and UV500 (used to calculate SF500) associated with the 1954-2014 period within "r1i1p1f1" historical simulations. Table 4.1 lists the model names, their institutions, and their native grid resolutions. Several of the models belong to the same model "family" but with varying resolution or underlying physics. (ex. ACCESS-CM2/ACCESS-ESM1-5). More specific details regarding the atmospheric, ocean, land, and ice components, and the physics and moist process parameterizations, can be found at https://es-doc.org and within the

references in Table 4.1. For each of the models, dry spell events will be identified in the same manner as those for ERA5 (see Section 4.3 for Methodology), and the model data for U250, Q850, UV500, and SF500 are processed identically to the corresponding fields from ERA5.

Reference	Model Name	Native Grid (lon X lat)
Dix et al. (2019)	ACCESS-CM2	192 X 144
Ziehn et al. (2019)	ACCESS-ESM1-5	192 X 144
Swart et al. (2019)	CanESM5	128 X 64
Danabasoglu (2019)	CESM2-WACCM	288 X 192
Lovato and Peano (2020)	CMCC-CM2-SR5	288 X 192
Guo et al. (2018)	GFDL-CM4	288 X 180
Choudhury et al. (2019)	IITM-ESM	192 X 94
Volodin et al. (2019)	INM-CM4-8	180 X 120
Volodin et al. (2019)	INM-CM5-0	180 X 120
Boucher et al. (2018)	IPSL-CM6A-LR	144 X 143
Byun et al. (2019)	KACE-1-0-G	192 X 144
Weiners et al. (2019)	MPI-ESM1-2-LR	192 X 96
Yukimoto et al. (2019)	MRI-ESM2-0	320 X 160
Cao and Wang (2019)	NESM3	192 X 96
W.-L. Lee and Liang (2020)	TaiESM1	288 X 192

Table 4.1 CMIP6 models used in this study, with reference and native grid resolution

4.3 – Methodology

4.3a – Event Isolation

Event isolation follows the procedure used by Sukhdeo et al. (2023). Space and time criteria are used to identify short-duration dry spells from the CPC Unified Gauge precipitation dataset and the model precipitation data to isolate those events in which most of the region experiences dry conditions at the same time. To begin, the CPC Unified Gauge precipitation data is area-averaged in the domain 40-45°N, 70-75°W to generate a daily precipitation time series. For each CMIP6 model, we use the model's precipitation data in its native grid resolution to identify the dry spells. For each model, all of the grid points that fall within the 40-45°N, 70-75°W domain are area-averaged in order to generate the daily precipitation time series for that model. Next, we examine consecutive dry days (CDDs). Each "dry day" must have an area-averaged precipitation

< 2 mm (in following Sukhdeo et al. 2023). The frequency tabulation and duration lengths of these CDD events for both ERA5 and the CMIP6 models are shown in histograms and will be discussed in Section 4.4a.

Following Sukhdeo et al. (2023), when looking at the CDD histogram for observational precipitation, CDD events lasting 12 days or longer represent roughly 11.4% of all "dry" days, according to the < 2 mm criteria. However (as will be discussed), all of the models are not able to cross over the approximate 10% threshold when working with integer days. The dry spell "threshold" for reanalysis and a particular model is one day less than the shortest number of days beyond which there are fewer than 10% of the dry periods. Because the minimum dry spell duration threshold is an integer, more than 10% of the dry spells will equal or exceed this dry spell duration "threshold." This requires us to consider events lasting 9, 10, or 11 days or longer in order to meet the approximate 10% threshold of dry days. For each model, the dry spell duration threshold (9, 10, 11, or 12), as well as the percentage of dry days associated with events lasting 12 days or longer, are labeled on histograms that are discussed in Section 4.4a.

Two potential issues emerge from this event isolation approach: 1) the atmospheric conditions that reinforce the individual dry spell events do not "lock in place" at onset, but rather evolve over time and 2) the dry spell events across all the data products (ERA5 and the CMIP6 models) have different total lengths, ranging from 9 to 39 days. To rectify these issues, we utilize an *n*-day averaging approach (*n* ranging from 9 to 12), whereby we time-average the first *n* total days for each event to generate a composite for that individual event. For example, if a model has its 10% threshold at 9 days or longer, then the time-average would be for the first 9 days of each of its dry events, and if a model has its 10% threshold at 12 days or longer, then the time-average would be for the first 12 days of each of its dry events. Therefore, individual dry spell events (for

each data product) are reconstituted as the time-average of the first *n* days (hereinafter, the onset period) of each respective event. This approach addresses the first issue, since the time-average is a filter isolating low-frequency parts of the fields. For the second issue, by using a relatively similar time-averaging range for events across data products, we can now more reliably compare the large-scale meteorological conditions associated with the different dry spell events across data products.

4.3b – k-Means Clustering

In this study, *k*-means clustering is applied to the SF500 anomaly fields defined for the dry spell events in ERA5 and the CMIP6 models in the domain 30-50°N, 60-90°W. This approach is iterative, and moves events from one group to another until there is no added improvement in reducing the overall distance between patterns amongst events in the created groups (Lee and Grotjahn 2016; Sukhdeo et al. 2023). For our analysis, we choose to apply clustering to the stream function anomaly field rather than the geopotential height anomaly field because stream function produces a discernible pattern in the tropics as well as higher latitudes. Additionally, the 500-hPa level is chosen because it is a commonly used level for showing large-scale, upper-level patterns in the mid-latitudes.

Following Sukhdeo et al. (2023), it was determined that two clusters ($k = 2$ for the *k*-means clustering algorithm) was adequate for sorting the circulation patterns from ERA5 that are associated with the dry spell events. Because we are interested in how well the CMIP6 models can represent the LSMPs associated with these two clusters, the *k*-means clustering will also be performed for $k = 2$ for the model data. Spatial projection analysis is applied (as in Lee and Grotjahn 2016; Sukhdeo et al. 2023) to assess how well individual events are sorted into two

clusters. Projection coefficients p_{kj} of the jth event for a particular model against the kth cluster composite means *of ERA5* are calculated for the same domain of the SF500 anomaly above:

$$p_{kj} = \frac{\sum_{i=1}^{N}(x_i^j y_i^k)}{\sum_{i=1}^{N}(y_i^k)^2}, \quad \text{for } k = 1,2 \text{ and } j = 1,\ldots,n,$$

where k is the cluster, j identifies an individual event, n is the total number of events, i is a specific grid point, N is the total number of grid points, x is the field of a variable of individual events j to be projected, and y^k is the composite mean field of x for cluster k. The projection coefficients for ERA5 and the CMIP6 models are plotted on scatterplots and will be shown and discussed in Section 4.4b.

Additionally, as in Sukhdeo et al. (2023), because we are interested in "true" LSMPs and not just composites of the SF500 anomaly fields, measures of consistency and significance must be calculated. The consistency is measured by using a sign counts procedure (Grotjahn 2011), which involves counting the number of events whose corresponding anomaly field has the same sign of the cluster mean anomaly at each grid point. The sign counts procedure is combined with significance from a bootstrap test to identify true LSMPs (Reed et al. 2022). The bootstrap compares the cluster mean to a large number (order 1000) of random means formed from the same membership size and drawn with replacement. Regions where the cluster mean is $< 5\%$ or $\geq 95\%$ of the random means are labeled significant for the LSMP composites.

4.3c – Determining Multi-Model Mean Weights

As this study is interested in the fidelity of CMIP6 models in representing different aspects of the large-scale meteorology associated with short-duration dry spells in the Northeast, it is reasonable to expect that the models are not all equally adept at representing these characteristics. As such, if we are interested in somehow creating a more optimal performance than by any single model (via a multi-model mean), then each model simulation should not be weighted equally. If differences in model skill are large, then unequal weighting improves the projection (Weigel et al. 2010). Since the multi-model mean is used to estimate some basic properties of the dry spells, such as distribution of longer events, seasonal frequency, and LSMP magnitude and placement, then metrics of those properties are used. Model performance is based on the property being considered, so the weights are based on comparisons between CMIP6 models and reanalysis for multiple historical properties of interest.

The weighting scheme selected is modified from Palipane and Grotjahn (2018), and uses fourteen, squared, inverse, normalized, individual model biases. The relative difference in variable "v" for model "m," $d_{v,m}$, is the model value minus ERA5 value divided by the ERA5 value of variable. The total error for each model is then calculated by summing each model's $d_{v,m}$ terms. The total error ($t_{e,m}$) for each model is used, but normalized by the sum of the total error of all models; hence, a model's weight depends on its performance relative to the corresponding values of other models. From this updated total error ($T_{e,\mathrm{m}}$) for each model, the inverse is taken. The inverse is defined as $IT_{e,m} = 1 / (T_{e,m})$. Fourteen evaluation variables for each model m are used here, and these variables fall into the categories of 1) LSMP magnitude and variability, 2) spatial correlation, 3) CDD distribution, and 4) seasonality. The Category 1 variables are (E1) Cluster 1 LSMP projection coefficient mean, (E2) Cluster 2 LSMP projection coefficient mean, (E3) Cluster

1 LSMP projection coefficient standard deviation, and (E4) Cluster 2 LSMP projection coefficient standard deviation. The Category 2 variables are (E5) Cluster 1 LSMP local spatial correlation, (E6) Cluster 2 LSMP local spatial correlation (domain for E1 through E6 is 30-50°N, 60-90°W), (E7) Cluster 1 LSMP expanded spatial correlation, and (E8) Cluster 2 LSMP expanded spatial correlation (domain for E7 and E8 is 30-60°N, 60-160°W). Each local and expanded spatial correlation carries a sub-weight of 0.50 each for Cluster 1 and Cluster 2. The Category 3 variables are (E9) Kolmogorov-Smirnov (K-S) test statistic and (E10) percentage of dry days associated with events lasting 12 days or longer. Lastly, the Category 4 variables are (E11) percentage of dry events in winter, (E12) percentage of dry events in spring, (E13) percentage of dry events in summer, and (E14) percentage of dry events in fall. E11 through E14 each carry a category sub-weight of 0.25. E1 and E2 assess models' magnitude of the patterns, E3 and E4 assess models' variability between the dry spells of the magnitudes, E5 through E8 assess the shape of the patterns, E9 and E10 assess the CDD distribution for each model, and E11 through E14 assess seasonality. For each model, a root-mean-squared total, S_m, is calculated as $S_m = \sqrt{(IT_{e,m})^2} \; / \; \sqrt{(IT_{e,1})^2 + \cdots + (IT_{e,15})^2}$, where the denominator is the sum of the root-mean-squared total for all models, including model "*m*." The final model weight W_m is defined relative to other models by dividing by the sum of the corresponding "*S*" from every model "*l*": $W_m = S_m / \Sigma S_l$. Therefore, all the W_m values sum to 1. The evaluation metrics, as well as the model weights, are shown in Table 4.2, and are discussed throughout Section 4.4. Normalized differences between the CMIP6 models and ERA5 for these variables are shown in Fig. S10 in the Supplemental Materials section.

Model	E1	E2	E3	E4	E5	E6	E7	E8	E9	E10	E11	E12	E13	E14	Model Weight
ERA5	1.137	1.237	0.514	0.462	1.000	1.000	1.000	1.000	1.000	0.1140	0.342	0.276	0.079	0.303	N/A
ACCESS-CM2	1.207	1.624	0.510	0.592	0.69	0.97	0.84	0.90	0.0769	0.0918	0.444	0.254	0.016	0.286	0.0703
ACCESS-ESM1-5	0.846	1.340	0.470	0.556	0.76	0.98	0.88	0.93	0.1538	0.0678	0.155	0.197	0.014	0.634	0.0601
CanESM5	1.049	1.505	0.523	0.578	0.90	0.99	0.92	0.84	0.1282	0.0640	0.407	0.235	0.025	0.333	0.0721
CESM2-WACCM	1.303	1.505	0.535	0.716	0.92	0.99	0.95	0.89	0.1282	0.0730	0.289	0.289	0.133	0.289	0.0661
CMCC-CM2-SR5	1.052	1.556	0.523	0.799	0.80	0.96	0.90	0.86	0.1538	0.0737	0.415	0.169	0.015	0.400	0.0569
GFDL-CM4	1.021	1.275	0.478	0.404	0.97	0.98	0.92	0.95	0.1538	0.0802	0.432	0.149	0.095	0.324	0.0942
IITM-ESM	0.847	1.334	0.313	0.559	0.97	0.98	0.86	0.95	0.1282	0.0683	0.537	0.134	0.061	0.268	0.0626
INM-CM4-8	0.919	1.417	0.313	0.649	0.96	0.98	0.85	0.96	0.2051	0.0469	0.397	0.181	0.036	0.386	0.0565
INM-CM5-0	1.079	1.372	0.366	0.611	0.96	0.99	0.89	0.93	0.1282	0.0633	0.227	0.180	0.049	0.541	0.0630
IPSL-CM6A-LR	1.216	1.747	0.659	0.813	0.97	0.95	0.95	0.89	0.1282	0.0494	0.286	0.319	0.044	0.352	0.0507
KACE-1-0-G	1.189	1.267	0.553	0.509	0.81	0.98	0.91	0.90	0.1026	0.1128	0.314	0.243	0.186	0.257	0.0928
MPI-ESM1-2-LR	1.231	1.476	0.535	0.844	0.75	0.95	0.86	0.89	0.1282	0.1020	0.442	0.135	0.058	0.365	0.0619
MRI-ESM2-0	1.022	1.557	0.519	0.685	0.91	0.97	0.90	0.90	0.1538	0.0554	0.448	0.192	0.000	0.359	0.0595
NESM3	1.296	1.598	0.610	0.641	0.84	0.96	0.85	0.88	0.0769	0.0972	0.384	0.077	0.090	0.449	0.0627
TaiESM1	0.954	1.436	0.478	0.581	0.96	0.99	0.87	0.87	0.1026	0.0882	0.368	0.132	0.026	0.474	0.0704
AVG1	1.082	1.467	0.492	0.636	0.88	0.97	0.89	0.90	0.1299	0.0756	0.370	0.192	0.056	0.381	0.0671
AVG2	1.099	1.331	0.503	0.602	0.92	0.99	0.97	0.97	0.1284	0.0775	0.371	0.192	0.062	0.374	0.0689

Table 4.2 Evaluation metrics (E1 through E14) for ERA5 and the CMIP6 models in comparison to ERA5. The CMIP6 average for each metric is given in the bottom row. Each model's weight is given in the last column. Model weights sum to 1. The AVG1 row calculates the simple, arithmetic mean for each column. The AVG2 row is a weighted mean (using the weights in the last column), but not of the numbers in the columns for some quantities. For E1, E2, and E5-E8, the weighted pattern is created first before doing the calculations

4.4 – Model Representation of Dry Spell – Related Characteristics

4.4a – CDD Histograms

CDD histogram distributions are shown for ERA5 and the CMIP6 models in Fig. 4.1. In general, the models seem to precipitate too quickly, in that there are too many 1- and 2-day CDD events as compared to ERA5. This leads in part to the models' having issues capturing the right tail end of the CDD distribution (i.e., our short-duration dry spells). For ERA5, the 10% threshold for dry days is achieved when we consider events lasting 12 days or longer (11.4%), and we thus evaluate the models based on whether they can achieve that 10% threshold when considering dry events that last 12 days or longer. One model (KACE-1-0-G; Fig. 4.1l) achieves that almost

identically (11.4% vs. 11.3%, respectively), although this appears to be by chance. Several other models (ACCESS-CM2 (Fig. 4.1b), GFDL-CM4 (Fig. 4.1g), MPI-ESM1-2-LR (Fig. 4.1m), NESM3 (Fig. 4.1o), and TaiESM1 (Fig. 4.1p)) have percentages that range from roughly 8 to 10%. The remaining nine models, with percentages ranging from 4.69% to 7.37%, are least capable of capturing the dry spell events lasting 12 days or longer. The ability to capture the CDD distribution, particularly at the right tail end, does not appear to be entirely related to resolution, as even a higher-resolution model, such as MRI-ESM2-0 (Fig. 4.1n) (native grid: 320 X 160), does not produce the correct distribution as well as a lower-resolution model like MPI-ESM1-2-LR (Fig. 4.1m) (native grid: 192 X 96). Overall, because the models poorly capture the correct number of 1- and 2-day events, and some of the models poorly capture events lasting 12 days or longer, the K-S test statistic values (used for evaluating cumulative distribution; column E9 in Table 4.2) are low when comparing the CMIP6 models to ERA5, with INM-CM4-8 achieving the highest K-S test statistic value of only 0.2051.

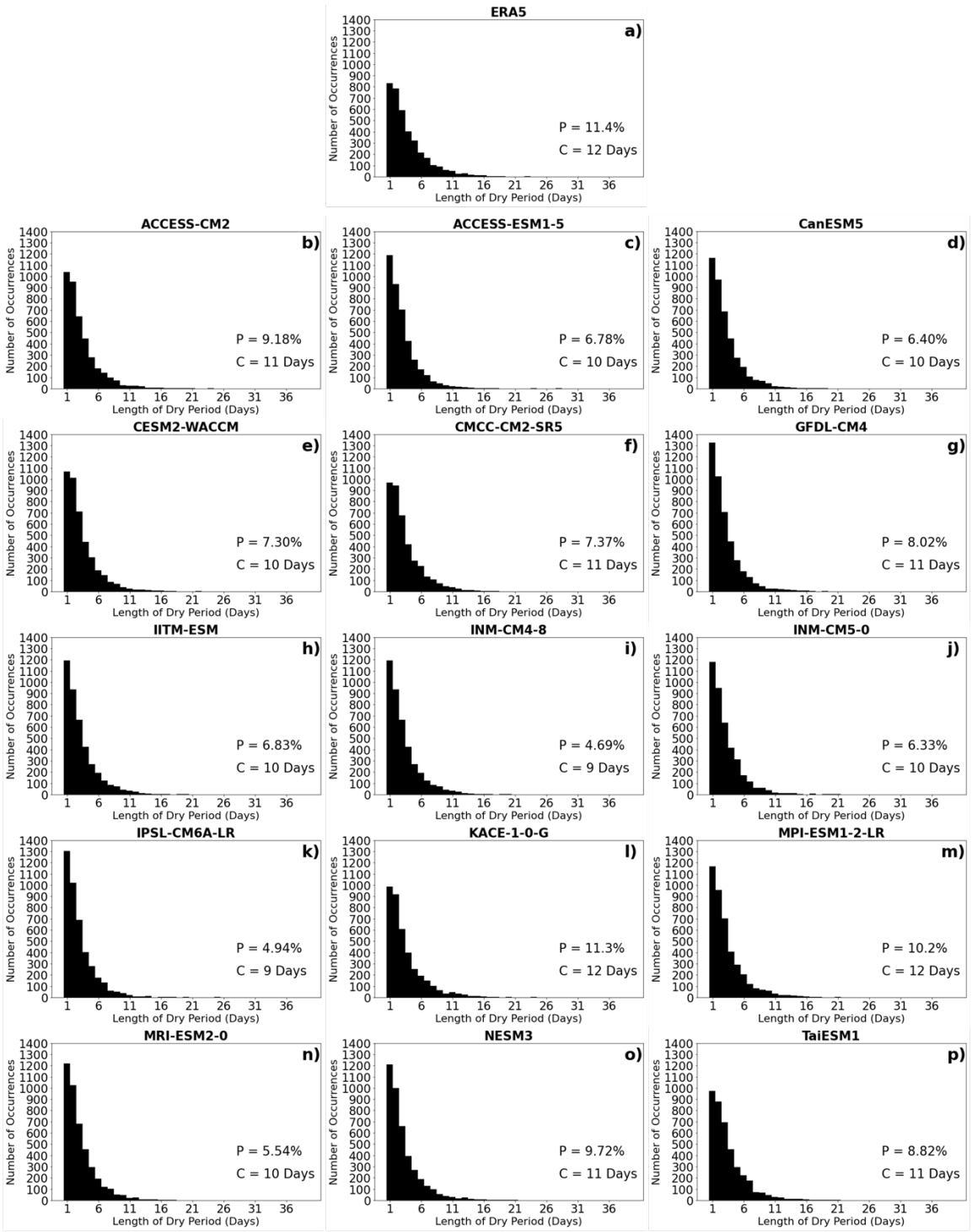

Fig. 4.1 Histogram distribution of consecutive dry day (CDD) events duration in the Northeast from ERA5 and the CMIP6 models for 1954-2014. Lengths of events (in days) are given along the x-axis, with total number of occurrences given along the y-axis. P is each panel is the percentage of dry days associated with events lasting 12 days or longer for each dataset. C in each panel is the cutoff duration for considered dry spell events for that dataset

4.4b – Projection Coefficients Scatterplots

Next, the ability of the CMIP6 models to correctly represent the projection coefficients scatterplot is discussed (see Section 4.3b for Methodology). For each model, the SF500 onset period composites for individual events from the models are projected onto the Cluster 1 and Cluster 2 means *of ERA5*. In the scatterplots (Fig. 4.2), individual events generally fall into groups along a diagonal line between two groups where the projection on one cluster is much higher than the projection onto the other cluster mean. The two cluster means are two ends of a continuum of synoptic patterns that create similar conditions over the Northeast. We want to identify as many events as we can that are assignable to one or the other cluster. In Sukhdeo et al. (2023) using reanalysis data, there are some events that project weakly and/or similarly onto both cluster means. Models behave similarly. These events, here labeled "mixed" (those depicted in-between the dashed lines, offset is 0.70), are excluded from the final sets of cluster constituents. The goal of this approach is to not only determine how well individual events are sorted into their respective cluster, but also to determine if the CMIP6 models capture the correct magnitude with regards to the stream function anomalies in comparison to ERA5.

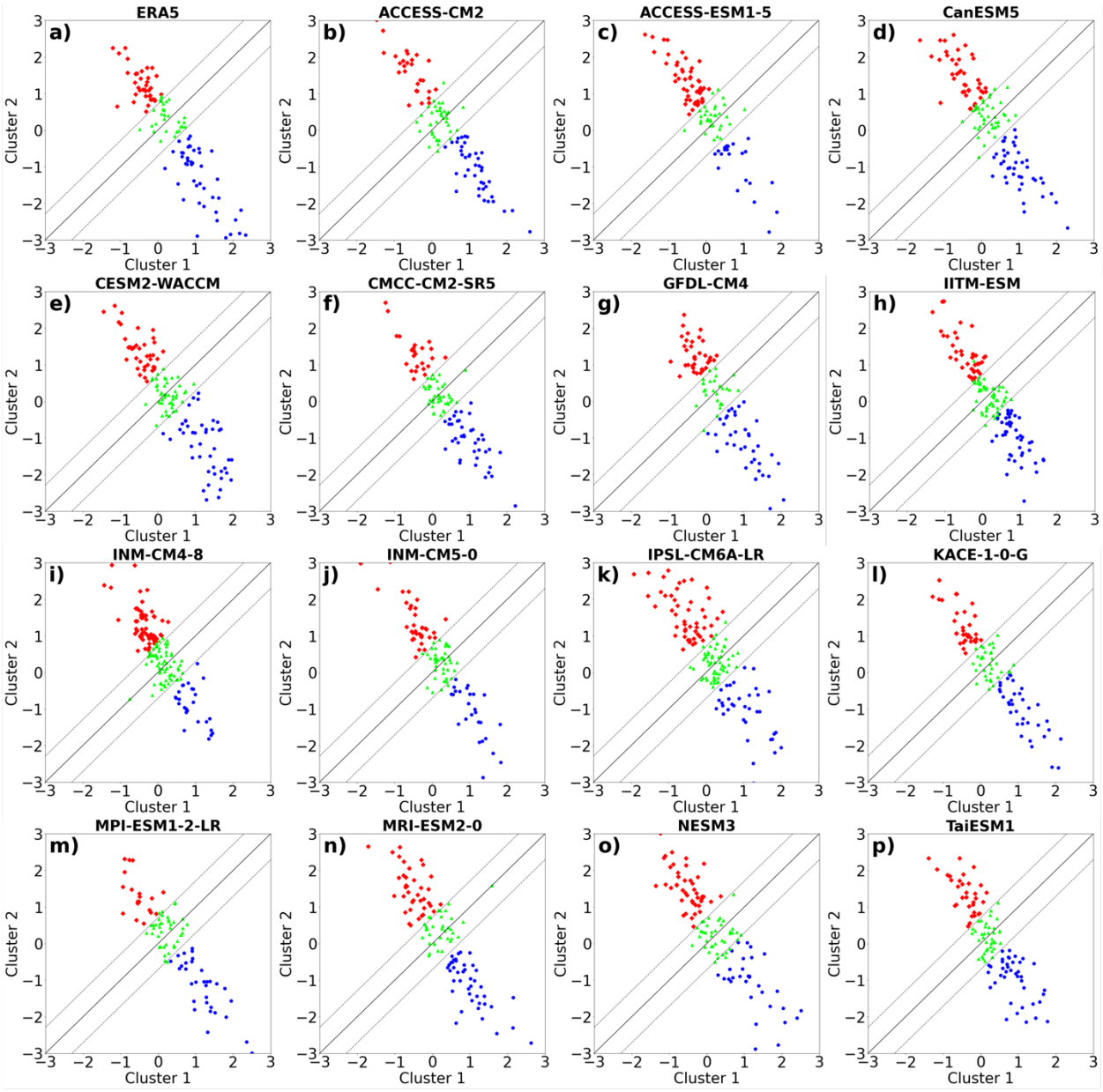

Fig. 4.2 Scatterplot of two projection coefficients for dry spell events from ERA5 and the CMIP6 models. Blue disks mark events in Cluster 1, while red diamonds mark events in Cluster 2, and green triangles mark mixed events and fall within the dashed lines. Dashed lines are used as a visual aid to show the separation of Cluster 1 and Cluster 2 events from mixed events. Shift of the dashed lines from the 1:1 line is 0.70. For individual events, the anomalous 500-hPa stream function field is projected onto the composite means of the two clusters from ERA5. Mixed events are excluded from the analysis hereafter

Firstly, recall that all the models are not equally able to capture the correct number of dry spells lasting 12 days or longer, so in order to reach the 10% dry day threshold, some models are considered with events lasting 9, 10, or 11 days or longer.

The models are able to simulate the key features of the projection coefficients scatterplot of ERA5, with events in Cluster 1 and Cluster 2 generally well-sorted into their respective cluster and mixed events falling along a spectrum in-between the dashed diagonal lines of each scatterplot. However, the models range in their abilities to capture the mean projection value (LSMPi mean) and the standard deviation of the projection values (LSMP std) for each cluster. In terms of the Cluster 1 LSMPi mean, ERA5 has a value of 1.137, meaning that the Cluster 1 constituents on average have a magnitude that is slightly greater than the Cluster 1 mean. For the models, we are also comparing their Cluster 1 constituents to that ERA5 Cluster 1 mean. In general, the models are able to represent the Cluster 1 LSMPi mean value well, with values ranging from 0.846 to 1.303 (column E1 in Table 4.2). Most models have a LSMPi mean value greater than 1, except for ACCESS-ESM1-5, IITM-ESM, INM-CM4-8, and TaiESM1. In terms of the Cluster 1 LSMPi std (column E3 in Table 4.2), the models also compare well with the ERA5 value of 0.514, with the better performing models ranging from 0.470 to 0.553. Several models (IITM-ESM, INM-CM4-8, and INM-CM5-0) have the three lowest values, ranging from 0.313 to 0.366, while NESM3 and IPSL-CM6A-LR have the two largest values of 0.610 and 0.659, respectively.

With regards to the Cluster 2 LSMPi mean and std (columns E2 and E4, respectively, in Table 4.2), the CMIP6 models generally perform poorly in comparison to ERA5, with the models tending to overestimate both quantities. For ERA5, the Cluster 2 LSMPi mean is 1.237. All 15 models have a Cluster 2 LSMPi mean value greater than 1.237, meaning that on average the Cluster 2 constituents for the models have a larger magnitude compared to the ERA5 Cluster 2 mean. The

LSMPi mean values range from 1.267 to 1.747. Two models (GFDL-CM4 and KACE-1-0-G) have values of 1.275 and 1.267, respectively, that are comparable to the 1.237 value of ERA5. In terms of the Cluster 2 LSMPi std, fourteen models have a value that is greater than the 0.462 value for ERA5, with values ranging from 0.509 to 0.779. GFDL-CM4 is the only model that has a value (0.404) less than ERA5's.

Generally, there appears to be a clear dichotomy in the performance of the CMIP6 models when comparing Cluster 1 and Cluster 2 LSMP characteristics to their corresponding characteristics for ERA5. While the models in general capture the LSMPi mean and std of Cluster 1 with some success, they have more variable performance in representing those quantities for Cluster 2, as almost all the models have larger magnitudes for individual events compared to the ERA5 Cluster 2 mean, with more spread around the mean. More specific analysis of the SF500 LSMPs for the models in comparison to ERA5 is provided in Section 4.4d.

4.4c – Seasonality of Dry Spell Events

After removing mixed events for ERA5 and the CMIP6 models, we are also interested in the seasonal distribution of the dry spell events. From Sukhdeo et al. (2023), there is a seasonality associated with the dry spell events, in that Cluster 1 events occur preferentially in DJF and MAM, and Cluster 2 events occur preferentially in SON. Are the CMIP6 models able to capture this seasonality? Bar charts displaying the number of dry spells by month (January – December) for ERA5 and the CMIP6 models are shown in Fig. 4.3. The models vary in their ability to capture the seasonality of the dry spell events. For Cluster 1 DJF, most models are able to capture the peak in dry spell events during this season, with the exception of ACCESS-ESM1-5 (Fig. 4.3c) and INM-CM5-0 (Fig. 4.3j) having too few events. Many more models have issues capturing the correct

number of events for Cluster 1 MAM, with CMCC-CM2-SR5 (Fig. 4.3f), GFDL-CM4 (Fig. 4.3g), IITM-ESM (Fig. 4.3h), INM-CM5-0 (Fig. 4.3j), MPI-ESM1-2-LR (Fig. 4.3m), and NESM3 (Fig. 4.3o) having too few events during this season / cluster combination. Generally, for Cluster 2 SON, most of the models capture the peak in dry spell occurrence, with only a few models (such as ACCESS-ESM1-5 (Fig. 4.3c) and NESM3 (Fig. 4.3o)) having too many events in SON.

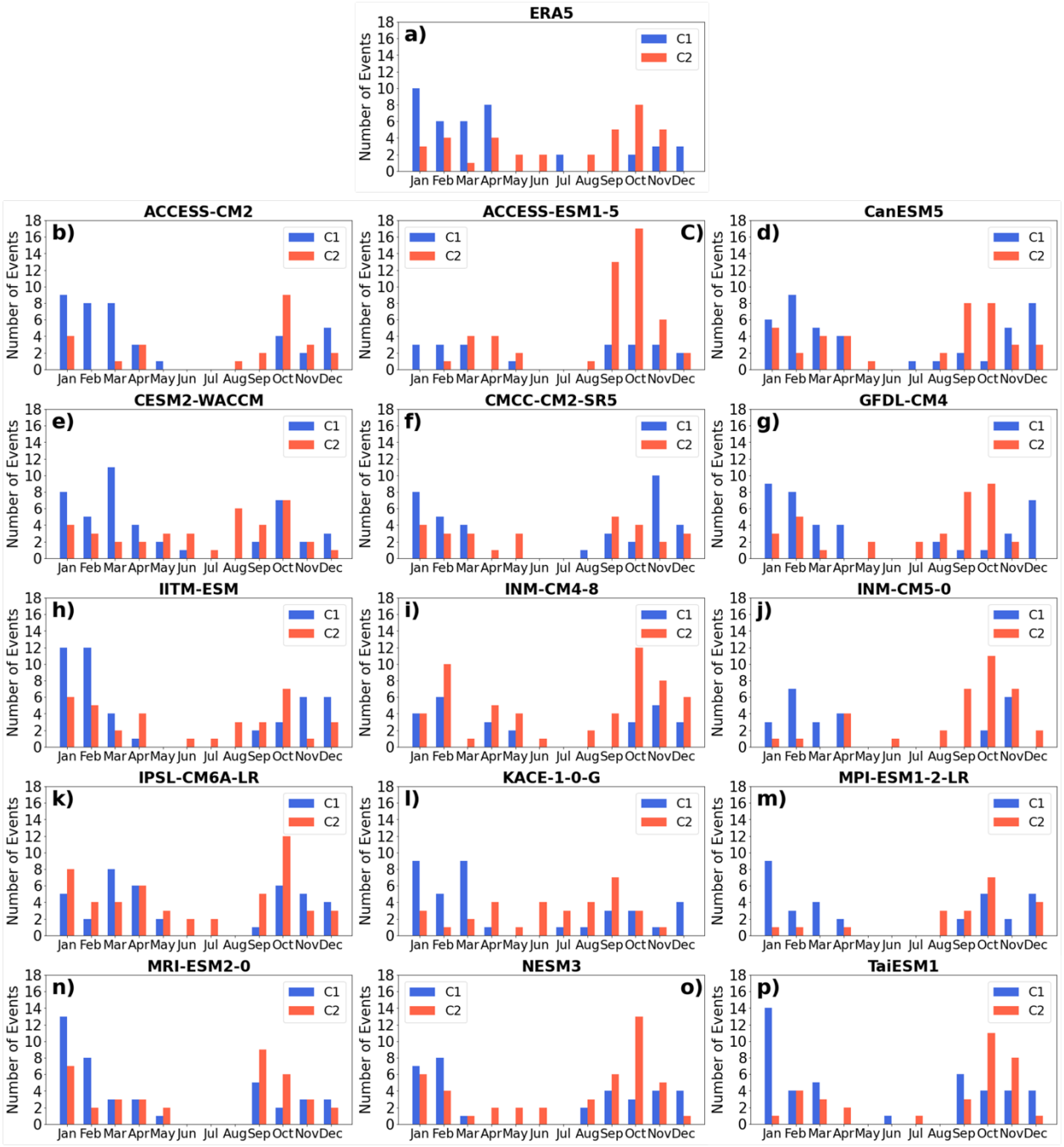

Fig. 4.3 Distribution of dry spell events by month for ERA5 and the CMIP6 models. Mixed events are removed from the total counts for each month. C1 denotes Cluster 1 and C2 denotes Cluster 2

Apart from the bar charts in Fig. 4.3, Table 4.3 also displays the total number of events for each data product (mixed cases removed), and the seasonal breakdown of those events. Models generally perform best during DJF, and struggle to capture the right number of dry spell events during the transition seasons of MAM and SON, a similar result that is found in other studies that have examined the Northeast (i.e., Agel et al. 2020a,b). While not discussed in-depth here, models tend to underrepresent the number of summer (JJA) events, except for CESM2-WACCM, GFDL-CM4, KACE-1-0-G, and NESM3. Lastly, in terms of total number of events (after removing mixed events), there is a difference in what is considered a "mixed event" between some models and ERA5 (and thus a difference in which events are excluded). Several models (ACCESS-CM2, CMCC-CM2-SR5, INM-CM5-0, MPI-ESM-1-2-LR) only have 63, 65, 61, and 52 events, respectively, while IPSL-CM6A-LR has too many events at 91. Overall, while some models can generally capture the correct seasonality of the dry spell events, several others cannot, particularly during the spring and fall transition seasons.

Model Name	DJF	MAM	JJA	SON	TOTAL
ERA5	**26**	**21**	**6**	**23**	**76**
ACCESS-CM2	28	16	1	18	63
ACCESS-ESM1-5	11	14	1	45	71
CanESM5	33	19	2	27	81
CESM2-WACCM	24	24	11	24	83
CMCC-CM2-SR5	27	11	1	26	65
GFDL-CM4	32	11	7	24	74
IITM-ESM	44	11	5	22	82
INM-CM4-8	33	15	3	32	83
INM-CM5-0	14	11	3	33	61
IPSL-CM6A-LR	26	29	4	32	91
KACE-1-0-G	22	17	13	18	70
MPI-ESM1-2-LR	23	7	3	19	52
MRI-ESM2-0	35	15	0	28	78
NESM3	30	6	7	35	78
TaiESM1	28	10	2	36	76

Table 4.3 Seasonal count of dry spell events (middle four columns) and total count of dry spell events (last column) for ERA5 and the CMIP6 models. Mixed events are not included in the counts

4.4d – SF500 LSMPs

In this section, we discuss the CMIP6 models' representation of the primary LSMPs (defined by the SF500 anomaly fields) for Cluster 1 and Cluster 2. The *k*-means clustering analysis produces two SF500 patterns that are visually very similar to those produced for ERA5 for most of the models. However, there are some key differences.

For Cluster 1 (Fig. 4.4), the models are able to capture the strong low-pressure anomaly located in the mid-latitude Atlantic Ocean, with varying skill in terms of representing the average magnitude of the anomaly as well as its placement. The magnitude of the anomaly (in comparison to ERA5) was addressed in Section 4.4b with the LSMPi mean statistic (column E1 in Table 4.2). The models have LSMPi mean values ranging from 0.846 to 1.303, with most models having a

value > 1, except for ACCESS-ESM1-5, IITM-ESM, INM-CM4-8, and TaiESM1. A value < 1 indicates that on average the model LSMP is weaker than the one for ERA5 near the Northeast, and visual inspection of Fig. 4.4 for these models confirms this. The remaining models, with a value > 1, have a model LSMP that is stronger than ERA5's. The larger LSMP magnitude for these models is also observed when looking at Cluster 1 DJF LSMPs (see Supplemental Materials).

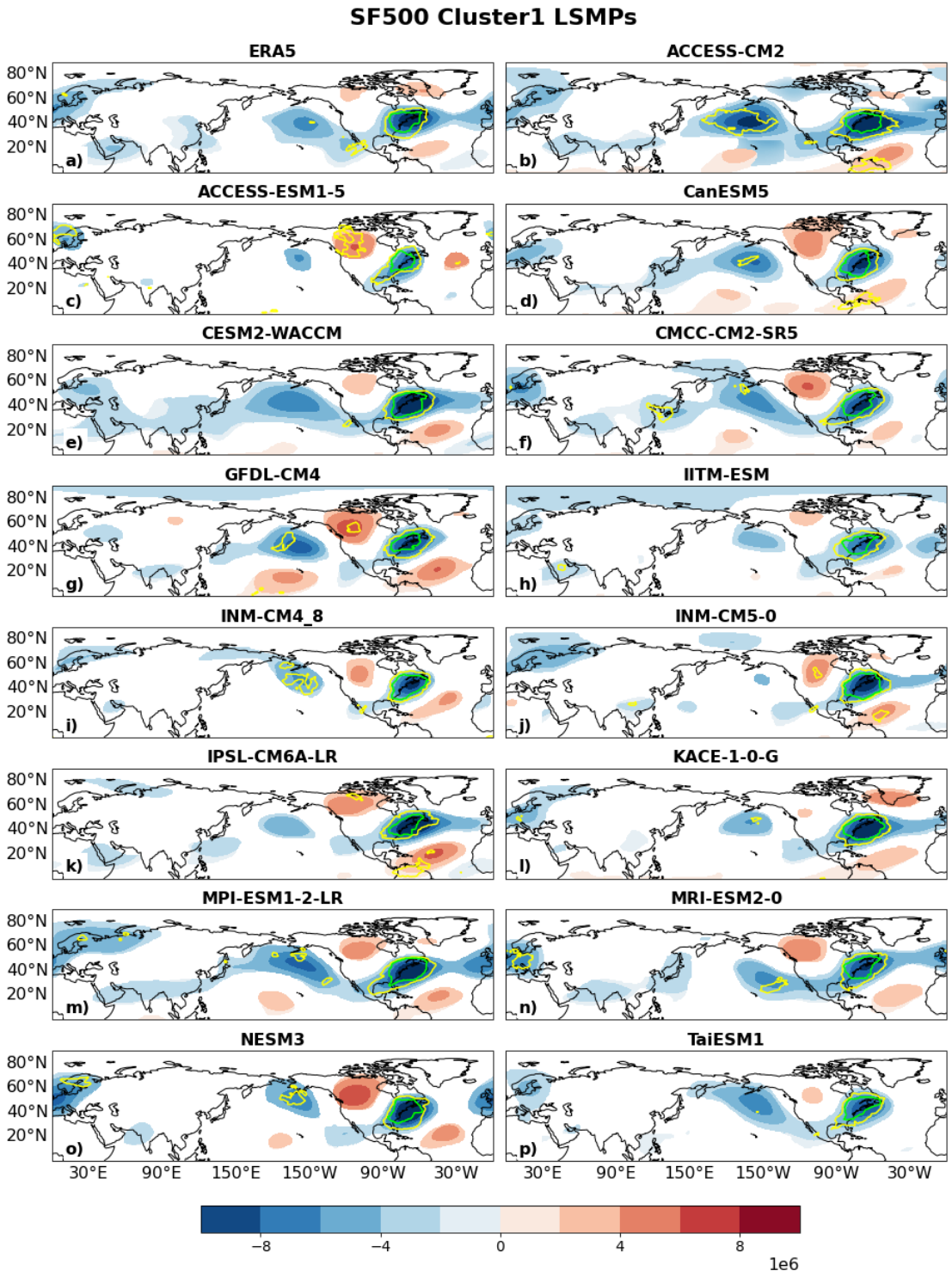

Fig. 4.4 Large-scale meteorological patterns (LSMPs), defined by the 500-hPa stream function anomaly field (m^2/s; contours), for the short-duration dry spell events in Cluster 1 for ERA5 and the CMIP6 models. Contour shading indicates areas of significance determined by bootstrap resampling. Yellow and green contours indicate: sign count magnitude of 0.6 and 0.8, such that 80% and 90% of the members in the cluster have the same sign, respectively. Stream function values are scaled by 10^6

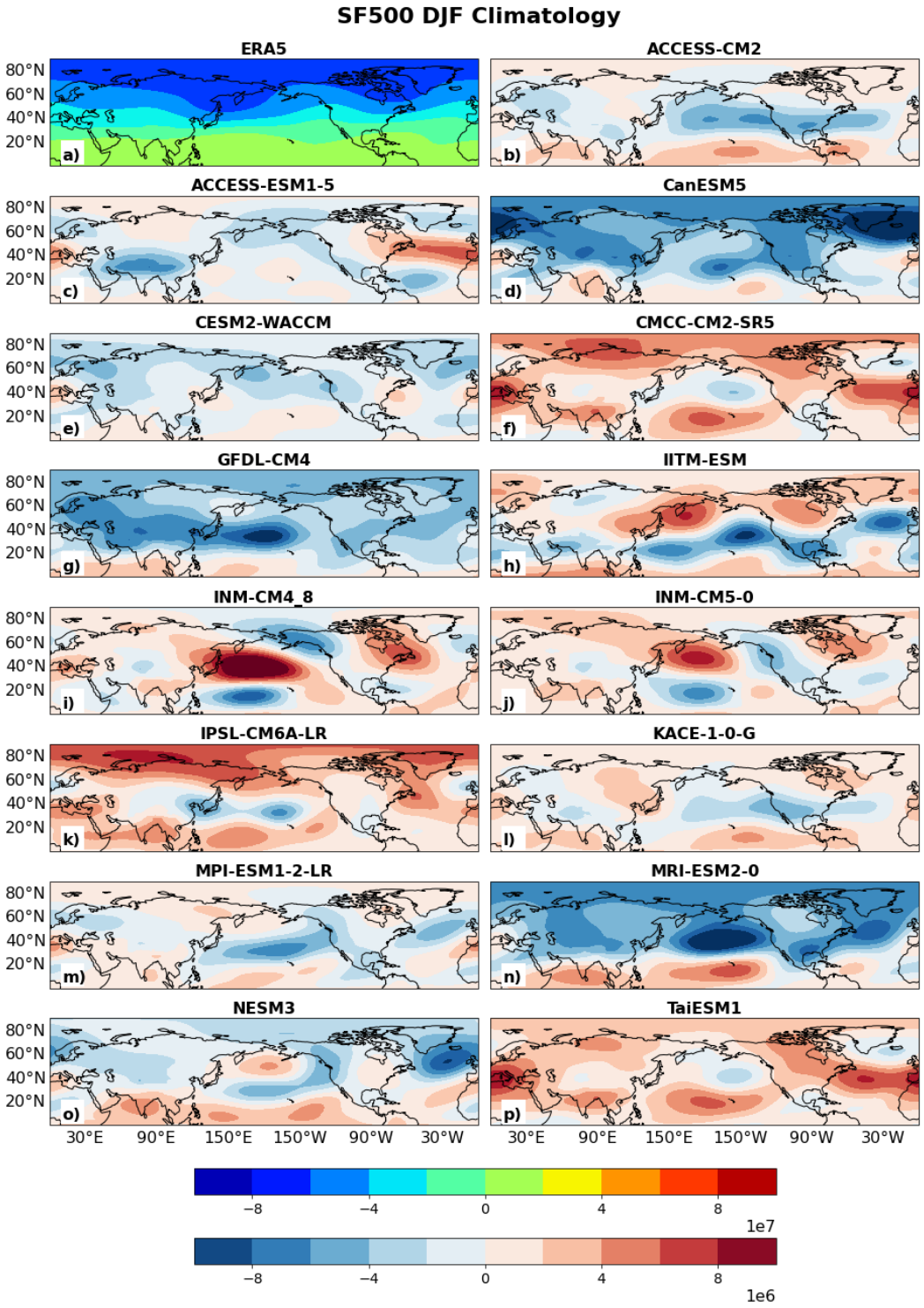

Fig. 4.5 ERA5 climatological mean SF500 field for DJF in a). Panels b-p show the difference between each model's climatological mean in DJF and ERA5's (model mean – ERA5 mean). Stream function values are scaled by 10^6, with units of m^2/s

In addition to LSMP magnitude, the placement of the Cluster 1 LSMP is also considered using spatial correlation. Spatial correlation is considered not only for the main LSMP area (domain: 30-50°N, 60-90°W), but also for an expanded section of the Northern Hemisphere (domain: 30-60°N, 60-160°W). The purpose of examining the larger domain is to determine how well the models are able to capture the hemispheric Rossby wave-train structure. For the local spatial correlation (column E5 in Table 4.2), 9 of the 15 models have a value > 0.90, so the LSMP placement is well-captured. ACCESS-CM2, ACCESS-ESM1-5, CMCC-CM2-SR5, KACE-1-0-G, MPI-ESM1-2-LR, and NESM3, however, have smaller local spatial correlation values than the other models, with values between 0.69 and 0.84. ACCESS-CM2 (Fig. 4.4b) and KACE-1-0-G (Fig. 4.4l) have an Atlantic LSMP low that is about 2° lower than that of ERA5, whereas the other four models do not capture the zonal orientation of the LSMP, instead having an LSMP that is oriented in the southwest-to-northeast direction along the eastern United States coast. For the expanded spatial correlation (column E7 in Table 4.2), the models generally perform well, with values ranging from 0.84 to 0.95, so they are able to capture the larger Rossby wave structure. Models that have a poor local spatial correlation have a notably improved value for the expanded spatial correlation of the larger domain.

For Cluster 2 (Fig. 4.6), like for Cluster 1, the models are able to capture the strong high-pressure anomaly located in east-central North America. For LSMP magnitude (measured with the LSMPi mean statistic; column E2 in Table 4.2), all of the models have a value > 1, ranging from 1.267 to 1.747, indicating that on average the model LSMPs have a larger magnitude than ERA5's. Models such as KACE-1-0-G and GFDL-CM4 are closer to ERA5, with LSMPi means values of 1.267 and 1.275, respectively, while other models, such as ACCESS-CM2 and IPSL-CM6A-LR

have much larger values of 1.624 and 1.747, respectively. This positive bias in the high-pressure anomaly also shows up prominently for Cluster 2 SON LSMPs (see Supplemental Materials).

Regarding local spatial correlation, there is much less variability in the models for Cluster 2 as compared to Cluster 1. Model local spatial correlation values (column E6 in Table 4.2) for Cluster 2 range from 0.95 to 0.99, indicating that the models are able to capture the LSMP placement well. This is confirmed by visual inspection of Fig. 4.6. Models generally capture the circular nature of the high pressure anomaly, with some models (such as CMCC-CM2-SR5 (Fig. 4.6f) and IPSL-CM6A-LR (Fig. 4.6k)) having a high-pressure that is slightly more elongated in the southwest-to-northeast direction. When considering the expanded spatial correlation (column E8 in Table 4.2), there is more skill disparity amongst the models. While all of the models have a reduced spatial correlation value compared to the local value, how much the values are decreased depends on the model. The expanded spatial correlation values range from 0.84 to 0.96. The disparity in the expanded spatial correlation is related to the representation of the high-low-high anomaly tripole that extends from just north of Hawaii through east-central North America. The models vary in the extent to which they highlight the tripole, with models such as ACCESS-CM2 (Fig. 4.6b) and CanESM5 (Fig. 4.6d) having a fully-observed tripole, GFDL-CM4 (Fig. 4.6g) having portions of the tripole, and MRI-ESM2-0 (Fig. 4.6n) having a pattern that looks more similar to that of ERA5. ERA5 has elements of the tripole (Fig. 4.6a); however, large portions of the high-pressure anomaly in the central Pacific and the low-pressure anomaly near Alaska that appear in the model LSMPs do not show up for ERA5 because they do not pass the bootstrap significance testing there. The presence of the tripole across multiple models and partially in ERA5 may indicate that there is a teleconnection mechanism linking the central Pacific to east-central North America for Cluster 2, but exploring such a link is beyond the scope of this study.

The varying skill of the models to represent LSMP magnitude and placement may be partly related to biases in the DJF climatology of the SF500 field for Cluster 1 (Fig. 4.5), as a negatively or positively biased climatology can influence the calculated SF500 anomaly fields that are used to generate the LSMPs. For example, ACCESS-CM2 (Fig. 4.4b; Fig. 4.5b) and KACE-1-0-G (Fig. 4.4l; Fig. 4.5l) have a negatively biased climatology in the mid-latitude Atlantic Ocean during DJF, so the LSMP does not have to be as negative as the LSMP of ERA5 to generate a similar total field. Conversely, ACCESS-ESM1-5 (Fig 4.4c; Fig. 4.5c) and CMCC-CM2-SR5 (Fig 4.4f; Fig. 4.5f) have a positively biased climatology in the mid-latitude Atlantic Ocean. As such, this can lead to anomalies being more positive (i.e., weaker magnitude) compared to ERA5. If those model biases (here model bias refers to model minus ERA5) are subtracted away from the Cluster 1 DJF composite means for those models (not shown), both the local spatial correlation and pattern projection are improved when compared to ERA5. For other models, such as CESM2-WACCM (Fig. 4.5e) and GFDL-CM4 (Fig. 4.5g), subtracting away any climatological biases worsens the local spatial correlation and pattern projection, indicating that the model climatologies already compare well to ERA5 locally without any sort of "bias correction."

Similarly for the Cluster 2 LSMPs, model biases in the climatological SF500 field in SON may play a role in causing the observed biases for some of the Cluster 2 LSMPs (SON events make the majority of events in Cluster 2). For example, CMCC-CM2-SR5 (Fig. 4.7f), INM-CM4-8 (Fig. 4.7i), and TaiESM1 (Fig. 4.7p) have strong positive biases over east-central North America in their SF500 SON climatologies. While LSMP placement is already well-captured for the CMIP6 models for Cluster 2, subtracting away these climatological biases does improve the pattern projection in comparison to ERA5. Other models, such as ACCESS-CM2 (Fig. 4.7b) and MRI-ESM2-0 (Fig. 4.7n) have greater negative biases over east-central North America as compared to the adjacent

Atlantic Ocean (i.e., opposite pattern to the LSMP) in their SON climatologies. As such, when looking at the corresponding Cluster 2 LSMPs for ACCESS-CM2 and MRI-ESM2-0 (Fig. 4.6b and Fig. 4.6n, respectively), there appears to be a larger LSMP magnitude than in ERA5 in east-central North America, and that is consistent with the E2 values for these models in Table 4.2.

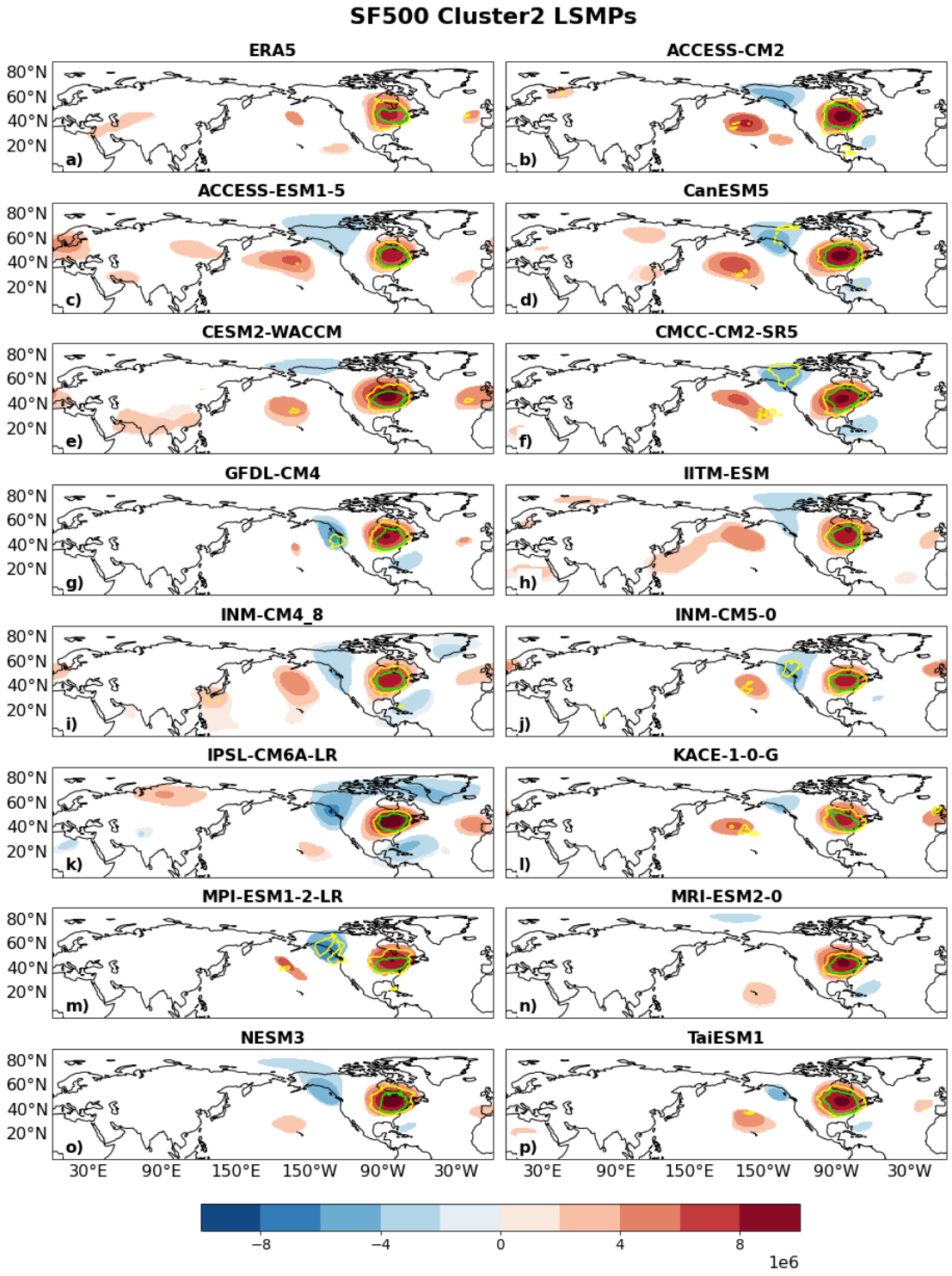

Fig. 4.6 Same format as **Fig. 4.4**, but for Cluster 2

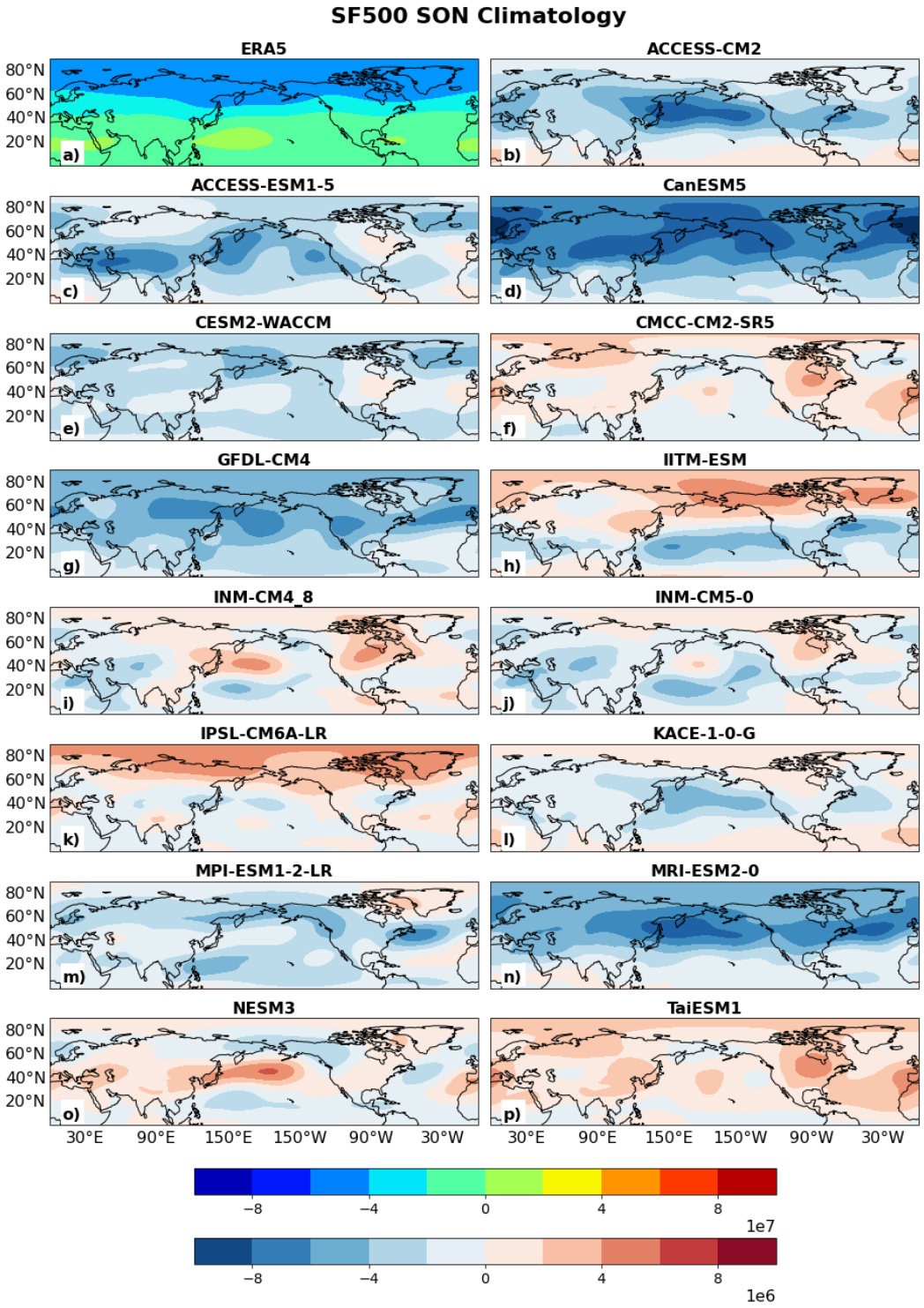

Fig. 4.7 Same format as **Fig. 4.5**, but for SF500 climatological mean in SON

Overall, the CMIP6 models are able to visually approximate the Cluster 1 and Cluster 2 LSMPs, but vary considerably in their abilities to correctly represent LSMP magnitude and placement as compared to ERA5. Some models underestimate the LSMP magnitude of Cluster 1, while most overestimate it; for Cluster 2, all models overestimate the LSMP magnitude. Model deficiencies in representing the LSMPs may be partially related to model biases in the SF500 climatology for DJF and SON. For local spatial correlation, the models vary in skill for Cluster 1, and are very good for Cluster 2. When looking at the expanded spatial correlation, however, Cluster 1 values tend to improve for all models, whereas values are lower for Cluster 2. Understanding the reasons for these differences between local and expanded spatial correlation is beyond the scope this present work.

4.4e – U250 LSMPs

While this study is primarily interested in the representation of the dry spell SF500 anomaly LSMPs in the CMIP6 models, the 250-hPa zonal wind (U250) anomaly LSMPs that are associated with our SF500 anomaly LSMPs are also considered. Sukhdeo et al. (2023) showed that for both clusters, the SF500 LSMPs create a dipole structure in the 200-hPa zonal wind (U200) anomaly field. This configuration leads to upper-level convergence of ageostrophic winds, which subsequently facilitates sinking motion at lower levels, which is expected under conditions where precipitation is reduced or minimized. Additionally, changes to jet stream strength and positioning can influence the development of LSMPs associated with extreme weather events (Grotjahn et al. 2016). For these reasons, we examine how well the CMIP6 models are able to represent this upper-level zonal wind dipole.

Looking at the U250 LSMPs for Cluster 1 (Fig. 4.8), the models visually capture the U250 LSMPs, with a negative U250 anomaly located in southeastern Canada and a positive U250 anomaly located at about 20°N in the mid-latitude Atlantic Ocean. Generally, the magnitude of the U250 dipoles scales with the magnitude of the SF500 LSMPs. ACCESS-ESM1-5 (Fig. 4.8c), IITM-ESM (Fig. 4.8h), INM-CM4-8 (Fig. 4.8i), and TaiESM1 (Fig. 4.8p) have a U250 dipole that is weaker than that of ERA5 (Fig. 4.8a), whereas CESM2-WACCM (Fig. 4.8e), CMCC-CM2-SR5 (Fig. 4.8f), IPSL-CM6A-LR (Fig. 4.8k), KACE-1-0-G (Fig. 4.8l), MPI-ESM1-2-LR (Fig. 4.8m), and NESM3 (Fig. 4.8o) have a U250 dipole that is stronger in magnitude than that of ERA5. The remaining models have magnitudes that are similar to that of ERA5. Additionally, the U250 dipole for ACCESS-ESM1-5 (Fig. 4.8c), CMCC-CM2-SR5 (Fig. 4.8f), INM-CM4-8 (Fig. 4.8i), MPI-ESM1-2-LR (Fig. 4.8m), and NESM3 (Fig. 4.8o) has a southwest-to-northeast orientation as compared to the more zonal orientation of ERA5's.

The models are also able to visually capture the U250 dipole associated with Cluster 2 (Fig. 4.9). However, due to the strong positive biases associated with the SF500 LSMPs of the models, the U250 LSMPs are also stronger in magnitude as compared to ERA5 (Fig. 4.9a). Some models (ACCESS-CM2 (Fig. 4.9b), ACCESS-ESM1-5 (Fig. 4.9c), CanESM5 (Fig. 4.9d), and KACE-1-0-G (Fig. 4.9l)) also have a secondary U250 dipole in the north-central Pacific, due to each model having a significant high-pressure anomaly in the region in their SF500 LSMPs.

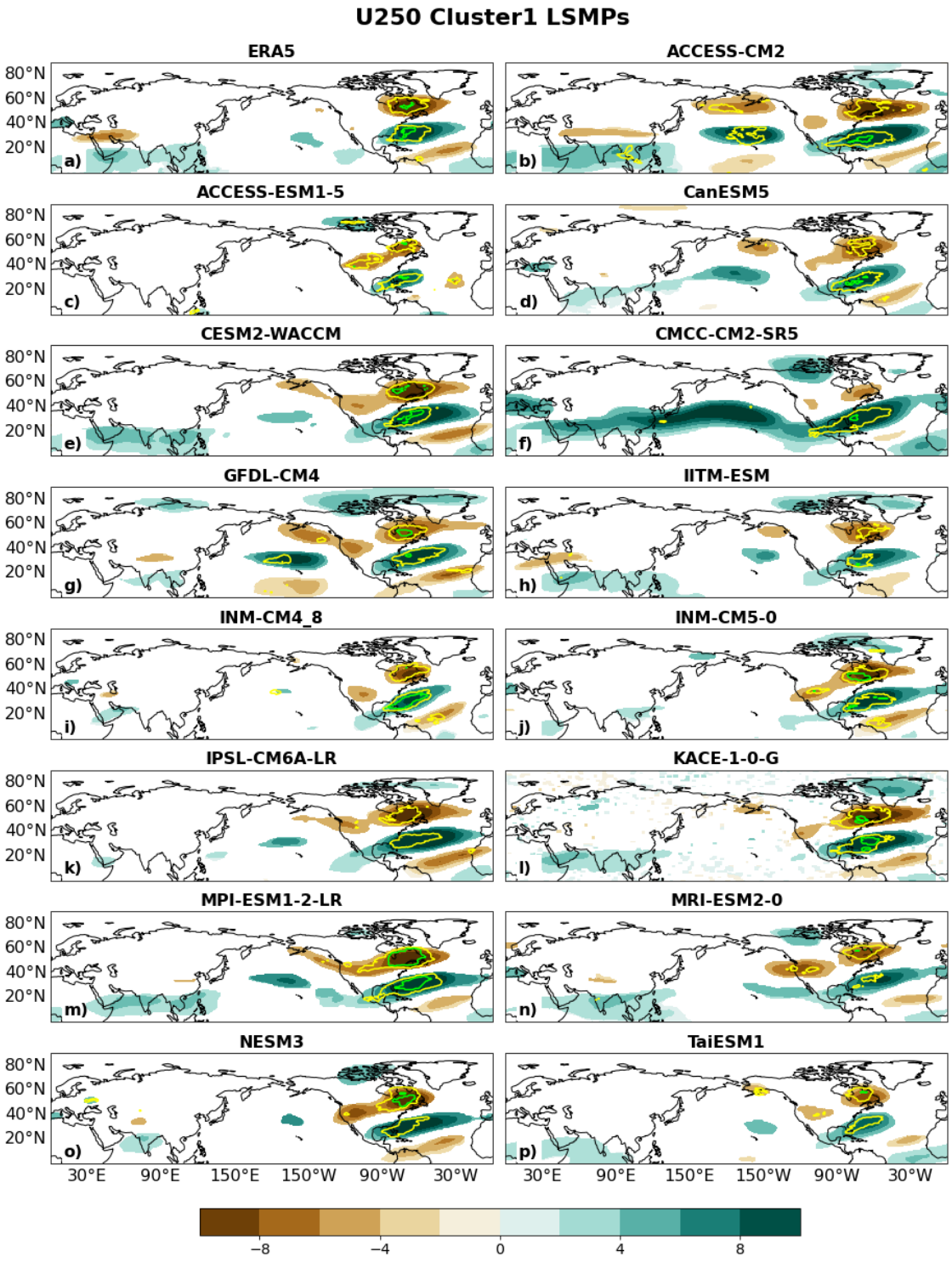

Fig. 4.8 Large-scale meteorological patterns (LSMPs), defined by the 250-hPa zonal wind anomaly field (m/s; contours), for the short-duration dry spell events in Cluster 1 for ERA5 and the CMIP6 models. Contour shading indicates areas of significance determined by bootstrap resampling. Yellow and green contours indicate: sign count magnitude of 0.6 and 0.8, such that 80% and 90% of the members in the cluster have the same sign, respectively

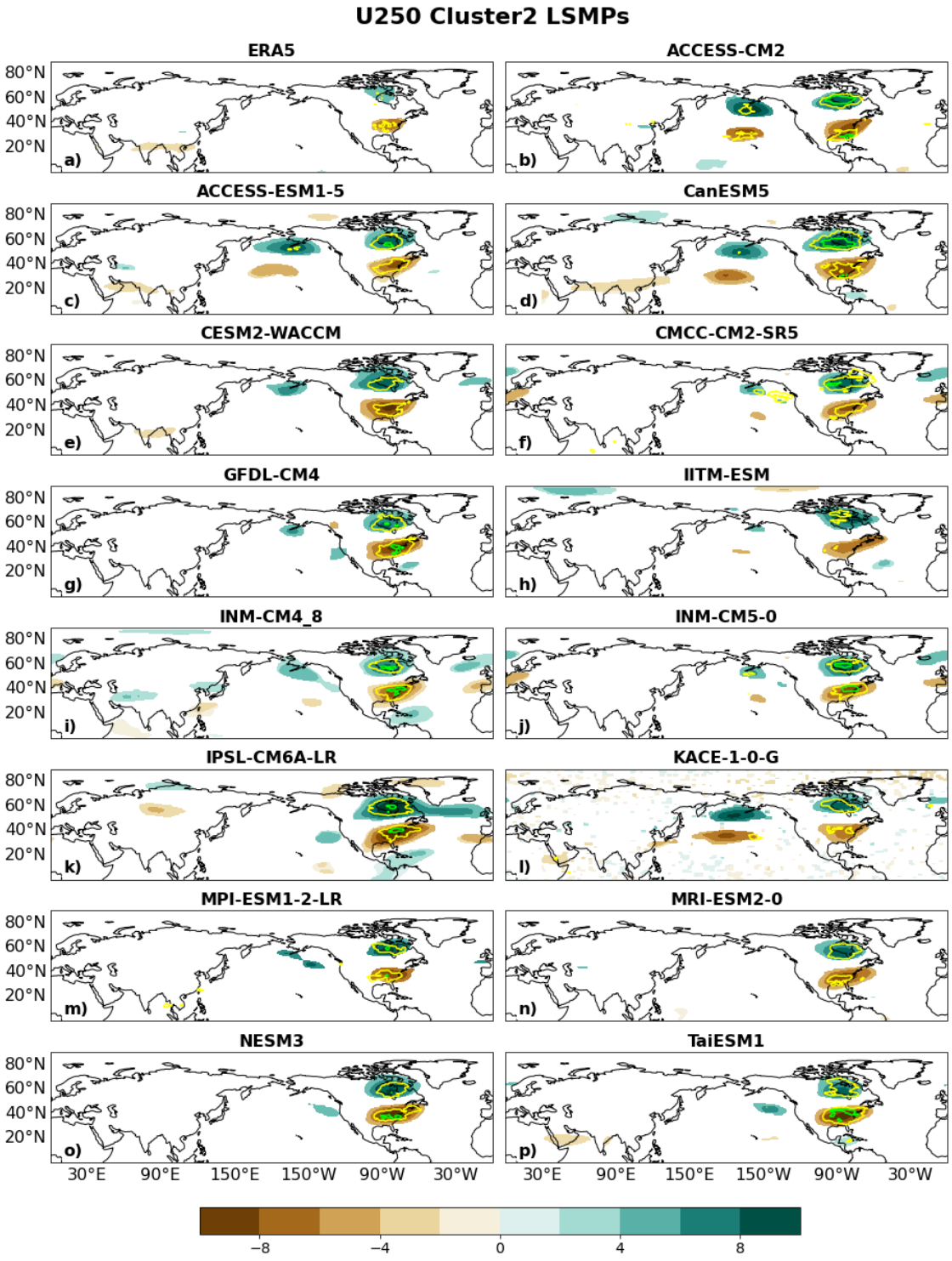

Fig. 4.9 Same format as **Fig. 4.8**, but for Cluster 2

As discussed, biases in the SF500 climatology for each of the models may in part be responsible for biases in the SF500 LSMPs. Are similar biases observed in each model's respective U250 climatology? To determine this, we calculate U250 climatological means for DJF and SON for each of the models (Fig. 4.10 and Fig. 4.11, respectively). As for the SF500 LSMPs, these seasons are prioritized because dry spell events in DJF and SON make up the majority of events in Cluster 1 and Cluster 2, respectively. The models range in the ability to represent the climatological jet in both seasons, particularly with regards to the jet latitude in the domain of 20-60°N, 30-100°W.

In DJF, most models have a climatological jet latitude that is within ± 2° of ERA5 (~38.1°). ACCESS-CM2 (Fig. 4.10b) and KACE-1-0-G (Fig. 4.10l) have a climatological jet that is noticeably farther south as compared to ERA5 (~33.3° and 34.8°, respectively). Consequently, the Cluster 1 U250 LSMPs for ACCESS-CM2 (Fig. 4.8b) and KACE-1-0-G (Fig. 4.8l) have an anomaly dipole that is also farther south as compared to ERA5. This positioning of the U250 anomaly dipole for these models for Cluster 1 may be related to why the SF500 LSMPs for those models (Fig. 4.4b and Fig. 4.4l, respectively) have smaller local spatial correlation values of 0.69 (ACCESS-CM2) and 0.81 (KACE-1-0-G) when compared to ERA5.

In SON, only CMCC-CM2-SR5 (Fig. 4.11f), NESM3 (Fig. 4.11o), and TaiESM1 (Fig. 4.11p) have a jet latitude that is within ± 2° of the ~46.7° jet latitude of ERA5 (~48.8°, 48.3°, and 44.7°, respectively). Three models (CESM2-WACCM (Fig. 4.11e), INM-CM4-8 (Fig. 4.11i), and INM-CM5-0 (Fig. 4.11j)) have a greater than 2° higher jet latitude than ERA5, while the remaining 9 models have a greater than 2° lower jet latitude than ERA5. Unlike for Cluster 1, the climatological jet positioning for SON does not appear to impact Cluster 2 LSMP structure, as all models have a local spatial correlation value for Cluster 2 of at least 0.95. It is, however, unclear

whether the differences in the climatological jet positioning for the models in SON (either a lower or higher jet) impacts LSMP magnitude, as all models have a larger mean pattern projection when compared to ERA5 for Cluster 2.

Given that jet placement can play an important role in the placement of high and low pressure systems, their magnitude and persistence, as well as the shifting of storm tracks for ETCs that would otherwise impact the Northeast (Sukhdeo et al. 2023), it is likely that biases in the U250 climatologies, in conjunction with biases in the SF500 climatologies, may be partly responsible for biases in the SF500 LSMPs, particularly for Cluster 1. Diagnosis of the causes of climatological biases in the SF500 and U20 fields is beyond the scope of this present work, but research into understanding how these biases may impact model representation of SF500 LSMPs could be very useful for model improvements in representing regional large-scale meteorological conditions.

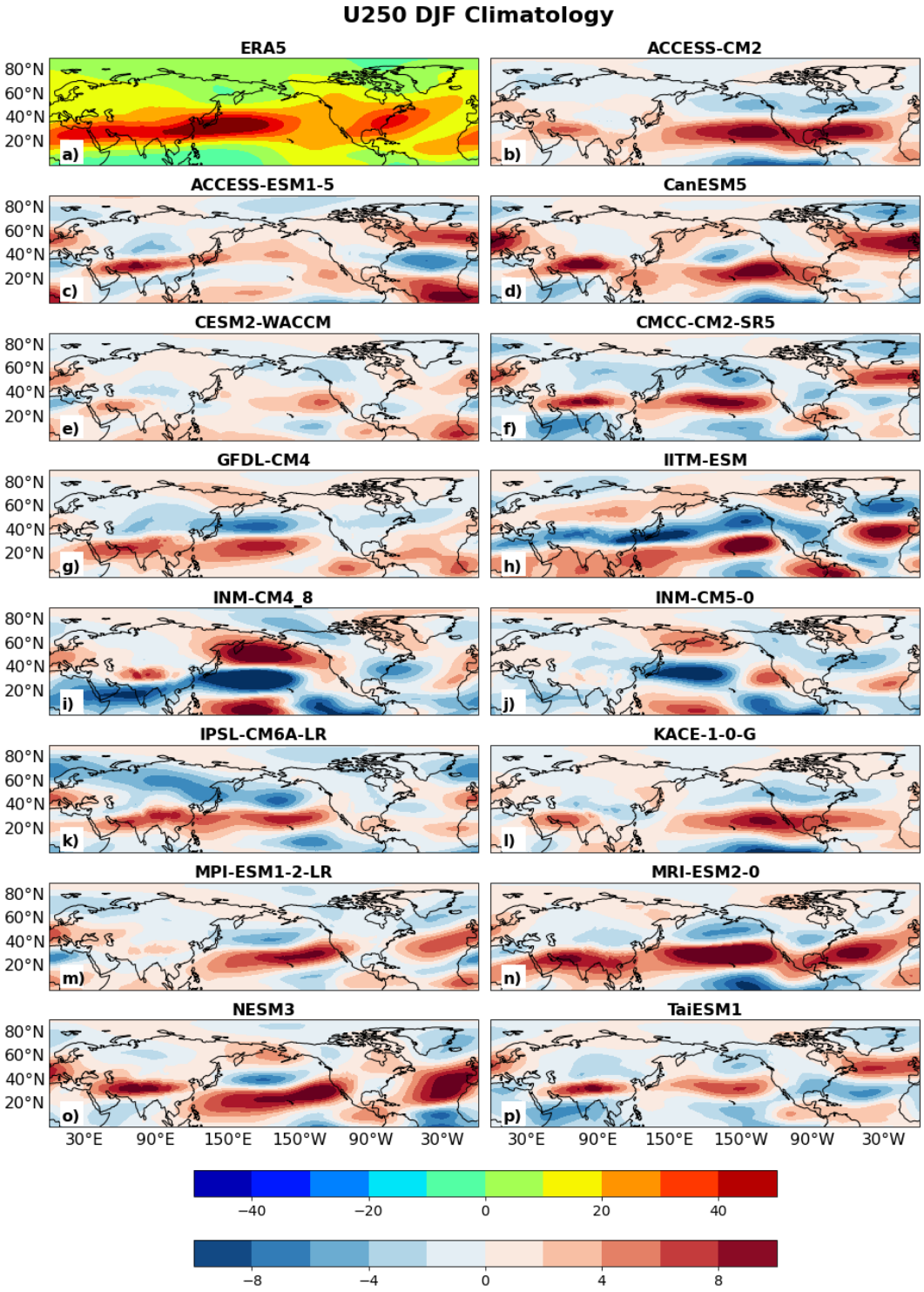

Fig. 4.10 ERA5 climatological mean U250 field for DJF in a). Panels b-p show the difference between each model's climatological mean in DJF and ERA5's (model mean – ERA5 mean). Units are m/s

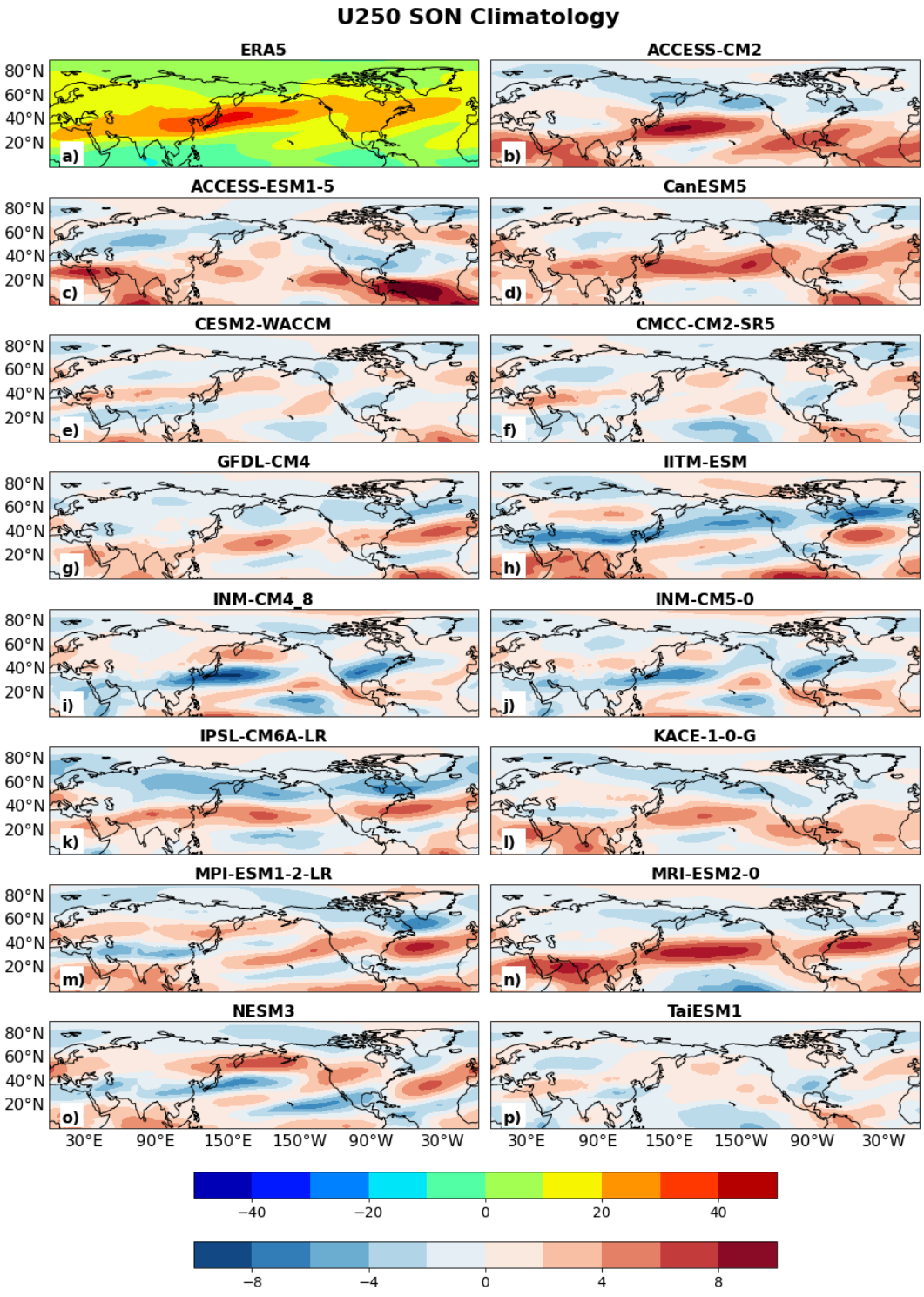

Fig. 4.11 Same format as **Fig. 4.10**, but for SON

4.4f – Q850 LSMPs

Lastly, model representation of the Q850 LSMPs is considered. Sinking motion, coupled with reduced moisture content over the Northeast, provides a conducive environment for dry spell conditions in the presence of either the Cluster 1 or Cluster 2 LSMP (Sukhdeo et al. 2023). Given that the models generally have issues representing the correct CDD distribution (i.e., too many short CDDs, not enough long CDDs), we examine how well the models capture the low-level moisture anomalies present during the dry spells.

Fig. 4.12 shows the Q850 LSMPs for ERA5 and the models for Cluster 1. While the models are able to represent the reduced moisture over the Northeast, some of the models, such as CMCC-CM2-SR5 (Fig. 4.12f) and INM-CM4-8 (Fig. 4.12i), have a negative Q850 anomaly that extends farther south into the lower southeastern United States. Despite these differences, the models in general are able to capture the moisture reduction over the Northeast for the Cluster 1 dry spells. This is perhaps not surprising, as our dry spell identification process already selects for dry conditions over the region, and dry conditions should be accompanied by reduced moisture, irrespective of what other deficiencies a particular model may have.

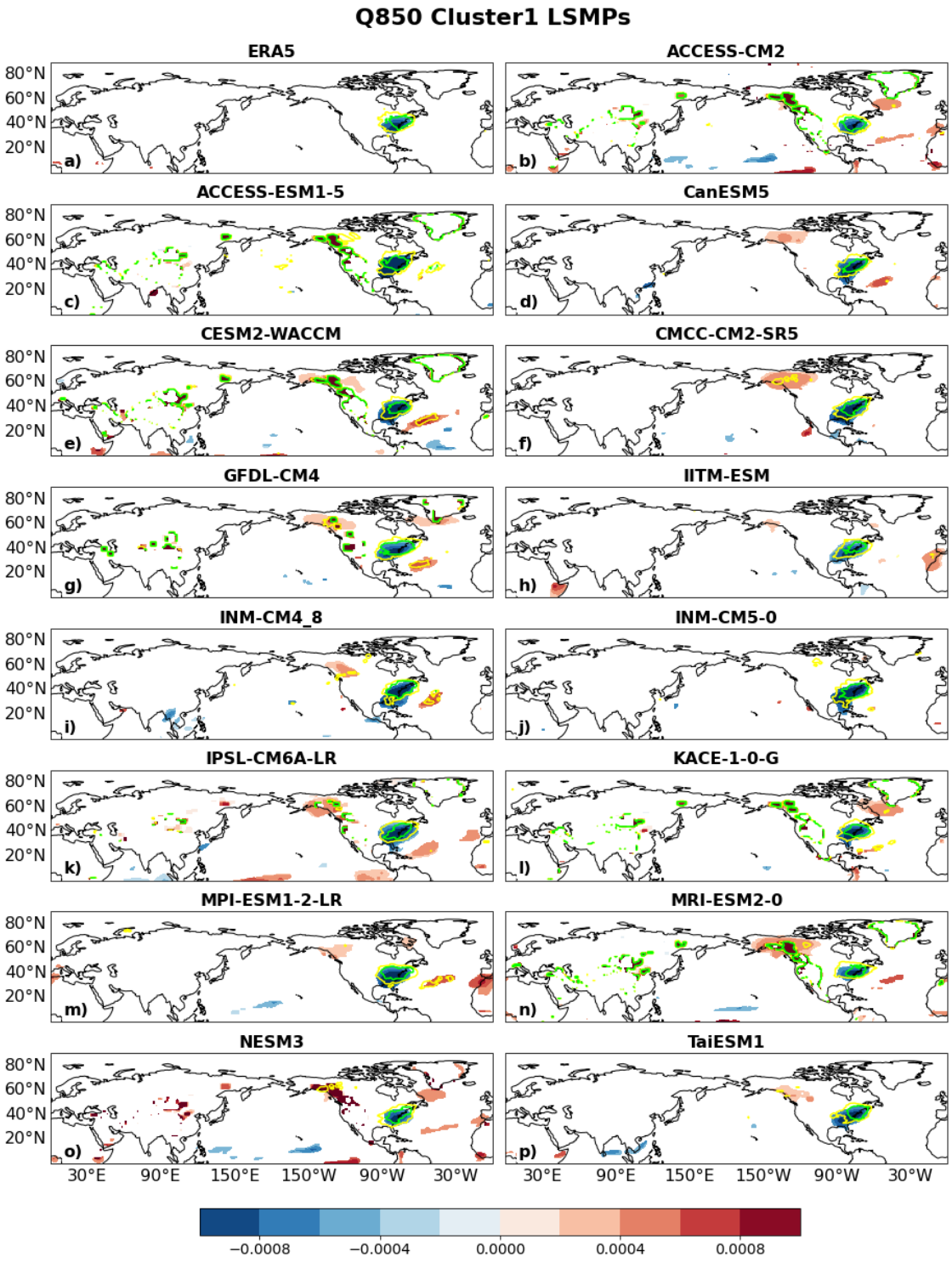

Fig. 4.12 Large-scale meteorological patterns (LSMPs), defined by the 850-hPa specific humidity anomaly field (kg/kg; contours), for the short-duration dry spell events in Cluster 1 for ERA5 and the CMIP6 models. Contour shading indicates areas of significance determined by bootstrap resampling. Yellow and green contours indicate: sign count magnitude of 0.6 and 0.8, such that 80% and 90% of the members in the cluster have the same sign, respectively. Values are scaled by 10^{-4}

With regards to Cluster 2 (Fig. 4.13), most models are able to capture the general pattern of the Q850 anomalies of ERA5 (Fig. 4.13a), with a positive anomaly located in east-central North America and a small negative anomaly centered over the Northeast. Some models, such as MPI-ESM1-2-LR (Fig. 4.13m), do not capture the significant negative anomaly centered over the Northeast. Regarding the positive anomaly in east-central North America, Sukhdeo et al. (2022) found that vapor transport from the Gulf of Mexico can provide an important moisture source for Northeast precipitation. For Cluster 2, with its high pressure anomaly LSMP, that circulation helps to bring moisture northward as it converges in central North America. The models, however, vary in terms of their ability to capture the correct magnitude and expanse of that moisture anomaly. Most models overestimate both the magnitude and expanse of the positive Q850 anomaly, consistent with their positive biases for the SF500 Cluster 2 LSMP. The stronger LSMP allows for increased moisture transport into central North America as compared to ERA5.

Overall, most of the CMIP6 models are able to capture the negative Q850 anomalies over the Northeast for Cluster 1 and Cluster 2, albeit with some differences from ERA5 outside of our Northeast region.

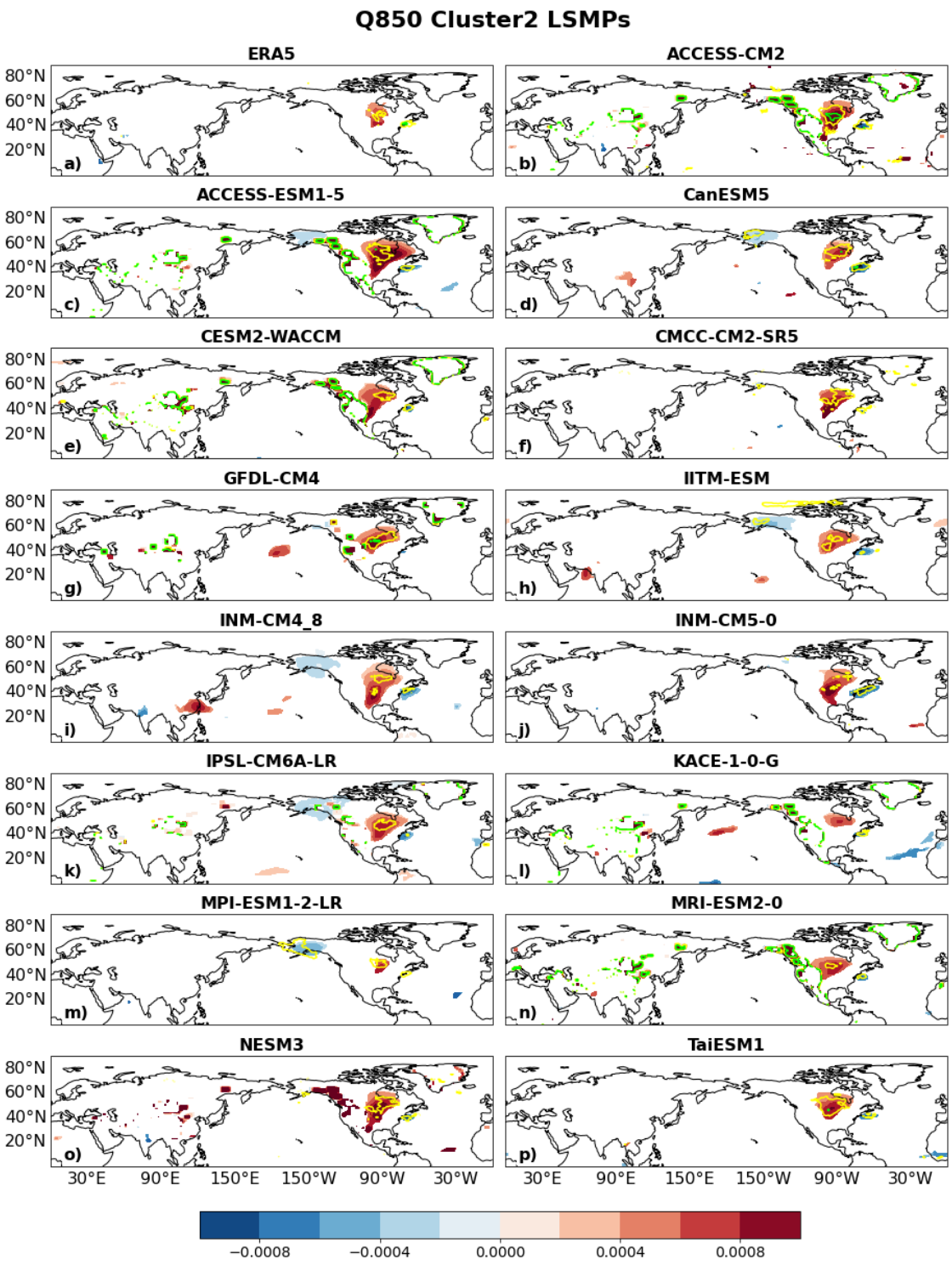

Fig. 4.13 Same format as **Fig. 4.12**, but for Cluster 2

4.4g – SF500 Composites: ERA5 Compared to CMIP6 Weighted

As we have demonstrated, the CMIP6 models vary in their abilities to represent the different characteristics of Northeast dry spells, specifically the distribution of consecutive dry days, the seasonality of dry spell events, and the representation of the SF500 LSMPs. These differences have been discussed in the preceding sections of this work. Here, we discuss overall model performance based on the weighting scheme described in Section 4.3c, with model weights shown in the last column of Table 4.2. Based on this weighting scheme, GFDL-CM4, KACE-1-0-G, CanESM5, and TaiESM1 are the four best-performing models, with model weights of 9.42%, 9.28%, 7.21%, and 7.04%, respectively. This does not mean that these models are without deficiencies, only that they perform best in accordance with the criteria and metrics we've deemed important for this analysis. The four worst-performing models are IPSL-CM6A-LR, INM-CM4-8, CMCC-CM2-SR5, and MRI-ESM2-0, with model weights of 5.07%, 5.65%, 5.69%, and 5.95%, respectively. The other models have model weights ranging from 6.01% to 7.03%.

As this study is primarily interested in the model representation of the SF500 LSMPs, we want to determine how well the Cluster 1 and Cluster 2 CMIP6 weighted composites compare to those from ERA5. Does the unequal weighting of the models generate composites that compensate for any deficiencies in any one model? Fig. 4.14 shows the ERA5 Cluster 1 (Fig. 4.14a) and Cluster 2 (Fig. 4.14b) composites, the corresponding CMIP6 weighted composites (Fig. 4.14c,d), and the difference between the CMIP6 weighted and ERA5 composites (Fig. 4.14e,f). For both clusters, the main LSMP areas near the Northeast are visually well-captured by the weighted composites. However, the Cluster 1 weighted composite has a more southwest-to-northeast orientation compared to ERA5's, and the magnitude is close to ERA5's (projection coefficient of 1.099). For Cluster 2, the CMIP6 weighted composite has a larger magnitude compared to ERA5's (projection

coefficient of 1.331). In terms of pattern placement, the weighted composites compare favorably with ERA5's, with local and expanded spatial correlation values for both clusters of > 0.90. However, for both clusters, the model weighted composites emphasize a tripole-like wave train that extends from the central Pacific to the eastern United States coast that is not emphasized as strongly in ERA5. So, while the CMIP6 weighted composites are a reasonable approximation for the corresponding patterns from ERA5, the weighted composites still have some difficulties in representing certain local and upstream LSMP structures.

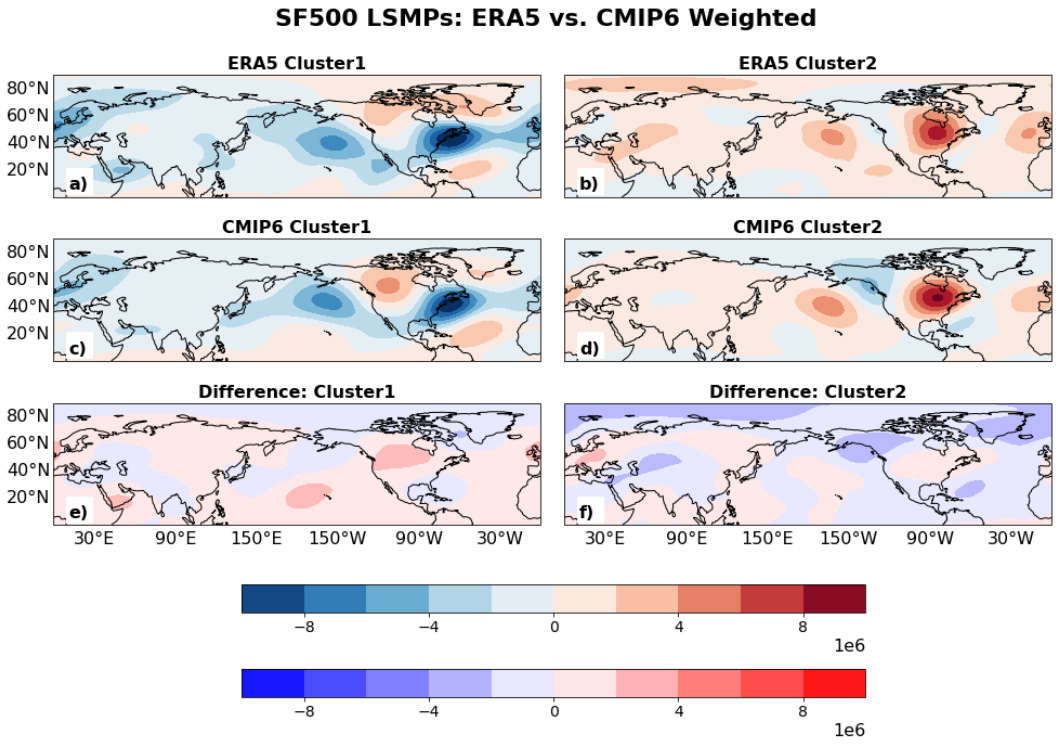

Fig. 4.14 Comparison of ERA5 Cluster 1 and Cluster 2 SF500 anomaly composites to those of CMIP6 using a weighted mean. Weighting for the CMIP composites is based on the weights in Table 4.2. Difference plots between ERA5 and the CMIP6 weighted mean (CMIP6 – ERA5) are shown in Panel E (Cluster 1) and Panel F (Cluster 2). Stream function values are scaled by 10^6, with units of m^2/s

4.5 – Summary and Discussion

In this study, we examine the fidelity of 15 CMIP6 models in representing several important characteristics of short-duration dry spells over the Northeast. We establish a set of metrics that best capture key aspects of the consecutive dry day distribution, the seasonality of dry spell events, and the representation of SF500 LSMPs, and evaluate each model in the framework of those metrics. Key results from this analysis are the following:

- There is a wide range of model ability to correctly capture the distribution of consecutive dry days, with most models overestimating the number of short events (1 or 2 days long) and underestimating the number of longer events (12 days or longer).
- Most models capture the seasonality of the dry spell events, with most Cluster 1 events occurring in DJF and MAM, and most Cluster 2 events occurring in SON. Some models, such as CMCC-CM2-SR5, GFDL-CM4, IITM-ESM, INM-CM5-0, MPI-ESM1-LR, and NESM3, are unable to capture enough dry spell events during MAM.
- The models are able to visually capture the Cluster 1 and Cluster 2 SF500 LSMPs, but vary in their ability to correctly capture LSMP magnitude and placement / structure.
- Model biases in the climatologies of SF500 and U250 seem to be partly responsible for biases in model representation of the SF500 LSMPs.
- In the case of Q850, the models capture the Q850 anomalies well over the Northeast region.

Several models (GFDL-CM4, KACE-1-0-G, CanESM5, and TaiESM1) are the better-performing models with regard to our set of evaluation metrics, while other models (IPSL-CM6A-LR, INM-CM4-8, CMCC-CM2-SR5, and MRI-ESM2-0) performed least well based on our evaluation metrics. While no one model closely replicates all aspects of the short-duration dry spells, there is value in understanding the strengths and limitations of each model in producing

historical simulations. While models with higher native resolution tend to score higher based on the metrics used here, resolution alone is not a proxy for better performance, suggesting that model parametrization and physics are also important and should be explored further.

The metrics used for this study are developed to be specific for the Northeast and are chosen to highlight the main characteristics of interest pertaining to CDD duration, seasonality, and LSMP structure, while also capturing the range of abilities of the CMIP6 models to match ERA5. The goal of this study is not to define any particular model as "good or "bad" at representing historical dry spells, but instead to provide information on the range of CMIP6 region-specific dry spell characteristics that are important in observations and reanalysis and model-specific insights on the drivers of these biases.

From our evaluation of the CMIP6 models here, the range of model limitations in reproducing aspects of the CDD distribution, event seasonality, and the SF500 LSMPs suggest that CMIP6 precipitation and large-scale circulation projections for the Northeast should be considered with some degree of caution. Future work could look to examine the potential causes of climatological mean biases in the SF500 and U250 fields of the CMIP6 models, and how they relate to biases in the representation of the SF500 LSMPs, as well as use the better-performing models (with our identified weights) to find pooled projections of future Northeast dry spell characteristics. Such work would be useful for the improvement and future development of models, and also assist with stakeholder planning and policy decisions as pertaining to our understanding of Northeast regional meteorology and climate.

4.6 – References

Agel, L., M. Barlow, J. Polonia, and D. Coe, 2020a: Simulation of northeast U.S. extreme precipitation and its associated circulation by CMIP5 models. *J. Climate*, **33**, 9817–9834, doi:10.1175/JCLI-D-19-0757.1.

Agel, L., and M. Barlow, 2020b: How well do CMIP6 historical runs match observed northeast U.S. precipitation and extreme precipitation–related circulation? *J. Clim.*, **33(22)**, 9835–9848. doi:10.1175/JCLI-D-19-1025.1.

Andreadis, K. M., and D. P. Lettenmaier, 2006: Trends in 20th century drought over the continental United States. *Geophys. Res. Lett.*, **33**, L10403, doi:10.1029/2006GL025711.

Boucher, O., S. Denvil, G. Levavasseur, A. Cozic, A. Caubel, M.-A. Foujols, et al., 2018: IPSL IPSL-CM6A-LR model output prepared for CMIP6 CMIP historical. Earth System Grid Federation. doi:10.22033/ESGF/CMIP6.5195.

Byun, Young-Hwa, Y.-J. Lim, H.-M. Sung, J. Kim, M. Sun, B.-H. Kim, 2019: NIMS-KMA KACE1.0-G model output prepared for CMIP6 CMIP. Earth System Grid Federation. doi:10.22033/ESGF/CMIP6.2241.

Cao, J., and B. Wang, 2019: NUIST NESMv3 model output prepared for CMIP6 CMIP historical. Earth System Grid Federation. doi:10.22033/ESGF/CMIP6.8769.

Choudhury, A. D., K. Raghavan, P.A. Gopinathan, S. Narayanasetti, M. Singh, S. Panickal, and A. Modi, 2019: CCCR-IITM IITM-ESM model output prepared for CMIP6 CMIP historical. Earth System Grid Federation. doi:10.22033/ESGF/CMIP6.3708.

Collier, N., F. M. Hoffman, D. M. Lawrence, G. Keppel-Aleks, C. D. Koven, W. J. Riley, M. Mu, and J. T. Randerson, 2018: The International Land Model Benchmarking (ILAMB) system:

Design, theory, and implementation. *J. Adv. Model. Earth Syst.*, **10**, 2731–2754, doi:10.1029/2018MS001354.

Dai, A., 2013: Increasing drought under global warming in observations and models. *Nat. Climate Change*, **3**, 52–58, doi:10.1038/nclimate1633.

Danabasoglu, G., 2019: NCAR CESM2-WACCM model output prepared for CMIP6 CMIP historical. Earth System Grid Federation. doi:10.22033/ESGF/CMIP6.7627.

Dawson, A., 2016: Windspharm: A High-Level Library for Global Wind Field Computations Using Spherical Harmonics. *Journal of Open Research Software*, **4(1)**, p.e31. doi:10.5334/jors.129.

Dix, M., D. Bi, P. Dobrohotoff, R. Fiedler, I. Harman, and R. Law, 2019: CSIRO-ARCCSS ACCESS-CM2 model output prepared for CMIP6 CMIP historical. Earth System Grid Federation. doi:10.22033/ESGF/CMIP6.4271.

Eyring, V., S. Bony, G. A. Meehl, C. A. Senior, B. Stevens, R. J. Stouffer, and K. E. Taylor, 2016: Overview of the Coupled Model Intercomparison Project Phase 6 (CMIP6) experimental design and organization. *Geosci. Model Dev.*, **9**, 1937–1958, doi:10.5194/gmd-9-1937-2016.

Eyring, V., and Coauthors, 2019: Taking climate model evaluation to the next level. *Nat. Climate Change*, **9**, 102–110, doi:10.1038/s41558-018-0355-y.

Fereday, D., R. Chadwick, J. Knight, and A. A. Scaife, 2018: Atmospheric dynamics is the largest source of uncertainty in future winter European rainfall. *J. Climate*, **31**, 963–977, doi:10.1175/JCLI-D-17-0048.1.

Frumhoff, P. C., J. J. McCarthy, J. M. Melillo, S. C. Moser, and D. J. Wuebbles, 2007: Confronting climate change in the U.S. Northeast: Science, impacts, and solutions. Union of Concerned

Scientists, 146 pp., https://www.ucsusa.org/sites/default/files/2019-09/confronting-climate-change-in-the-u-s-northeast.pdf.

Grotjahn, R., 2011: Identifying extreme hottest days from large scale upper air data: A pilot scheme to find California Central Valley summertime maximum surface temperatures. *Clim Dyn.*, **37**, 587–604, doi:10.1007/s00382-011-0999-z.

Grotjahn, R., and Coauthors, 2016: North American extreme temperature events and related large scale meteorological patterns: a review of statistical methods, dynamics, modeling, and trends. *Clim Dyn.*, **46**, 1151–1184, doi:10.1007/s00382-015-2638-6.

Guo, H., J.G. John, C. Blanton, C. McHugh, S. Nikonov, A. Radhakrishnan, et al., 2018): NOAA-GFDL GFDL-CM4 model output. Earth System Grid Federation. doi:10.22033/ESGF/CMIP6.1402.

Hayhoe, K., and Coauthors, 2007: Past and future changes in climate and hydrological indicators in the US Northeast. *Clim Dyn.*, **28**, 381–407, doi:10.1007/s00382-006-0187-8.

Hersbach H., and Coauthors, 2020: The ERA5 global reanalysis. *Q J R Meteorol Soc.*, **146**, 1999–2049, doi:10.1002/qj.3803.

Kharin, V. V., F. W. Zwiers, X. Zhang, and G. C. Hegerl, 2007: Changes in temperature and precipitation extremes in the IPCC ensemble of global coupled model simulations. *J. Climate*, **20**, 1419–1444, doi:10.1175/JCLI4066.1.

Lee, Y.-Y., and R. Grotjahn, 2016: California Central Valley summer heat waves form two ways. *J. Climate*, **29**, 1201–1217, doi:10.1175/JCLI-D-15-0270.1.

Lee, J., K. R. Sperber, P. J. Gleckler, C. J. Bonfils, and K. E. Taylor, 2018: Quantifying the agreement between observed and simulated extratropical modes of interannual variability. *Climate Dyn.*, **52**, 4057–4089, doi:10.1007/s00382-018-4355-4.

Lee, W.-L., and H.-C. Liang, 2020: AS-RCEC TaiESM1.0 model output prepared for CMIP6 CMIP historical. Earth System Grid Federation. doi:10.22033/ESGF/CMIP6.9755.

Li, J., H. Chen, X. Rong, J. Su, Y. Xin, K. Furtado, S. Milton, and N. Li, 2018: How well can a climate model simulate an extreme precipitation event: A case study using the transpose-AMIP experiment. *J. Climate*, **31**, 6543–6556, doi:10.1175/JCLI-D-17-0801.1.

Lovato, T., and D. Peano, 2020: CMCC CMCC-CM2-SR5 model output prepared for CMIP6 CMIP historical. Earth System Grid Federation. doi:10.22033/ESGF/CMIP6.3825.

Moon, H., L. Gudmundsson, and S. I. Seneviratne, 2018: Drought persistence errors in global climate models. *J. Geophys. Res. Atmos.*, **123**, 3483–3496, doi:10.1002/2017JD027577.

Nasrollahi, N., A. AghaKouchak, L. Cheng, L. Damberg, T. J. Phillips, C. Miao, K. Hsu, and S. Sorooshian, 2015: How well do CMIP5 climate simulations replicate historical trends and patterns of meteorological droughts? *Water Resour. Res.*, **51**, 2847–2864, doi:10.1002/2014WR016318.

Palipane, E. and R. Grotjahn, R., 2018: Future Projections of the Large-Scale Meteorology Associated with California Heat Waves in CMIP5 Models. *J. Geophys. Res. Atmos.*, **123**, 8500–8517, doi:10.1029/2018JD029000.

Reed, K.A. and Coauthors, 2022: Metrics as tools for bridging climate science and applications. *WIRES Clim. Chg*. In press, doi:10.1002/WCC.799.

Strzepek, K., G. Yohe, J. Neumann, and B. Boehlert, 2010: Characterizing changes in drought risk for the United States from climate change. *Environ. Res. Lett.*, **5**, 044012, doi:10.1088/1748-9326/5/4/044012.

Sukhdeo, R., P.A. Ullrich, and R. Grotjahn, 2022: Assessing the large-scale drivers of precipitation in the northeastern United States via linear orthogonal decomposition. *Clim Dyn*, doi:10.1007/s00382-022-06289-y.

Sukhdeo, R., R. Grotjahn, and P.A. Ullrich, 2023: Two large-scale meteorological patterns are associated with short-Duration dry spells in the northeastern United States. *Mon. Wea. Rev.*, **151**, pp. 2993-3011. doi:10.1175/MWR-D-23-0141.1.

Swart, N.C., J.N.S. Cole, V. V. Kharin, M. Lazare, J.F. Scinocca, N.P. Gillett, J. Anstey, V. Arora, J.R. Christian, Y. Jiao, W.G. Lee, F. Majaess, O.A. Saenko, C. Seiler, C. Seinen, A. Shao, L. Solheim, K. von Salzen, D. Yang, B. Winter, and M. Sigmond, 2019: CCCma CanESM5 model output prepared for CMIP6 ScenarioMIP. Earth System Grid Federation. doi:10.22033/ESGF/CMIP6.1317.

Volodin, E.; E. Mortikov, A. Gritsun, V. Lykossov, V. Galin, N. Diansky, A. Gusev, S. Kostrykin, N. Iakovlev, A. Shestakova, S. Emelina, 2019: INM INM-CM4-8 model output prepared for CMIP6 CMIP historical. Earth System Grid Federation. doi:10.22033/ESGF/CMIP6.5069.

Volodin, E.; E. Mortikov, A. Gritsun, V. Lykossov, V. Galin, N. Diansky, A. Gusev, S. Kostrykin, N. Iakovlev, A. Shestakova, S. Emelina, 2019: INM INM-CM5-0 model output prepared for CMIP6 CMIP historical. Earth System Grid Federation. doi:10.22033/ESGF/CMIP6.5070.

Wagener, T., and Coauthors, 2010: The future of hydrology: An evolving science for a changing world. *Water Resour. Res.*, **46**, W05301, doi:10.1029/2009WR008906.

Weigel, A. P., R. Knutti, M.A. Liniger, and C. Appenzeller, 2010: Risks of model weighting in multimodel climate projections. *J. Climate*, **23(15)**, 4175–4191. doi:10.1175/2010JCLI3594.1.

Wieners, K.-H., M. Giorgetta, J. Jungclaus, C. Reick, M. Esch, M. Bittner, and E. Roeckner, 2019: MPI-M MPI-ESM1.2-LR model output prepared for CMIP6 CMIP historical. Earth System Grid Federation. doi:10.22033/ESGF/CMIP6.6595.

Xie, P., A. Yatagai, M. Chen, T. Hayasaka, Y. Fukushima, C. Liu, and S. Yang, 2007: A gauge-based analysis of daily precipitation over East Asia, *J. Hydrometeorol.*, **8**, 607-626.

Xue, Z., and P.A. Ullrich, 2021a: A retrospective and prospective examination of the 1960s U.S. northeast drought. *Earth's Future*, **9**, e2020EF001930, doi:10.1029/2020EF001930.

Xue, Z., and P.A. Ullrich, 2021b: A comprehensive intermediate-term drought evaluation system and evaluation of climate data products over the conterminous United States. *Journal of Hydrometeorology*, **22(9)**, 2311–2337, doi:10.1175/JHM-D-20-0314.1.

Yukimoto, S., T. Koshiro, H. Kawai, N. Oshima, K. Yoshida, and S. Urakawa, 2019): MRI MRI-ESM2.0 model output prepared for CMIP6 CMIP historical. Earth System Grid Federation. doi:10.22033/ESGF/CMIP6.6842.

Ziehn, T., M. Chamberlain, A. Lenton, R. Law, R. Bodman, M. Dix, and K. Druken, 2019: CSIRO ACCESS-ESM1.5 model output prepared for CMIP6 CMIP historical. Earth System Grid Federation. doi:10.22033/ESGF/CMIP6.4272.

4.7 – Supplemental Materials

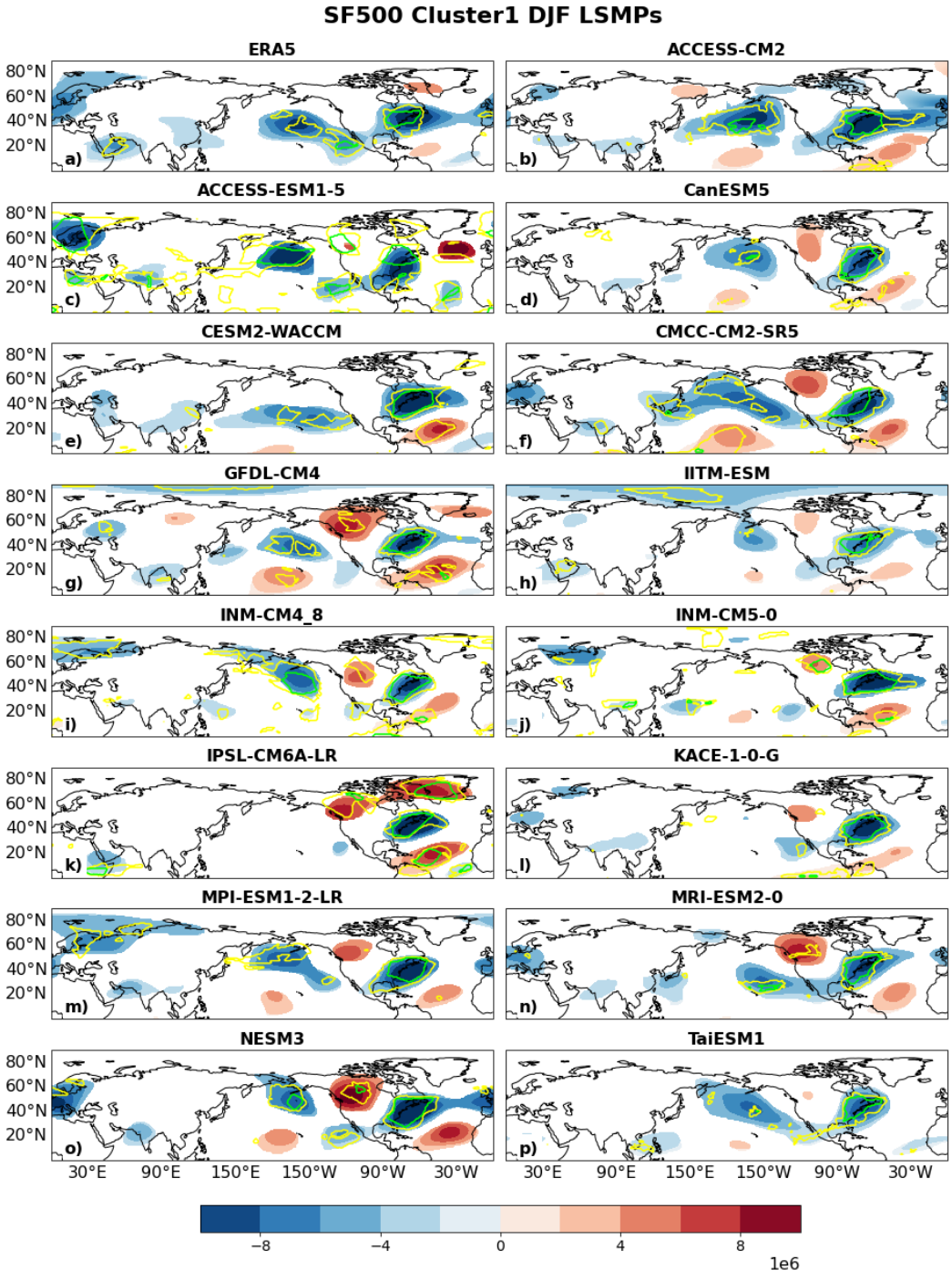

Fig. S1 Large-scale meteorological patterns (LSMPs), defined by the 500-hPa stream function anomaly field (m^2/s; contours), for the short-duration dry spell events in Cluster 1 in DJF for ERA5 and the CMIP6 models. Contour shading indicates areas of significance determined by bootstrap resampling. Yellow and green contours indicate: sign count magnitude of 0.6 and 0.8, such that 80% and 90% of the members in the cluster have the same sign, respectively. Stream function values are scaled by 10^6

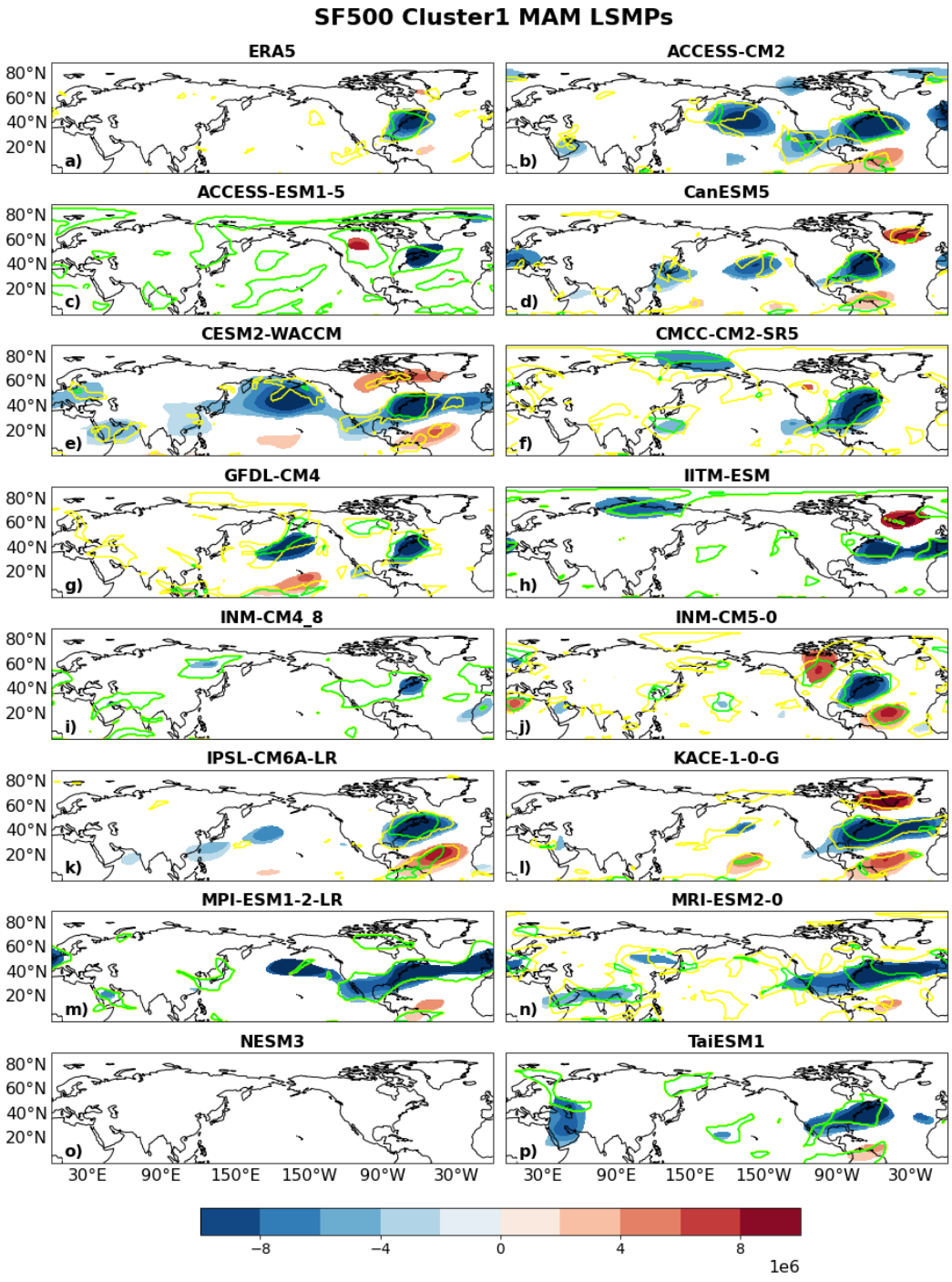

Fig. S2 Same format as **Fig. S1**, but for Cluster 1 MAM. NESM3 panel is intentionally left blank due to insufficient sample size

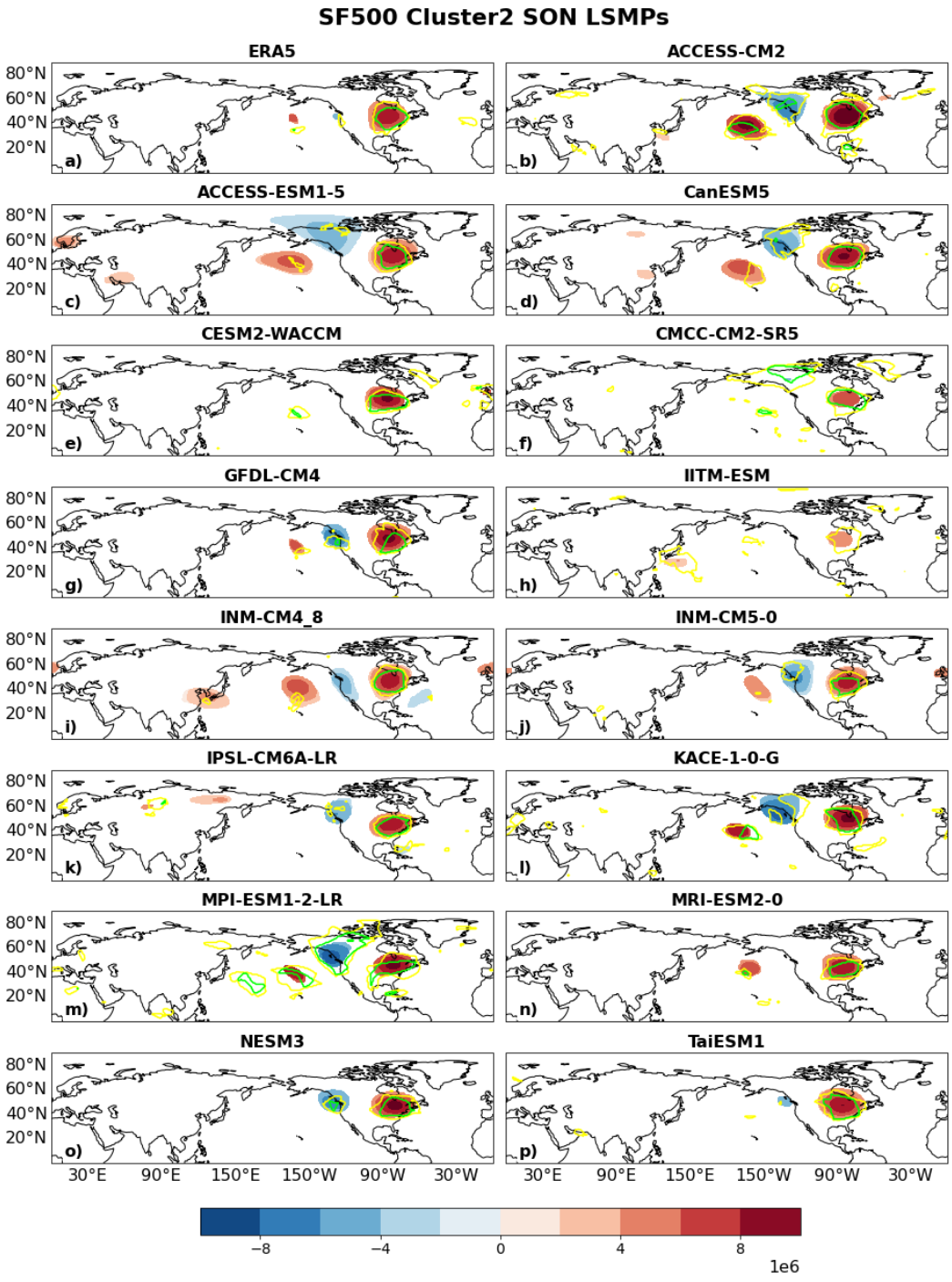

Fig. S3 Same format as **Fig. S1**, but for Cluster 2 SON

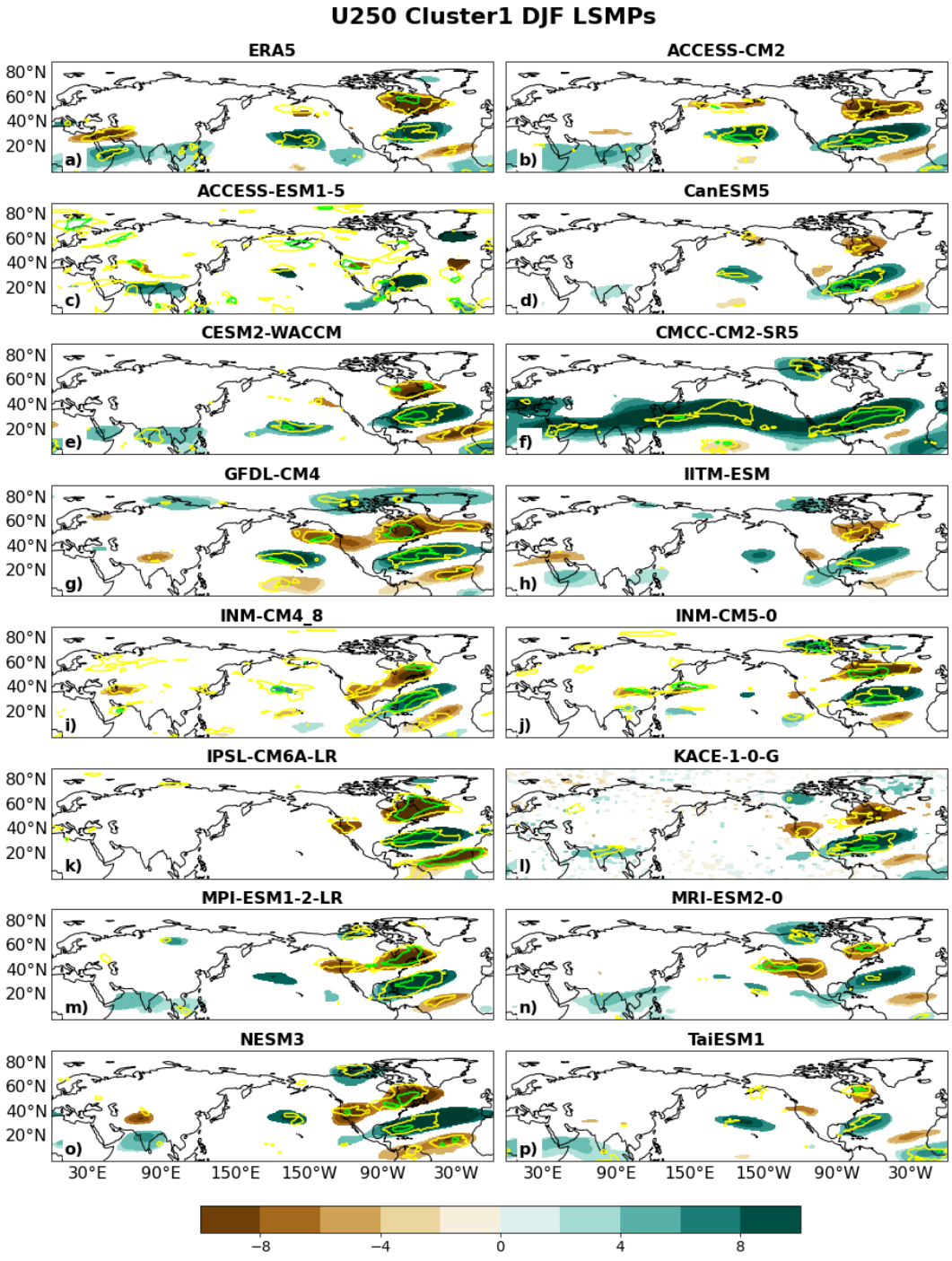

Fig. S4 Large-scale meteorological patterns (LSMPs), defined by the 250-hPa zonal wind anomaly field (m/s; contours), for the short-duration dry spell events in Cluster 1 in DJF for ERA5 and the CMIP6 models. Contour shading indicates areas of significance determined by bootstrap resampling. Yellow and green contours indicate: sign count magnitude of 0.6 and 0.8, such that 80% and 90% of the members in the cluster have the same sign, respectively

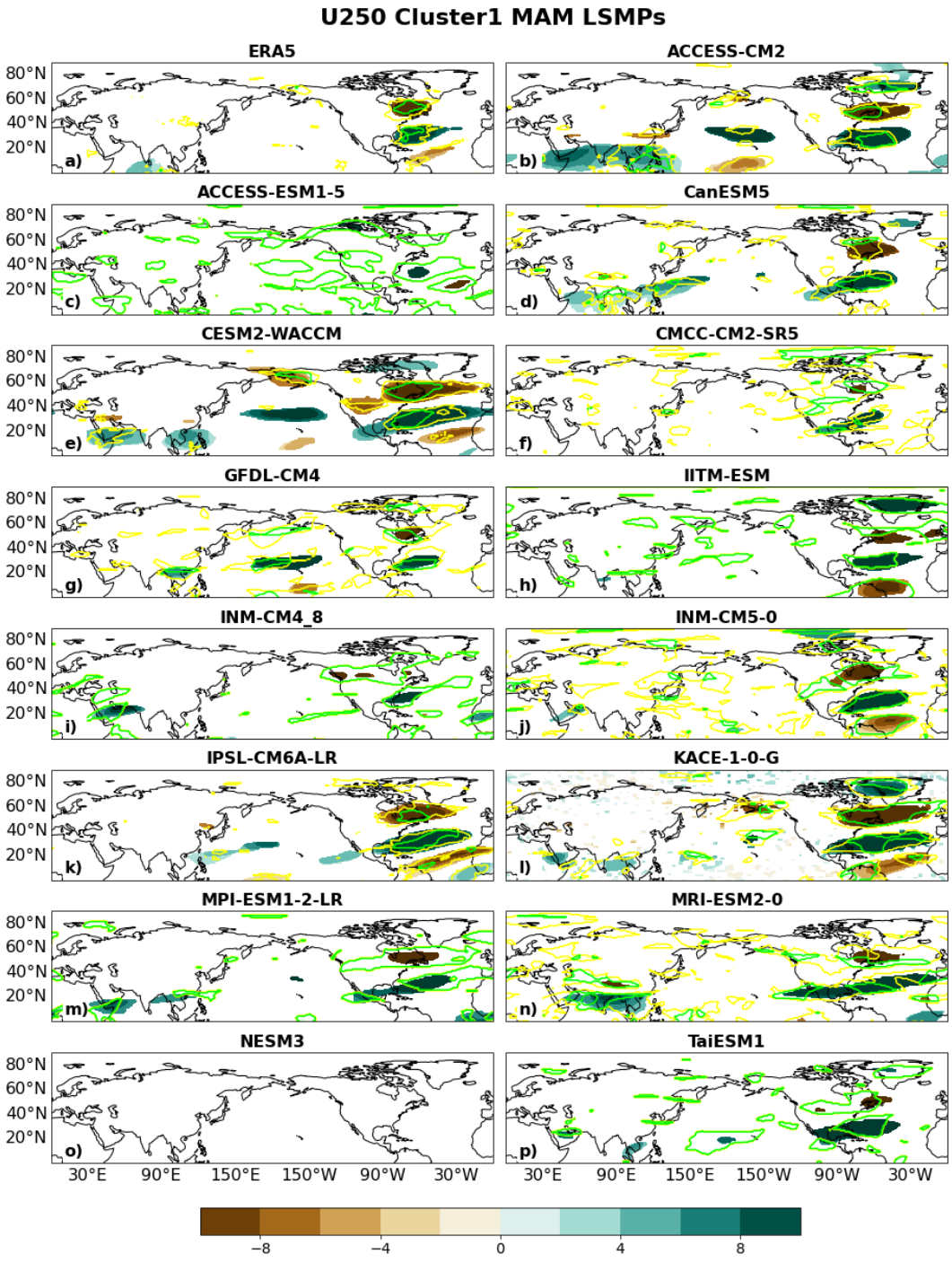

Fig. S5 Same format as **Fig. S4**, but for Cluster 1 MAM. NESM3 panel is intentionally left blank due to insufficient sample size

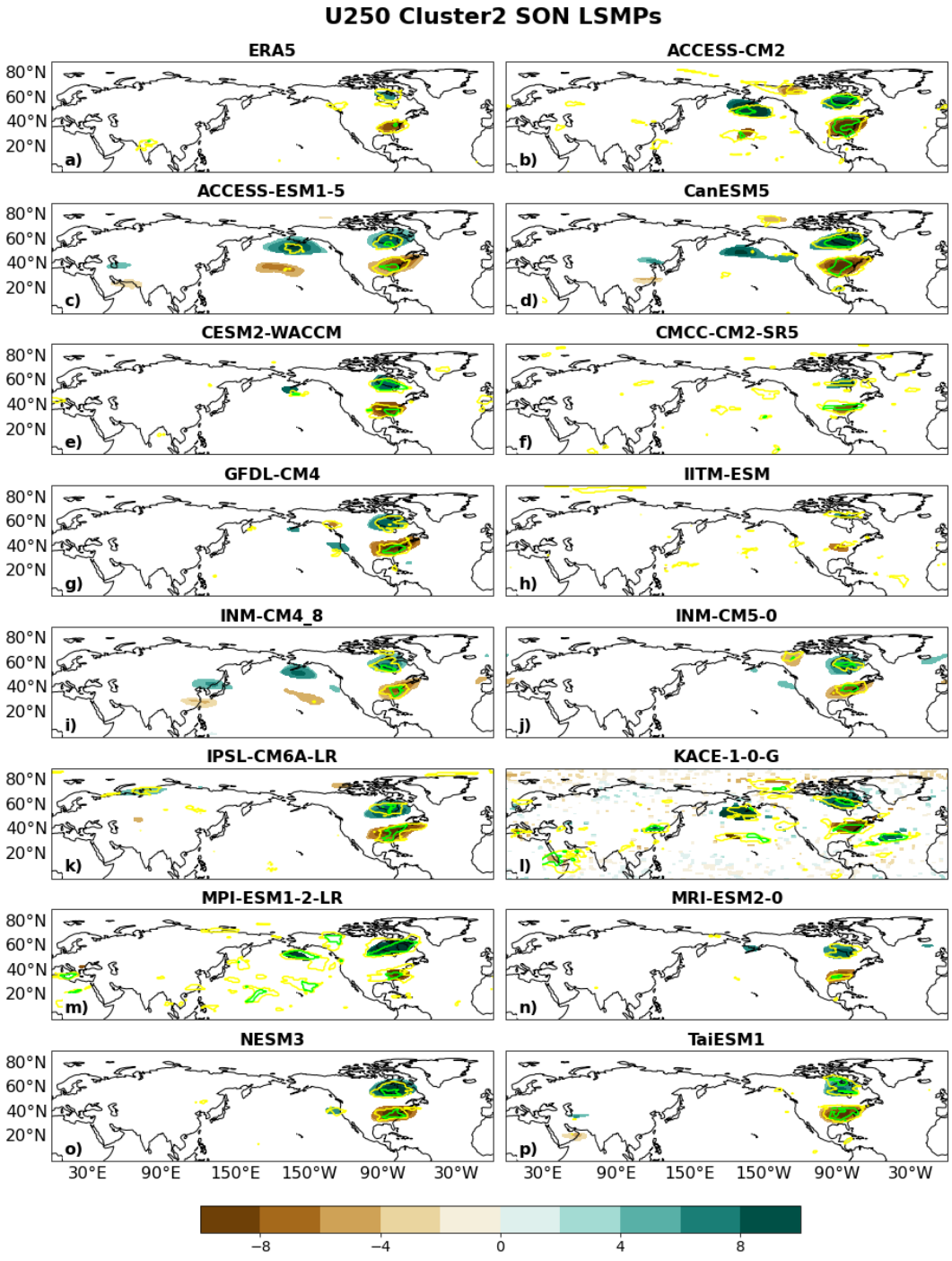

Fig. S6 Same format as **Fig. S4**, but for Cluster 2 SON

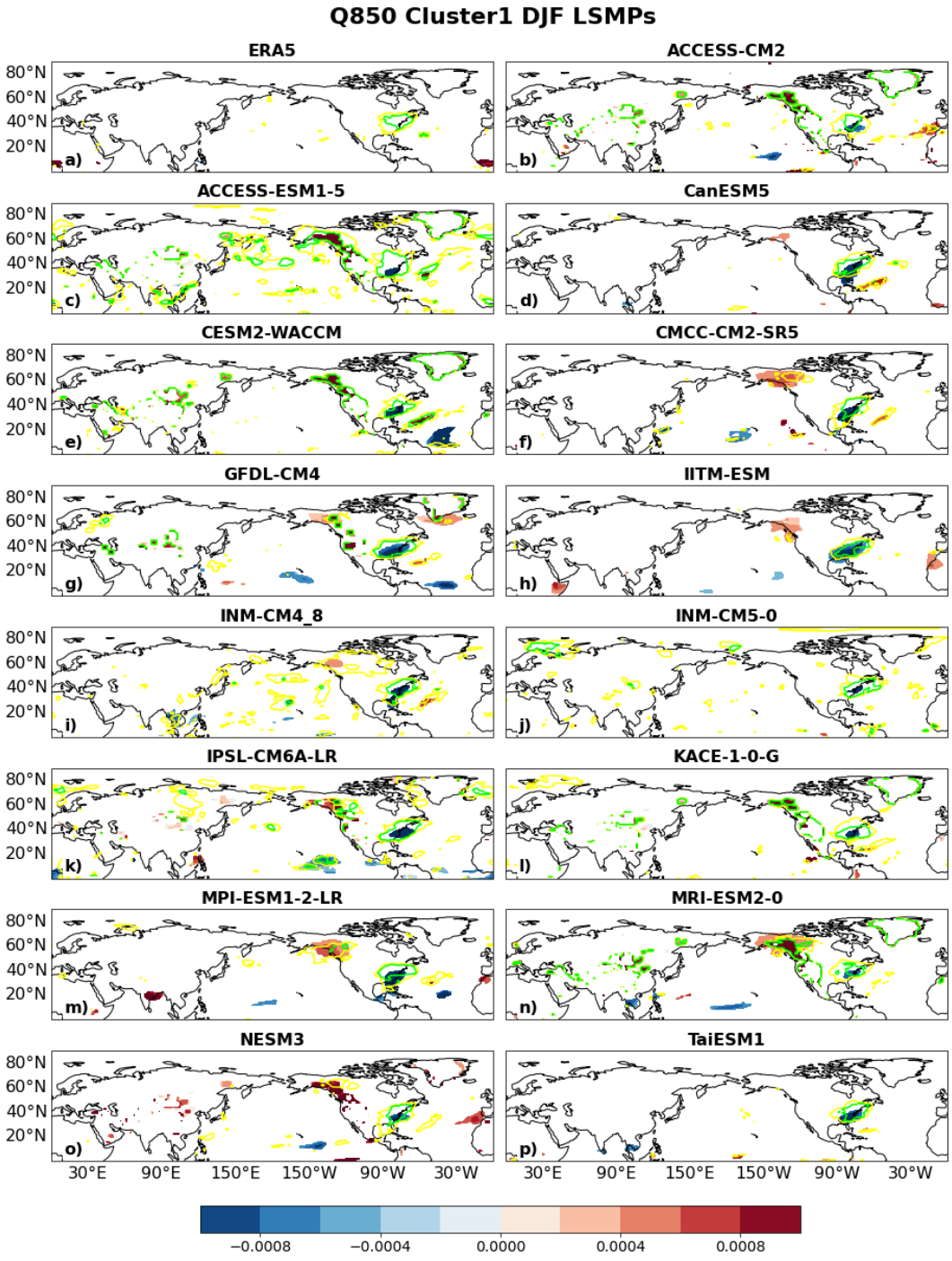

Fig. S7 Large-scale meteorological patterns (LSMPs), defined by the 850-hPa specific humidity anomaly field (kg/kg; contours), for the short-duration dry spell events in Cluster 1 in DJF for ERA5 and the CMIP6 models. Contour shading indicates areas of significance determined by bootstrap resampling. Yellow and green contours indicate: sign count magnitude of 0.6 and 0.8, such that 80% and 90% of the members in the cluster have the same sign, respectively. Values are scaled by 10^{-4}

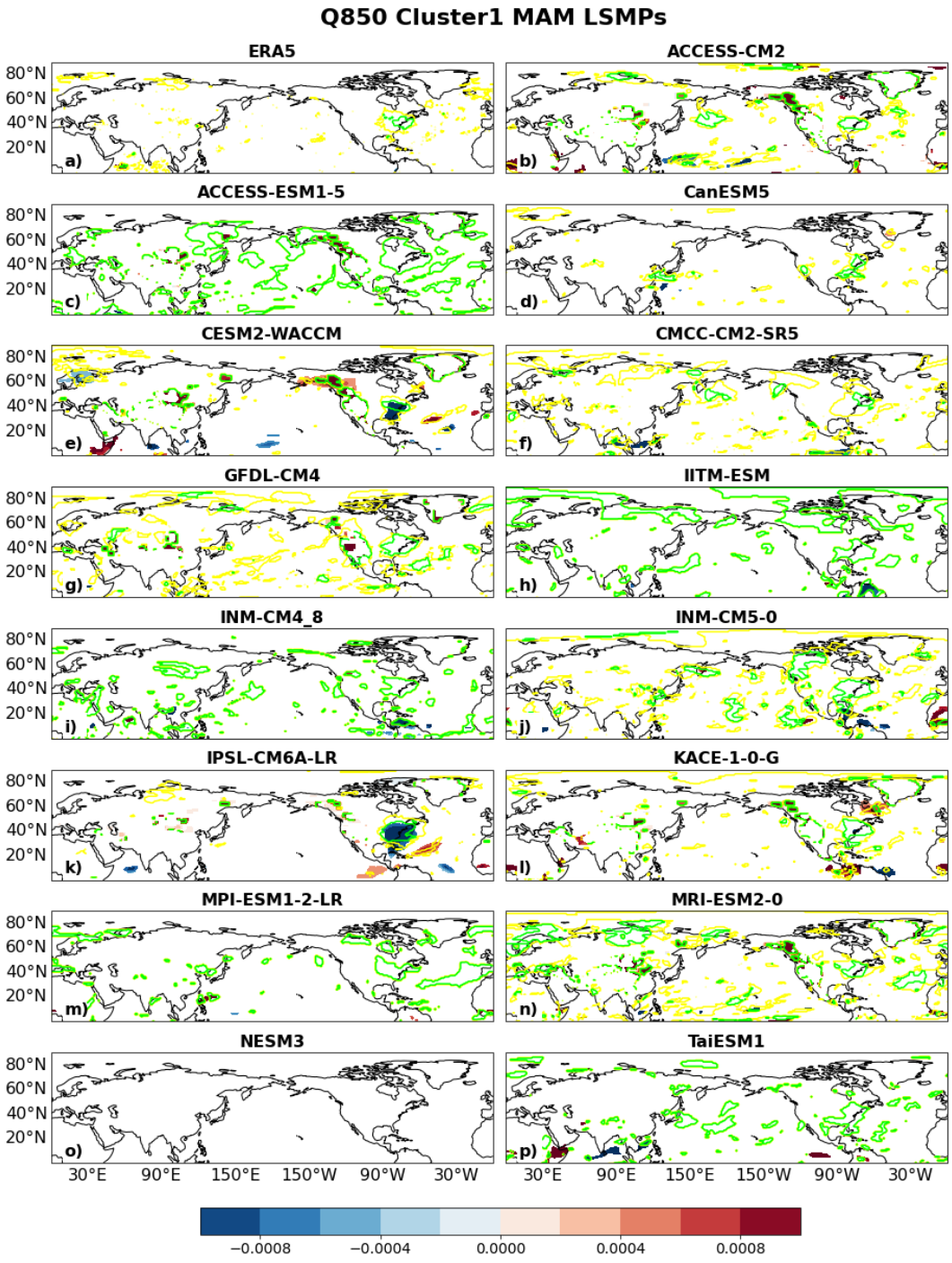

Fig. S8 Same format as **Fig. S7**, but for Cluster 1 MAM. NESM3 panel is intentionally left blank due to insufficient sample size

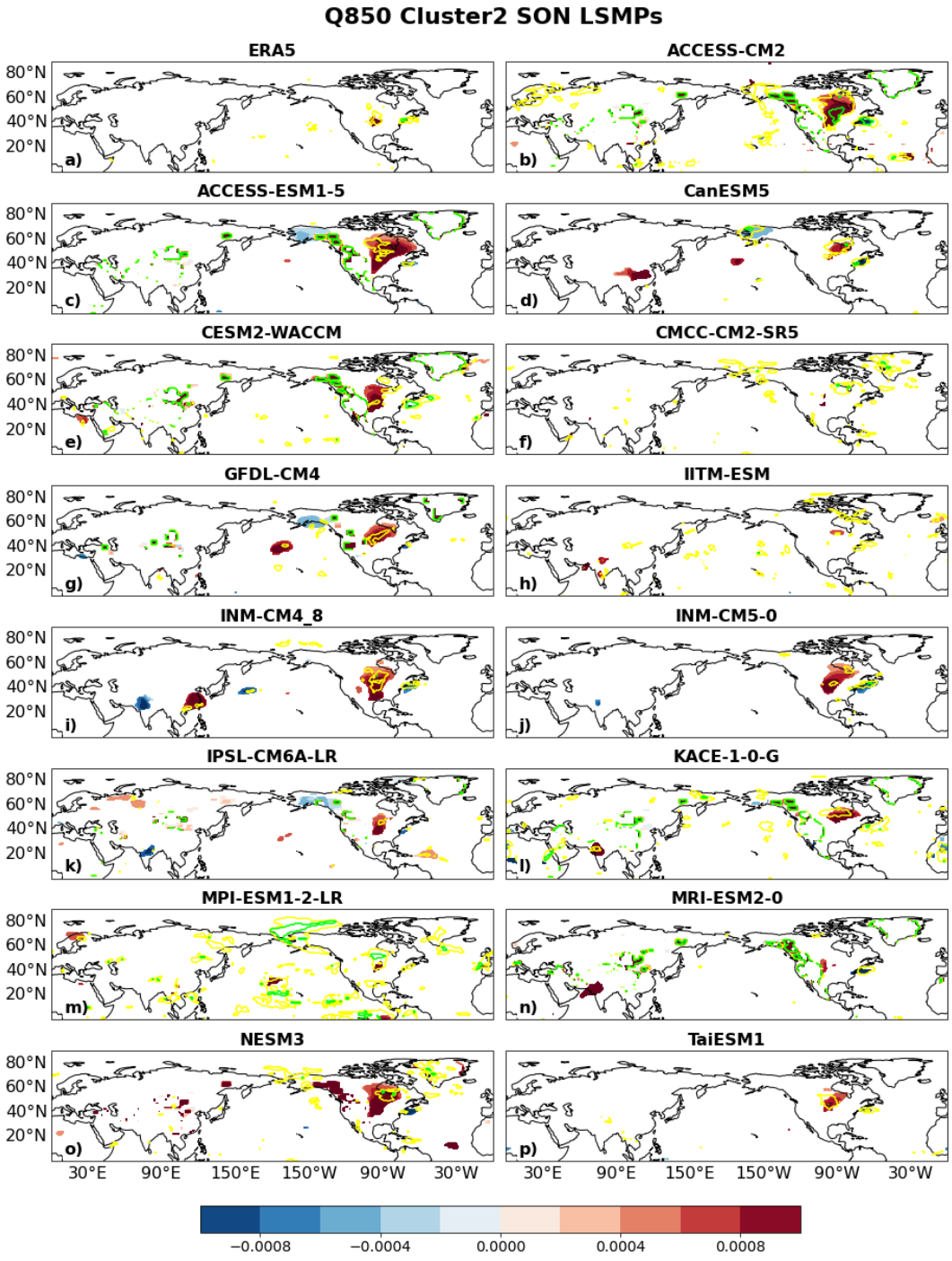

Fig. S9 Same format as **Fig. S7**, but for Cluster 2 SON

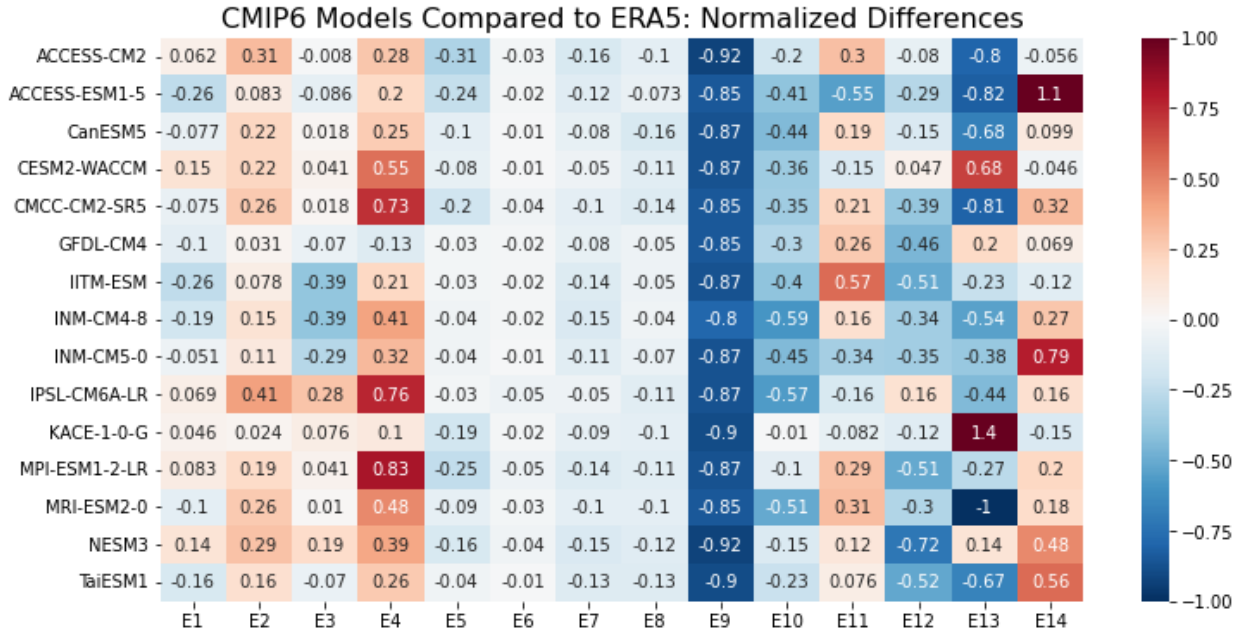

Fig. S10 Normalized differences between the CMIP6 models and ERA5 for the fourteen variables (E1 through E14) in Table 4.2. Normalized differences are calculated as: (model value – ERA5 value) / (ERA value) for each variable considered in Table 4.2

Chapter 5 – Summary, Conclusions, and Future Work

5.1 Summary and Conclusions

This PhD dissertation has sought to broadly improve our understanding of the large-scale meteorology of precipitation variability over the northeastern United States, with emphasis on understanding the large-scale atmospheric drivers of that variability and using that understanding to examine short-duration dry spells that impact the region.

In Chapter 2, a novel linear orthogonal decomposition (LOD) approach is introduced as a means for identifying the large-scale drivers of precipitation over the Northeast. The method allows one to sub-sample the time series of many different predictor fields in order to maximize linear predictability of precipitation. The analysis determined that vapor transport along the Atlantic seaboard (first linear mode), extratropical cyclone activity (second linear mode), and vapor transport from the Gulf of Mexico (third linear mode) are the prominent large-scale drivers of precipitation over the Northeast. When examining both ends of the precipitation spectrum (i.e., droughts and extreme precipitation), these drivers are often reduced or absent (in the case of droughts) or enhanced (in the case of extreme precipitation). Furthermore, it was also inferred from the analysis that the large-scale meteorological patterns (LSMPs) play an important role in modulating these precipitation drivers. LSMPs related to extreme precipitation over the Northeast have already been studied extensively (see References from previous chapters), but understanding those LSMPs related to short-duration dry spells had not yet been addressed in great detail, thus providing some impetus for my continued PhD work.

Chapter 3 assesses that large-scale meteorology associated with short-duration dry spells, with emphasis on identifying the LSMPs that cause the dry spells. Two LSMPs – a strong low-

pressure anomaly in the mid-latitude Atlantic Ocean and a strong high-pressure anomaly in east-central North America – are associated with these short-duration dry spells. Both LSMPs lead to a reduction in the large-scale precipitation drivers identified in Chapter 2, with reduced vapor transport from the Atlantic seaboard, a southward shift in the extratropical cyclone storm track, and a reduction in vapor transport from the Gulf of Mexico.

Some of the analysis in Chapter 2 compares ERA5 to the CESM1 large ensemble to determine if the LOD linear modes are robust across multiple data products. Our three primary linear modes are indeed robust across multiple data products, but some differences in the representation of the linear modes do exist. As such, it is likely that current generation GCMs have issues representing LSMPs as well. This served as a motivation for the study undertaken in Chapter 4, which seeks to assess the ability of CMIP6 models to represent the large-scale meteorology of short-duration dry spells over the Northeast. As shown in Chapter 4, some of the CMIP6 models not only have difficulties representing the correct magnitude and placement of the dry spell LSMPs, but they also have issues with representing the correct CDD distribution and the seasonality of the dry spell events, which may hint at limitations with model resolution, physics, parameterization, or some combination of all three.

While this PhD dissertation has focused on the northeastern United States, large-scale drivers of precipitation variability, and short-duration dry spells that impact the region, the large-scale framework of this dissertation can be used to study regional climate in any area of the world. By first identifying the large-scale atmospheric drivers of a particular field (ex. precipitation, temperature, etc.), then examining the LSMPs that modulate those large-scale atmospheric drivers, and then examining the representation of those LSMPs within current-generation GCMs, a comprehensive assessment of a particular type of climate extreme that impacts a particular region

can be achieved. This kind of assessment, coupled with insight into which model deficiencies may be causing model biases in the large-scale meteorology, can be very useful for facilitating model improvements.

5.2 Future Work

Given the topics presented here in this PhD dissertation, there are several opportunities for future work, specifically with regard to 1) understanding climatological model biases in the CMIP6 models, 2) future projections of the large-scale meteorology associated with Northeast dry spells, and 3) the potential role of remote teleconnections modes in the manifestation of dry spell LSMPs. These topics for future work are discussed briefly in the following paragraphs.

As discussed in Chapter 4, many of the CMIP6 have either a positive or negative bias in terms of the Cluster 1 and Cluster 2 LSMPs. For example, ACCESS-CM2 has a strong negative bias in the central Pacific and a strong (albeit weaker) negative bias in the mid-latitude Atlantic Ocean for the Cluster 1 LSMP. When examining the DJF SF500 climatological mean for ACCESS-CM2, we find that the climatological mean also has a negative bias compared to ERA5 in both regions. Given that we calculate SF500 anomalies relative to the climatological mean, it is highly likely that biases in the mean are impacting some models' representation of the LSMPs. This climatological mean bias also shows up in the U250 climatology, as many models suffer from issues with jet stream strength and positioning. Given that the jet stream plays an important role in Rossby wave trains and the positioning of troughs and ridges within circulation patterns, it is important to understand how model biases in the SF500 and U250 climatologies may be related and may be impacting model representation of the LSMPs. Can identifying the sources of these

biases assist in improving model representation of the dry spell LSMPs? This additional analysis is ongoing, and will accompany the analysis in Chapter 4 as part of a future manuscript submission.

Given that Chapter 4 focused on historical model representation of dry spell LSMPs in CMIP6, a logical next step would be to look at future projections of dry spell characteristics over the Northeast, using the SSP585 ("business as usual") projection scenario. For this particular analysis, many of the methodological steps outlined in Chapter 4 would be repeated for each of the CMIP6 models' SSP585 scenario, for the period 2040-2100. Similar metrics will be used to evaluate the models' representation of CDD distribution, dry spell seasonality, and SF500 LSMPs. Also, model weights for the historical simulations will be assumed to hold constant for the future simulations. Of particular interest in this analysis would be to determine if there is a significant change is certain dry spell characteristics. For example, do dry spell events occur more frequently in future periods? Does dry spell event seasonality change? Does the frequency of Cluster 1 or Cluster 2 events change? Care must be taken for this analysis, however, as it has been shown that the models are not all equally adept at representing the dry spells in their historical simulations, so relying on weighted averages (which weight better-performing models more strongly) for different dry spell characteristics may be a reliable means for assessing future projections.

Lastly, there is interest in determining the role of remote teleconnection modes in influencing the development of the dry spell LSMPs. In particular, we are interested in the North Atlantic Oscillation (NAO) (given its area of influence near the Northeast) and the Madden-Julian Oscillation (MJO) (given its intra-seasonal time scale that overlaps with our dry spells time scale). To begin such an analysis, one would first need to identify events of different phases (negative and positive phase for NAO; phase pairs 8-1, 2-3, 4-5, and 6-7 for MJO), and events belonging to those phases would need to be composited together. Using lead and lag composites, the goal would be

to determine if there is a physical overlap between the SF500 LSMPs *after* a particular climate mode and the SF500 LSMPs *before* our dry spell events. If there is a physical overlap, this may indicate there they may be some teleconnection mechanism at play. Some initial work with this approach has shown that there can be a physical overlap of these patterns. However, the SF500 composites are often not statistically significant, nor do they persist for longer than ~5 days. This likely means that more careful analysis is needed. For example, there may be physical differences between strong negative NAO events that occur in DJF, so purely grouping DJF events together when compositing may be muddying any significant signals. Additionally, relying solely on lead-lag composites may not provide precise information about whether possible teleconnection mechanisms exist. Coupling lead-lag composites with another tool, such as Rossby ray tracing, may offer more clarity regarding any teleconnections that may impact the development of dry spell LSMPs over the Northeast.

These three topics offer exciting avenues for future work, and as time permits, I hope to explore these topics in greater detail. Such additional work would not only assist in model improvement and future model development, but would also serve to inform about the predictability of dry spells in the Northeast, which may assist stakeholders with interests pertaining to future resource allocations and water management practices in the Northeast.